Doctoral Dissertation

$CoFe_2O_4$ Nanoparticles on Bio-based Polymer Derived Nitrogen Doped Carbon as Bifunctional Electrocatalyst for Li-air Battery

PIRAPATH ARKASALERKS

Supervisor: Noriyoshi Matsumi

Graduate School of Advanced Science and Technology
Japan Advanced Institute of Science and Technology

[Materials Science]

September 2024

Abstract

This research work focuses on the utilization of a bio-based polymer-derived nitrogen-doped carbon as a support for $CoFe_2O_4$ nanoparticles electrocatalyst in Li-air battery application. This work also showcases the electrocatalyst's bifunctional ability to perform robust electrochemical performances. Nowadays lithium-air batteries (LABs) have emerged as a promising prospect due to their unparalleled theoretical energy density of 3,505 $Whkg^{-1}$. However, despite the promising theoretical advantages, issues such as poor cycling stability, limited lifespan, and unresolved side reactions have hindered their commercial viability and widespread adoption. The major challenges of LABs are sluggish oxygen kinetics from oxygen reduction reaction (ORR) and oxygen evolution reaction (OER) are major issues that hinder their performance. Hence, developing electrocatalysts to promote ORR/OER is essential to reach the theoretical performance of LABs.

In this study, we introduced spinel cobalt iron oxide ($CoFe_2O_4$) nanoparticles decorated on bio-derived pyrolyzed poly(2,5-benzimidazole) (PYPBI800) as a nitrogen-doped carbon support electrocatalyst for LABs. The electrocatalyst was synthesized through pyrolysis of PBI followed by incipient wetness impregnation calcination on the metal precursors. The Strong Metal-Substrate Interaction (SMSI) between $CoFe_2O_4$ and PBI800 has been confirmed with X-ray photoelectron spectroscopy. Due to both the intrinsic properties of $CoFe_2O_4$ and the nitrogen doping effect, these electrocatalysts also modulate the electronic state of metals, facilitating oxygen adsorption and desorption at the electrode.

The electrocatalysts were evaluated as air-breathing electrodes in a CR-2032 coin-type cell LABs compared with other types of carbon supports. The initial discharge capacity for LAB coin cells with $CoFe_2O_4$ on PBI800 was observed to be 18,356 $mAhg^{-1}$. Furthermore, the cycling stability of the $CoFe_2O_4$ on PBI800 cathode was tested through 200 charge-discharge cycles at 400 mAg^{-1} with 1,000 $mAhg^{-1}$ cut-off capacity. The resulting cycle-life data revealed that the battery maintains a discharge capacity as high as 100% even after the 200th cycle, demonstrating exceptional stability with overpotential remains consistently low at 140 mV throughout the examined cycle. The extensive surface area with N heteroatom defects of the PBI provides abundant nucleation sites for $CoFe_2O_4$ nanoparticles which serve as active sites for ORR and OER. The $CoFe_2O_4$ nanoparticles formed on the support exhibit strong metal-substrates interaction which leads to high exceptional stability and electrocatalytic activity.

Based on these findings, the $CoFe_2O_4$ nanoparticles on bio-based polymer-derived nitrogen-doped carbon suggested through this hold promise as a practical air-breathing electrode for high-performance rechargeable LABs. This work will also benefit future heteroatom-doped carbon support design, specifically nitrogen to enhance LABs performance.

Keywords: Oxygen Reduction Reaction, Oxygen Evolution Reaction, Metal Nanoparticles, Lithium Air Battery, Nitrogen Doped Carbon.

Preface

This thesis is consolidation of results of the doctoral research works on the topic of "$CoFe_2O_4$ nanoparticles on bio-based polymer derived nitrogen doped carbon as bifunctional electrocatalyst for Li-air battery". This work was carried out under the supervision of Professor Noriyoshi Matsumi at the School of Materials Sciences, Japan Advanced Institute of Science and Technology during October 2021 – September 2024.

Energy storage is crucial in our modern society for a variety of reasons. It plays a vital role in balancing the supply and demand of electricity, ensuring a stable and reliable power supply. Energy storage not only improves the efficiency of power grids but also reduces the reliance on fossil fuels, contributing to a more sustainable and environmentally friendly energy landscape. Lithium-air batteries (LABs) are a promising option among various battery technologies, primarily due to their remarkable theoretical energy density. LABs utilize oxygen from the atmosphere as a reactant. However, their practical application is impeded by several issues, including poor cycling stability, limited lifespan, and unresolved side reactions. The main difficulties are associated with the air cathode, which consists of porous material for Li_2O_2 storage and electrocatalysts to aid oxygen reduction and evolution reactions. The development of effective electrocatalysts is key to unlocking the full theoretical potential of LABs.

The work presented in this thesis covers the synthesis of $CoFe_2O_4$ nanoparticles on bio-based polymer derived nitrogen doped carbon and their application as electrocatalyst materials for oxygen reduction reaction and oxygen evolution reaction in non-aqueous Li-air batteries. The thesis concludes with a final chapter that encapsulates all the research conducted and offers perspectives on the potential future uses of pyrolyzed poly(2,5-benzimidazole) in electrocatalytic applications.

Pirapath Arkasalerks

School of Material Science

Japan Advanced Institute of Science and Technology

October 2024

Table of Contents

Abstract ii

Preface iv

Table of Figures vii

Acknowledgement ix

Chapter 1 Introduction 1

1.1 General Introduction 1

1.2 Oxygen Reduction Reaction and Oxygen Evolution Reaction in Aqueous Electrolyte 2

1.2.1 Oxygen Reduction Reaction in Aqueous Electrolyte 2

1.2.2 Oxygen Evolution Reaction in Aqueous Electrolyte 5

1.3 Oxygen Reduction Reaction and Oxygen Evolution Reaction in Nonaqueous Li-Air Batteries 6

1.3.1 Oxygen Reduction Reaction as Discharge in Li-Air Batteries 6

1.3.2 Oxygen Evolution Reaction as Charge in Li-Air Batteries 9

1.4 Catalysts for Li- air battery 10

1.4.1 Noble metal 11

1.4.2 Carbon-based 12

1.4.3 Transition-metal oxides 14

1.5 Strong Metal-Substrates Interaction 19

1.6 Introduction to Poly(2,5-benzimidazole) 21

1.7 Electrochemical Performance Testing 22

1.7.1 Rotating Disk Electrode 22

1.7.2 Cyclic Voltammetry 25

1.7.3 Linear Sweep Voltammetry 26

1.7.4 Electrochemical impedance spectroscopy 27

1.8 Li-air Battery Evaluation 28

1.9 Research Outlook 29

References 30

Chapter 2 $CoFe_2O_4$ Nanoparticles on Bio-based Polymer Derived Nitrogen Doped Carbon as Bifunctional ORR/OER Electrocatalyst in Nonaqueous Electrolyte. 38

Abstract 38

2.1 Introduction 38

2.2 Experimental 41

2.2.1 Synthesis of Pyrolyzed Poly(2,5-benzimidazole) 41
2.2.2 Decoration of $CoFe_2O_4$ on PYPBI800 42
2.2.3 Characterization of Electrocatalyst 42
2.2.4 Electrochemical Characterization 42
2.3 Results and Discussion 43
2.3.1 Characterisation of Electrocatalysts 43
2.4 Electrocatalytic Performance of Electrocatalysts 57
2.5 Conclusions 60
References 61
Chapter 3 $CoFe_2O_4$ Nanoparticles on Bio-based Polymer Derived Nitrogen Doped Carbon as Bifunctional Electrocatalyst for Li-air Battery 65
Abstract 65
3.1 Introduction 65
3.2 Experimental 67
3.2.1 Electrocatalyst Preparation 67
3.2.2 Characterisation of Electrocatalyst 68
3.2.3 Electrochemical Characterisation 68
3.2.4 Li−Air Battery Fabrication and Testing 69
3.3 Results and Discussion 69
3.3.1 Characterisation of Electrocatalysts 69
3.3.2 Electrocatalytic Performance of Electrocatalysts 70
3.3.3 Li-Air Battery Evaluation 73
3.4 Post-mortem Analysis 77
3.5 Conclusions 79
References 79
Chapter 4 Conclusion 90
4.1 General Conclusion 90
4.2 Future Prospects 92

Table of Figures

Figure 1.1 ORR pathways mechanism in acidic electrolyte[7]. 3
Figure 1.2 ORR pathways mechanism in alkaline electrolyte[8]. 4
Figure 1.3 OER mechanism pathways in acidic and alkaline electrolytes[9]. 6
Figure 1.4 ORR mechanism pathways on cathode in non-aqueous LAB 7
Figure 1.5 OER mechanism pathways on cathode in non-aqueous LAB 9
Figure 1.6 ORR volcano plot of noble metal electrocatalysts 12
Figure 1.7 SEM images of a) α-MnO_2 and β-MnO_2 and initial discharge of LAB employing various type of MnO_2 as cathode in c) LiPF6/PC electrolyte and d) LiTFSI/TEGDME[67] . 16
Figure 1.8 TEM images and histograms of the Pt NP size distribution of a) Pt/PANIlong750 and b) Pt/PANIlong1000 21
Figure 1.9 Synthesis of polymer poly(2, 5-benzimidazole) (2,5-PBI) from DABA[108] 22
Figure 1.10 Rotating Disk Electrode with three electrodes system configuration. 23
Figure 1.11 K-L plot from RDE which use to determine the number of electrons transferred 25
Figure 1.12 Example of cyclic voltammogram for electrochemically reversible one-electron redox process [110] 25
Figure 1.13 Example of CV potential waveform [111]. 26
Figure 1.14 Comparison of a) Linear sweep voltammetry (LSV) and b) cyclic voltammetry waveforms[112]. 27
Figure 1.15 Experimental and simulated impedance spectra showing a simplified Randles equivalent circuit for an electrochemical system. [114] 28
Figure 1.16 LAB evaluation including a) cycle stability test, b) initial discharge capacity, and c) LAB efficiencies and overpotential[116]. 29
Figure 2.1 SEM images of a) PBI800, b) Fe PBI, c) Co PBI, d)20%$CoFe_2O_4$ PBI, e) 10%$CoFe_2O_4$ PBI, and f) 30%$CoFe_2O_4$ PBI 45
Figure 2.2 SEM-EDS Mapping images of PYPBI800 a) Depicted area for EDS elemental mapping. b) Carbon c) Nitrogen 45
Figure 2.3 SEM-EDS Mapping images of Fe PBI a) Depicted area for EDS elemental mapping. b) Carbon c) Nitrogen d) Oxygen e) Iron 46
Figure 2.4 SEM-EDS Mapping images of Co PBI a) Depicted area for EDS elemental mapping. b) Carbon c) Nitrogen d) Oxygen e) Cobalt 46
Figure 2.5 SEM-EDS Mapping images of 10%$CoFe_2O_4$ PBI a) Depicted area for EDS elemental mapping. b) Carbon c) Nitrogen d) Oxygen e) Iron f) Cobalt 47
Figure 2.6 SEM-EDS Mapping images of 20%$CoFe_2O_4$ PBI a) Depicted area for EDS elemental mapping. b) Carbon c) Nitrogen d) Oxygen e) Iron f) Cobalt 47
Figure 2.7 SEM-EDS Mapping images of 30%$CoFe_2O_4$ PBI a) Depicted area for EDS elemental mapping. b) Carbon c) Nitrogen d) Oxygen e) Iron f) Cobalt 48
Figure 2.8 XRD patterns corresponded to Fe PBI, Co PBI, 20%$CoFe_2O_4$ PBI, and PBI800 . 49
Figure 2.9 a) HR-TEM image, b) lattices fringes, and c) SAED pattern of 20%$CoFe_2O_4$ PBI 49
Figure 2.10 XPS survey spectra for a) PYPBI800, b) 20%$CoFe_2O_4$ Graphite, c) Co PBI, d) Fe PBI, e) 10%$CoFe_2O_4$ PBI, and f) 20%$CoFe_2O_4$ PBI 52

Figure 2.11 XPS spectra of PYPBI800, 20%$CoFe_2O_4$ Graphite, Co PBI, Fe PBI, 10%$CoFe_2O_4$ PBI, and 20%$CoFe_2O_4$ PBI at a) C 1s region and b) N 1s region. 53
Figure 2.12 XPS spectra at O 1s region of PYPBI800, 20%$CoFe_2O_4$ Graphite, Co PBI, Fe PBI, 10%$CoFe_2O_4$ PBI, and 20%$CoFe_2O_4$ PBI 54
Figure 2.13 XPS spectra of PYPBI800, 20%CoFe2O4 Graphite, Co PBI, Fe PBI, 10%CoFe2O4 PBI, and 20%CoFe2O4 PBI at a) Co 2p region and b) Fe 2p region. 55
Figure 2.14 CV plot comparing a) different metal content and b) different metal loading at 1600 rpm at a scan rate of 50 mVs^{-1} in 0.1 M LiTFSI in TEGDME under O_2 atmosphere. ... 59
Figure 2.15 Coulombic efficiency of electrocatalyst calculated from CV at 1600 rpm at a scan rate of 50 mVs^{-1} in 0.1 M LiTFSI in TEGDME under O_2 atmosphere. 59
Figure 2.16 Potentiostatic electrochemical impedance spectroscopy of electrocatalyst calculated at 1600 rpm in 0.1 M LiTFSI in TEGDME under O_2 atmosphere. 60
Figure 3.1 LSV plot comparing a) ORR on different metals, b), ORR on different $CoFe_2O_4$ content c) OER on different metals d) OER on different $CoFe_2O_4$ content at 1600 rpm at a scan rate of 5 mVs^{-1} in 0.1 M LiTFSI in TEGDME under O_2 atmosphere. 71
Figure 3.2 Tafel plots comparing different metal content in a) ORR and b) OER, and different metal loading in c) ORR and d) OER at 1600 rpm at a scan rate of 5 mVs^{-1} in 0.1 M LiTFSI in TEGDME under O_2 atmosphere 72
Figure 3.3 a)ORR and b)OER mechanism pathways on cathode in non-aqueous LAB 73
Figure 3.4 a) Initial discharge of LABs at the discharge current density of 200 mA g^{-1}, cyclic stability of LABs at current density of 400 mA g^{-1} for b) 1^{st} cycle, and c) 200^{th} cycle. 74
Figure 3.5 Cyclic stability of LABs at current density of 400 mA g^{-1} from 1^{st} cycle to 200^{th} cycle employing a) PYPBI800, b) Co PBI, c) Fe PBI, d) 10%$CoFe_2O_4$ PBI, e) 20%$CoFe_2O_4$ PBI, and f) 30%$CoFe_2O_4$ PBI as cathodes. 75
Figure 3.6 Overpotential and energy efficiency of LABs at current density of 400 mA g^{-1} from 1^{st} cycle to 200^{th} cycle employing a) PYPBI800, b) Co PBI, c) Fe PBI, d) 10%$CoFe_2O_4$ PBI, e) 20%$CoFe_2O_4$ PBI, and f) 30%$CoFe_2O_4$ PBI as cathodes 77
Figure 3.7 XPS results for pristine electrode and electrode after 200 charge-discharge cycles of 20%CoFe2O4 PBI at a) C1s, b) O1s, and c) F1s region 78

Acknowledgement

This research was conducted under the supervision of Professor Noriyoshi Matsumi at the School of Material Science, Japan Advanced Institute of Science and Technology from 2021 to 2024. The author expresses profound appreciation and gratitude to his supervisor, Professor Noriyoshi Matsumi, for his unwavering support and direction throughout this doctoral research.

The author also sincerely thanks the members of the review committee, *Assoc. Prof. Jumpei Ueda, Assoc. Prof. Anh Van Ho, Assoc. Prof. Shun Nishimura and Assoc. Prof. Takeshi Kakibe* for their valuable time, suggestions, and guidance during the process of thesis evaluation.

The author expresses his gratitude to *Prof. Toshiaki Taniike* for allowing him to work in their laboratories for the completion of minor research. The author is also thankful to *Sr. Lecturer Patchanee Chammingkwan* and *Assoc. Prof. Khanin Nueangnoraj* for his valuable support and supervision for the minor research project.

Throughout the duration of this doctoral research at JAIST, the author expresses gratitude to *Rajashekar Badam* and *Assistant Prof. Bharat Srimitra Mantripragada* for their support, advice, and contributions to this thesis. The author expresses his gratitude to *Mr. Noriyuki Takamori* for making the author as an international student life easier in Japan. Additionally, the author extends thanks to all former and present members of the *Matsumi laboratory* for their ongoing encouragement, assistance, collaboration, and during this doctoral research.

The author wishes to express my profound gratitude to his cherished family members. Their unwavering love, support, and encouragement have been the source of my strength and happiness throughout the completion of this thesis. Additionally, I extend my heartfelt appreciation to all Thai members at JAIST who has helped alleviate my feelings of loneliness.

Pirapath Arkasalerks

School of Material Science

Japan Advanced Institute of Science and Technology

October 2024

Chapter 1 Introduction

1.1 General Introduction

In the relentless pursuit of sustainable energy solutions, the global scientific community has long recognized the pressing need for advanced energy storage systems to address current technologies' limitations. Among the array of potential candidates, lithium-air batteries (LABs) have emerged as a promising prospect due to their unparalleled theoretical energy density, which surpasses that of the prevalent lithium-ion [1]. This remarkable potential stems from the fact that Li-air batteries utilize atmospheric oxygen as a reactant, thereby significantly reducing the weight and volume of the required cathode materials.

However, despite the promising theoretical advantages, the practical realization of Li-air batteries remains fraught with multifaceted challenges [2]. Issues such as poor cycling stability, limited lifespan, and unresolved side reactions have hindered their commercial viability and widespread adoption [3]. Consequently, the imperative for rigorous research and development efforts aimed at overcoming these obstacles cannot be overstated.

The significance of advancing Li-air battery technology extends beyond mere incremental improvements; it holds the potential to catalyze transformative shifts in various sectors ranging from transportation and grid storage to portable electronics. By enabling higher energy densities and extended operational lifespans, the successful development of Li-air batteries could substantially accelerate the global transition towards a more sustainable and carbon-neutral energy landscape. Moreover, the economic implications are profound, with the potential to create new industries, generate employment opportunities, and drive innovation across the supply chain.

In summary, while the conceptual allure of lithium-air batteries as a game-changing energy storage solution is undeniable, realizing this potential necessitates concerted research efforts to address existing challenges. By fostering interdisciplinary collaboration and leveraging cutting-edge scientific advancements, the scientific community stands on the cusp of unlocking the transformative capabilities of Li-air batteries, thereby paving the way for a more sustainable and energy-efficient future.

Abstract

This research work focuses on the utilization of a bio-based polymer-derived nitrogen-doped carbon as a support for $CoFe_2O_4$ nanoparticles electrocatalyst in Li-air battery application. This work also showcases the electrocatalyst's bifunctional ability to perform robust electrochemical performances. Nowadays lithium-air batteries (LABs) have emerged as a promising prospect due to their unparalleled theoretical energy density of 3,505 $Whkg^{-1}$. However, despite the promising theoretical advantages, issues such as poor cycling stability, limited lifespan, and unresolved side reactions have hindered their commercial viability and widespread adoption. The major challenges of LABs are sluggish oxygen kinetics from oxygen reduction reaction (ORR) and oxygen evolution reaction (OER) are major issues that hinder their performance. Hence, developing electrocatalysts to promote ORR/OER is essential to reach the theoretical performance of LABs.

In this study, we introduced spinel cobalt iron oxide ($CoFe_2O_4$) nanoparticles decorated on bio-derived pyrolyzed poly(2,5-benzimidazole) (PYPBI800) as a nitrogen-doped carbon support electrocatalyst for LABs. The electrocatalyst was synthesized through pyrolysis of PBI followed by incipient wetness impregnation calcination on the metal precursors. The Strong Metal-Substrate Interaction (SMSI) between $CoFe_2O_4$ and PBI800 has been confirmed with X-ray photoelectron spectroscopy. Due to both the intrinsic properties of $CoFe_2O_4$ and the nitrogen doping effect, these electrocatalysts also modulate the electronic state of metals, facilitating oxygen adsorption and desorption at the electrode.

The electrocatalysts were evaluated as air-breathing electrodes in a CR-2032 coin-type cell LABs compared with other types of carbon supports. The initial discharge capacity for LAB coin cells with $CoFe_2O_4$ on PBI800 was observed to be 18,356 $mAhg^{-1}$. Furthermore, the cycling stability of the $CoFe_2O_4$ on PBI800 cathode was tested through 200 charge-discharge cycles at 400 mAg^{-1} with 1,000 $mAhg^{-1}$ cut-off capacity. The resulting cycle-life data revealed that the battery maintains a discharge capacity as high as 100% even after the 200th cycle, demonstrating exceptional stability with overpotential remains consistently low at 140 mV throughout the examined cycle. The extensive surface area with N heteroatom defects of the PBI provides abundant nucleation sites for $CoFe_2O_4$ nanoparticles which serve as active sites for ORR and OER. The $CoFe_2O_4$ nanoparticles formed on the support exhibit strong metal-substrates interaction which leads to high exceptional stability and electrocatalytic activity.

Based on these findings, the $CoFe_2O_4$ nanoparticles on bio-based polymer-derived nitrogen-doped carbon suggested through this hold promise as a practical air-breathing electrode for high-performance rechargeable LABs. This work will also benefit future heteroatom-doped carbon support design, specifically nitrogen to enhance LABs performance.

Keywords: Oxygen Reduction Reaction, Oxygen Evolution Reaction, Metal Nanoparticles, Lithium Air Battery, Nitrogen Doped Carbon.

Preface

This thesis is consolidation of results of the doctoral research works on the topic of "$CoFe_2O_4$ nanoparticles on bio-based polymer derived nitrogen doped carbon as bifunctional electrocatalyst for Li-air battery". This work was carried out under the supervision of Professor Noriyoshi Matsumi at the School of Materials Sciences, Japan Advanced Institute of Science and Technology during October 2021 – September 2024.

Energy storage is crucial in our modern society for a variety of reasons. It plays a vital role in balancing the supply and demand of electricity, ensuring a stable and reliable power supply. Energy storage not only improves the efficiency of power grids but also reduces the reliance on fossil fuels, contributing to a more sustainable and environmentally friendly energy landscape. Lithium-air batteries (LABs) are a promising option among various battery technologies, primarily due to their remarkable theoretical energy density. LABs utilize oxygen from the atmosphere as a reactant. However, their practical application is impeded by several issues, including poor cycling stability, limited lifespan, and unresolved side reactions. The main difficulties are associated with the air cathode, which consists of porous material for Li_2O_2 storage and electrocatalysts to aid oxygen reduction and evolution reactions. The development of effective electrocatalysts is key to unlocking the full theoretical potential of LABs.

The work presented in this thesis covers the synthesis of $CoFe_2O_4$ nanoparticles on bio-based polymer derived nitrogen doped carbon and their application as electrocatalyst materials for oxygen reduction reaction and oxygen evolution reaction in non-aqueous Li-air batteries. The thesis concludes with a final chapter that encapsulates all the research conducted and offers perspectives on the potential future uses of pyrolyzed poly(2,5-benzimidazole) in electrocatalytic applications.

Pirapath Arkasalerks

School of Material Science

Japan Advanced Institute of Science and Technology

October 2024

Table of Contents

Abstract iii

Preface v

Table of Figures viii

Acknowledgement x

Chapter 1 Introduction 1

1.1 General Introduction 1

1.2 Oxygen Reduction Reaction and Oxygen Evolution Reaction in Aqueous Electrolyte 2

1.2.1 Oxygen Reduction Reaction in Aqueous Electrolyte 2

1.2.2 Oxygen Evolution Reaction in Aqueous Electrolyte 5

1.3 Oxygen Reduction Reaction and Oxygen Evolution Reaction in Nonaqueous Li-Air Batteries 6

1.3.1 Oxygen Reduction Reaction as Discharge in Li-Air Batteries 6

1.3.2 Oxygen Evolution Reaction as Charge in Li-Air Batteries 9

1.4 Catalysts for Li- air battery 10

1.4.1 Noble metal 11

1.4.2 Carbon-based 12

1.4.3 Transition-metal oxides 14

1.5 Strong Metal-Substrates Interaction 19

1.6 Introduction to Poly(2,5-benzimidazole) 21

1.7 Electrochemical Performance Testing 22

1.7.1 Rotating Disk Electrode 22

1.7.2 Cyclic Voltammetry 25

1.7.3 Linear Sweep Voltammetry 26

1.7.4 Electrochemical impedance spectroscopy 27

1.8 Li-air Battery Evaluation 28

1.9 Research Outlook 29

References 30

Chapter 2 $CoFe_2O_4$ Nanoparticles on Bio-based Polymer Derived Nitrogen Doped Carbon as Bifunctional ORR/OER Electrocatalyst in Nonaqueous Electrolyte. 38

Abstract 38

2.1 Introduction 38

2.2 Experimental 41

2.2.1 Synthesis of Pyrolyzed Poly(2,5-benzimidazole) 41
2.2.2 Decoration of $CoFe_2O_4$ on PYPBI800 42
2.2.3 Characterization of Electrocatalyst 42
2.2.4 Electrochemical Characterization 42
2.3 Results and Discussion 43
2.3.1 Characterisation of Electrocatalysts 43
2.4 Electrocatalytic Performance of Electrocatalysts 57
2.5 Conclusions 60
References 61
Chapter 3 $CoFe_2O_4$ Nanoparticles on Bio-based Polymer Derived Nitrogen Doped Carbon as Bifunctional Electrocatalyst for Li-air Battery 65
Abstract 65
3.1 Introduction 65
3.2 Experimental 67
3.2.1 Electrocatalyst Preparation 67
3.2.2 Characterisation of Electrocatalyst 68
3.2.3 Electrochemical Characterisation 68
3.2.4 Li−Air Battery Fabrication and Testing 69
3.3 Results and Discussion 69
3.3.1 Characterisation of Electrocatalysts 69
3.3.2 Electrocatalytic Performance of Electrocatalysts 70
3.3.3 Li-Air Battery Evaluation 73
3.4 Post-mortem Analysis 77
3.5 Conclusions 79
References 79
Chapter 4 Conclusion 82
4.1 General Conclusion 82
4.2 Future Prospects 84

Table of Figures

Figure 1.1 ORR pathways mechanism in acidic electrolyte[7]. 3
Figure 1.2 ORR pathways mechanism in alkaline electrolyte[8]. 4
Figure 1.3 OER mechanism pathways in acidic and alkaline electrolytes[9]. 6
Figure 1.4 ORR mechanism pathways on cathode in non-aqueous LAB 7
Figure 1.5 OER mechanism pathways on cathode in non-aqueous LAB 9
Figure 1.6 ORR volcano plot of noble metal electrocatalysts 12
Figure 1.7 SEM images of a) α-MnO_2 and β-MnO_2 and initial discharge of LAB employing various type of MnO_2 as cathode in c) LiPF6/PC electrolyte and d) LiTFSI/TEGDME[67] . 16
Figure 1.8 TEM images and histograms of the Pt NP size distribution of a) Pt/PANIlong750 and b) Pt/PANIlong1000 21
Figure 1.9 Synthesis of polymer poly(2, 5-benzimidazole) (2,5-PBI) from DABA[108] 22
Figure 1.10 Rotating Disk Electrode with three electrodes system configuration. 23
Figure 1.11 K-L plot from RDE which use to determine the number of electrons transferred 25
Figure 1.12 Example of cyclic voltammogram for electrochemically reversible one-electron redox process [110] 25
Figure 1.13 Example of CV potential waveform [111]. 26
Figure 1.14 Comparison of a) Linear sweep voltammetry (LSV) and b) cyclic voltammetry waveforms[112]. 27
Figure 1.15 Experimental and simulated impedance spectra showing a simplified Randles equivalent circuit for an electrochemical system. [114] 28
Figure 1.16 LAB evaluation including a) cycle stability test, b) initial discharge capacity, and c) LAB efficiencies and overpotential[116]. 29
Figure 2.1 SEM images of a) PBI800, b) Fe PBI, c) Co PBI, d)20%$CoFe_2O_4$ PBI, e) 10%$CoFe_2O_4$ PBI, and f) 30%$CoFe_2O_4$ PBI 45
Figure 2.2 SEM-EDS Mapping images of PYPBI800 a) Depicted area for EDS elemental mapping. b) Carbon c) Nitrogen 45
Figure 2.3 SEM-EDS Mapping images of Fe PBI a) Depicted area for EDS elemental mapping. b) Carbon c) Nitrogen d) Oxygen e) Iron 46
Figure 2.4 SEM-EDS Mapping images of Co PBI a) Depicted area for EDS elemental mapping. b) Carbon c) Nitrogen d) Oxygen e) Cobalt 46
Figure 2.5 SEM-EDS Mapping images of 10%$CoFe_2O_4$ PBI a) Depicted area for EDS elemental mapping. b) Carbon c) Nitrogen d) Oxygen e) Iron f) Cobalt 47
Figure 2.6 SEM-EDS Mapping images of 20%$CoFe_2O_4$ PBI a) Depicted area for EDS elemental mapping. b) Carbon c) Nitrogen d) Oxygen e) Iron f) Cobalt 47
Figure 2.7 SEM-EDS Mapping images of 30%$CoFe_2O_4$ PBI a) Depicted area for EDS elemental mapping. b) Carbon c) Nitrogen d) Oxygen e) Iron f) Cobalt 48
Figure 2.8 XRD patterns corresponded to Fe PBI, Co PBI, 20%$CoFe_2O_4$ PBI, and PBI800 . 49
Figure 2.9 a) HR-TEM image, b) lattices fringes, and c) SAED pattern of 20%$CoFe_2O_4$ PBI 49
Figure 2.10 XPS survey spectra for a) PYPBI800, b) 20%$CoFe_2O_4$ Graphite, c) Co PBI, d) Fe PBI, e) 10%$CoFe_2O_4$ PBI, and f) 20%$CoFe_2O_4$ PBI 52

Figure 2.11 XPS spectra of PYPBI800, 20%$CoFe_2O_4$ Graphite, Co PBI, Fe PBI, 10%$CoFe_2O_4$ PBI, and 20%$CoFe_2O_4$ PBI at a) C 1s region and b) N 1s region. 53
Figure 2.12 XPS spectra at O 1s region of PYPBI800, 20%$CoFe_2O_4$ Graphite, Co PBI, Fe PBI, 10%$CoFe_2O_4$ PBI, and 20%$CoFe_2O_4$ PBI 54
Figure 2.13 XPS spectra of PYPBI800, 20%CoFe2O4 Graphite, Co PBI, Fe PBI, 10%CoFe2O4 PBI, and 20%CoFe2O4 PBI at a) Co 2p region and b) Fe 2p region. 55
Figure 2.14 CV plot comparing a) different metal content and b) different metal loading at 1600 rpm at a scan rate of 50 mVs^{-1} in 0.1 M LiTFSI in TEGDME under O_2 atmosphere. ... 59
Figure 2.15 Coulombic efficiency of electrocatalyst calculated from CV at 1600 rpm at a scan rate of 50 mVs^{-1} in 0.1 M LiTFSI in TEGDME under O_2 atmosphere. 59
Figure 2.16 Potentiostatic electrochemical impedance spectroscopy of electrocatalyst calculated at 1600 rpm in 0.1 M LiTFSI in TEGDME under O_2 atmosphere. 60
Figure 3.1 LSV plot comparing a) ORR on different metals, b), ORR on different $CoFe_2O_4$ content c) OER on different metals d) OER on different $CoFe_2O_4$ content at 1600 rpm at a scan rate of 5 mVs^{-1} in 0.1 M LiTFSI in TEGDME under O_2 atmosphere. 71
Figure 3.2 Tafel plots comparing different metal content in a) ORR and b) OER, and different metal loading in c) ORR and d) OER at 1600 rpm at a scan rate of 5 mVs^{-1} in 0.1 M LiTFSI in TEGDME under O_2 atmosphere 72
Figure 3.3 a)ORR and b)OER mechanism pathways on cathode in non-aqueous LAB 73
Figure 3.4 a) Initial discharge of LABs at the discharge current density of 200 mA g^{-1}, cyclic stability of LABs at current density of 400 mA g^{-1} for b) 1^{st} cycle, and c) 200^{th} cycle. 74
Figure 3.5 Cyclic stability of LABs at current density of 400 mA g^{-1} from 1^{st} cycle to 200^{th} cycle employing a) PYPBI800, b) Co PBI, c) Fe PBI, d) 10%$CoFe_2O_4$ PBI, e) 20%$CoFe_2O_4$ PBI, and f) 30%$CoFe_2O_4$ PBI as cathodes. 75
Figure 3.6 Overpotential and energy efficiency of LABs at current density of 400 mA g^{-1} from 1^{st} cycle to 200^{th} cycle employing a) PYPBI800, b) Co PBI, c) Fe PBI, d) 10%$CoFe_2O_4$ PBI, e) 20%$CoFe_2O_4$ PBI, and f) 30%$CoFe_2O_4$ PBI as cathodes 77
Figure 3.7 XPS results for pristine electrode and electrode after 200 charge-discharge cycles of 20%CoFe2O4 PBI at a) C1s, b) O1s, and c) F1s region 78

Acknowledgement

This research was conducted under the supervision of Professor Noriyoshi Matsumi at the School of Material Science, Japan Advanced Institute of Science and Technology from 2021 to 2024. The author expresses profound appreciation and gratitude to his supervisor, Professor Noriyoshi Matsumi, for his unwavering support and direction throughout this doctoral research.

The author also sincerely thanks the members of the review committee, *Assoc. Prof. Jumpei Ueda, Assoc. Prof. Anh Van Ho, Assoc. Prof. Shun Nishimura and Assoc. Prof. Takeshi Kakibe* for their valuable time, suggestions, and guidance during the process of thesis evaluation.

The author expresses his gratitude to *Prof. Toshiaki Taniike* for allowing him to work in their laboratories for the completion of minor research. The author is also thankful to *Sr. Lecturer Patchanee Chammingkwan* and *Assoc. Prof. Khanin Nueangnoraj* for his valuable support and supervision for the minor research project.

Throughout the duration of this doctoral research at JAIST, the author expresses gratitude to *Rajashekar Badam* and *Assistant Prof. Bharat Srimitra Mantripragada* for their support, advice, and contributions to this thesis. The author expresses his gratitude to *Mr. Noriyuki Takamori* for making the author as an international student life easier in Japan. Additionally, the author extends thanks to all former and present members of the *Matsumi laboratory* for their ongoing encouragement, assistance, collaboration, and during this doctoral research.

The author wishes to express my profound gratitude to his cherished family members. Their unwavering love, support, and encouragement have been the source of my strength and happiness throughout the completion of this thesis. Additionally, I extend my heartfelt appreciation to all Thai members at JAIST who has helped alleviate my feelings of loneliness.

Pirapath Arkasalerks

School of Material Science

Japan Advanced Institute of Science and Technology

October 2024

Chapter 1 Introduction

1.1 General Introduction

In the relentless pursuit of sustainable energy solutions, the global scientific community has long recognized the pressing need for advanced energy storage systems to address current technologies' limitations. Among the array of potential candidates, lithium-air batteries (LABs) have emerged as a promising prospect due to their unparalleled theoretical energy density, which surpasses that of the prevalent lithium-ion [1]. This remarkable potential stems from the fact that Li-air batteries utilize atmospheric oxygen as a reactant, thereby significantly reducing the weight and volume of the required cathode materials.

However, despite the promising theoretical advantages, the practical realization of Li-air batteries remains fraught with multifaceted challenges [2]. Issues such as poor cycling stability, limited lifespan, and unresolved side reactions have hindered their commercial viability and widespread adoption [3]. Consequently, the imperative for rigorous research and development efforts aimed at overcoming these obstacles cannot be overstated.

The significance of advancing Li-air battery technology extends beyond mere incremental improvements; it holds the potential to catalyze transformative shifts in various sectors ranging from transportation, grid storage, and electronic devices. By enabling higher energy densities and extended operational lifespans, the successful development of Li-air batteries could substantially accelerate the global transition towards a more sustainable and carbon-neutral energy landscape. Moreover, the economic implications are profound, with the potential to create new industries, generate employment opportunities, and drive innovation across the supply chain.

In summary, while the conceptual allure of lithium-air batteries as a game-changing energy storage solution is undeniable, realizing this potential necessitates concerted research efforts to address existing challenges. By fostering interdisciplinary collaboration and leveraging cutting-edge scientific advancements, the scientific community stands on the cusp of unlocking the transformative capabilities of Li-air batteries, thereby paving the way for a more sustainable and energy-efficient future.

1.2 Oxygen Reduction Reaction and Oxygen Evolution Reaction in Aqueous Electrolyte

1.2.1 Oxygen Reduction Reaction in Aqueous Electrolyte

The Oxygen Reduction Reaction (ORR) is a fundamental electrochemical process that plays a vital role in diverse energy conversion and storage technologies, such as fuel cells, metal-air batteries, and specific aspects of electrolysis. At its essence, the ORR entails converting oxygen molecules (O_2) from the atmosphere into various products through a sequence of intermediate steps, accompanied by the release of electrons. This redox reaction is inherently complex, involving multiple electron transfer events and intermediate species, which underscores the need for meticulous attention to optimize efficiency and kinetics.

One of the defining characteristics that underscore the significance of the ORR lies in its sluggish nature when compared to other electrochemical reactions, such as the hydrogen evolution reaction (HER). This intrinsic sluggishness poses considerable challenges, particularly in applications where rapid oxygen reduction is essential for maintaining device performance and overall efficiency. Consequently, the development of efficient ORR catalysts and strategies to enhance reaction kinetics has become a focal point of extensive research endeavors spanning disciplines such as materials science, chemistry, and engineering. Currently, the catalysts facilitate ORR in two major pathways including four electrons and two electrons pathway as shown in Table 1.1. Considering ORR in acidic electrolytes, the detailed mechanisms are shown in

Figure 1.1 where * represents the electrocatalyst surface. In the case of $4e^-$ pathway, there are 2 minor mechanisms, including the associative mechanism and dissociative mechanism. The associative mechanism considered the adsorption of the O_2 molecule on the electrocatalyst surface and followed by the formation of OOH* intermediates. At this point, there are two possible pathways for OOH*. First, the OOH* are reduced into OH* and bind with another OH* and form H_2O and another OH*. This OH* is then protonated and produces another molecule of H_2O which 2 molecules of water are formed in total. Second, the OOH* is protonated into O* and H_2O. Then O* is protonated twice into another molecule H_2O. On the other hand, the dissociative mechanism involved the cleavage of O-O bond, and subsequently, the hydrogenation of atomic oxygen (O*) to form OH* and then H_2O where hydrogenation of OH is the rate-limiting step at ORR equilibrium potential at 1.299 V vs

SHE[4–6]. For $2e^-$ pathway, the early steps are like that of the associative mechanism including the adsorption of O_2 and formation of OOH*. Then, OOH* is protonated and forms H_2O_2*. At this point, H_2O_2 might be desorbed or further protonated twice into 2 molecules of H_2O. In the case of ORR in alkaline electrolyte, H_2O is a proton source instead of H^+, and the final product is hydroxide anion and peroxide ion in $4e^-$ and $2e^-$, respectively. The mechanisms of ORR in alkaline electrolyte are shown in Figure 1.2 which have similar associative, dissociative, and $2e^-$ pathway mechanisms to acidic electrolyte. For the associative mechanism, the O_2 is adsorbed and protonated and form OOH* with OH^-. Then, the OOH* binds with OH^- and form $2OH^-$ with O*. This O* is also protonated by H_2O into OH* and another OH^-, and OH* is desorbed from the surface which made totally $4OH^-$ over the processes. In this pathway, the intermediate OOH* might get desorbed as the product from $2e^-$ pathway. For the dissociative pathway, after the O-O bond cleavaging, each O* is protonated with H_2O which made total 4 protons and electrons transferred obtaining 2OH* and $2OH^-$. Then, The OH* is desorbed resulted as $4OH^-$ in total.

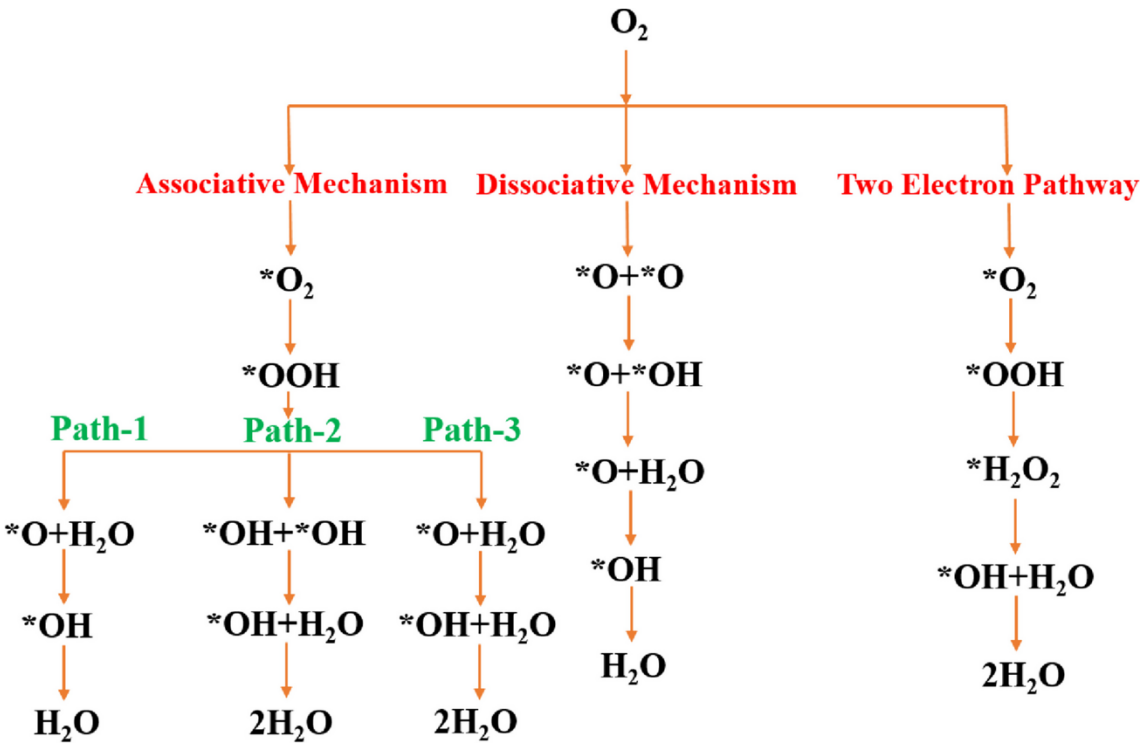

Figure 1.1 ORR pathways mechanism in acidic electrolyte[7].

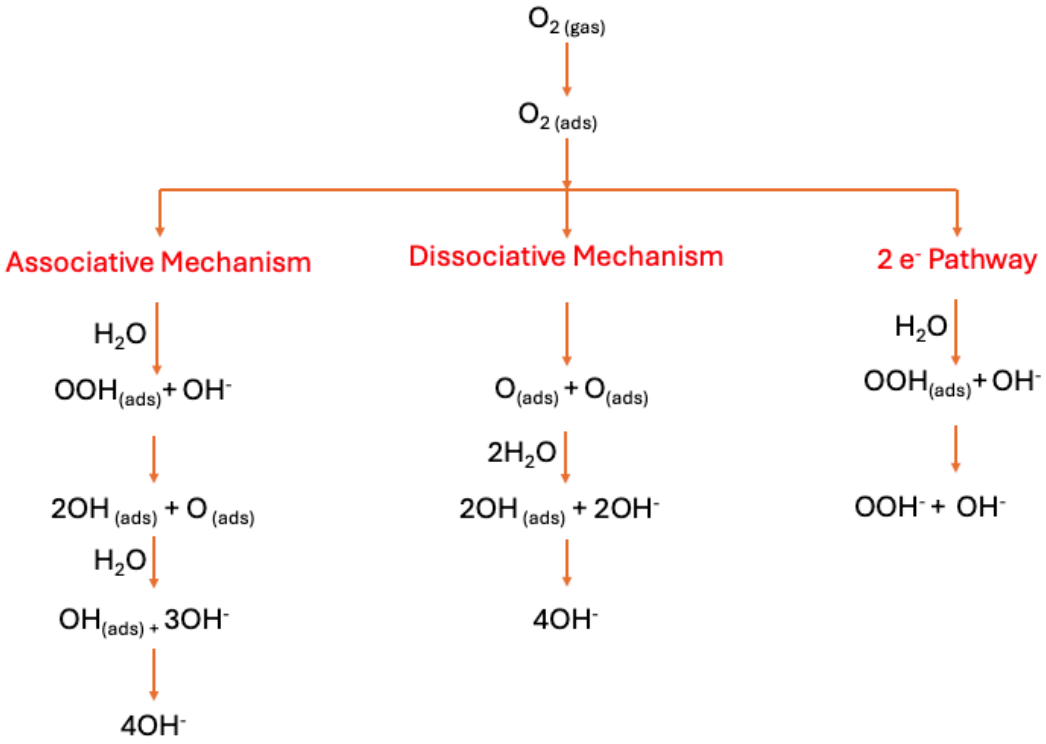

Figure 1.2 ORR pathways mechanism in alkaline electrolyte[8].

Table 1.1 Mechanism of ORR in various electrolytes

Electrolyte	ORR	Thermodynamic electrode potential at 25°C and 1 atm (V vs SHE)
Acidic aqueous electrolyte	$O_2 + 4H^+ + 4e^- \rightarrow H_2O$ $O_2 + 2H^+ + 2e^- \rightarrow H_2O_2$ $H_2O_2 + 2H^+ + 2e^- \rightarrow 2H_2O$	1.229 0.70 1.76
Alkaline aqueous electrolyte	$O_2 + H_2O + 4e^- \rightarrow 4OH^-$ $O_2 + H_2O + 2e^- \rightarrow HO_2^- + OH^-$ $HO_2^- + H_2O + 2e^- \rightarrow 3OH^-$	0.401 -0.065 0.867
Non-aqueous electrolyte	$O_2 + e^- \rightarrow O_2^-$ $O_2^- + e^- \rightarrow O_2^{2-}$	Electrolytes dependence

1.2.2 Oxygen Evolution Reaction in Aqueous Electrolyte

The Oxygen Evolution Reaction (OER) serves as a corners tone in the realm of electrochemistry, offering a vital pathway for the generation of oxygen gas (O_2) from ORR products through an intricate series of redox processes. This pivotal reaction, often related to its counterpart, the ORR, holds paramount significance in a multitude of energy conversion and storage applications. Unlike the ORR, which involves the reduction of oxygen, the OER necessitates the oxidation of water molecules to liberate oxygen, making it an indispensable process for sustainable energy generation.

Despite its fundamental importance, the OER is inherently challenging from an electrochemical perspective due to its sluggish kinetics and the need for robust catalysts to facilitate the reaction efficiently. The complexities associated with the OER arise from the multi-step nature of the reaction, involving proton-coupled electron transfer events, intermediate species formation, and intricate surface interactions, which collectively dictate the overall efficiency and stability of the process.

In OER, there are 2 possible pathways from the O* intermediate for both electrolytes as shown in Figure 1.3. Starting from H_2O as ORR product in acidic electrolyte, the H_2O absorbed on the electrocatalyst surface and released H^+ and e^- into OH* Then, OH* is deprotonated into O* and desorbed as O_2 from the surface. On another pathway, after the deprotonation of OH* into O*, it is oxidized with H_2O into *OOH intermediate followed by oxidation into O_2 and desorbed from the surface. Similarly, in alkaline electrolyte, OH^- is absorbed on the electrocatalyst surface, then deprotonates into O*, before desorbing off the surface. For another pathway, the O* is oxidized to OOH* and follows a similar process with an acidic electrolyte.

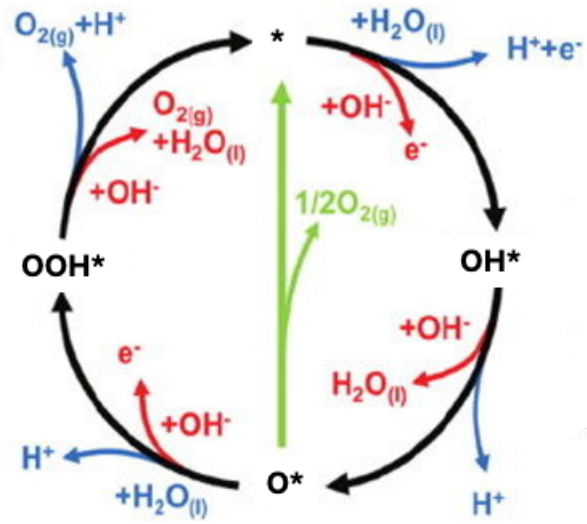

Figure 1.3 OER mechanism pathways in acidic and alkaline electrolytes[9].

1.3 Oxygen Reduction Reaction and Oxygen Evolution Reaction in Nonaqueous Li-Air Batteries

Earlier studies in electrochemistry explored the possibility of reducing molecular oxygen to superoxide (O^{2-}) within organic solvents during the ORR in a nonaqueous electrolyte. Predominant research efforts on ORR and OER nonaqueous electrolytes are directed toward Li^+ nonaqueous electrolytes (consisting of organic solvents and lithium-containing salt), primarily due to their pivotal role in the mechanism of Li–air (O_2) batteries (LABs). A fundamental nonaqueous LABs comprises several essential components. These include a lithium metal anode, a separator, and a porous carbon-based cathode soaked in electrolytes. The carbon cathode serves as a structural framework rather than an active material, according to its lightweight nature, affordability, excellent electrical conductivity, and high chemical stability. ORR take place during discharge, O_2 in the atmosphere interact with lithium ions together with electrons at the cathode, resulting in the formation of a solid reaction product—typically lithium peroxide (Li_2O_2)—which accumulates within the carbon framework pores. During charging, Li_2O_2 decomposes as OER producing O_2 back to the atmosphere.

1.3.1 Oxygen Reduction Reaction as Discharge in Li-Air Batteries

During discharge at the cathode surface of LAB. ORR is shown in equation (1), with the equilibrium voltage of 2.96 V vs Li^+/Li[10]. There are two possible pathways for ORR in LAB including the surface mechanism or solution-mediated pathway[11–14]. These pathways

are illustrated in Figure 1.4, where the subscription of "(cat)" and "(sol)" referred to the species adsorbed on the surface of the cathode and dissolved in the solution, respectively.

In the solution-mediated pathway, $O_{2(g)}$ is adsorbed on the surface which forms LiO_2 and diffuses into the solution. The diffused $LiO_{2(sol)}$ is dissolved into Li^+ and O_2^-. However, the solubility in organic electrolytes is considerably low. So, instead of dissolving, disproportionation of $LiO_{2(sol)}$ takes place and forms $Li_2O_{2(sol)}$ and $O_{2(g)}$. The $Li_2O_{2(sol)}$ is precipitated which can be observed from the Li_2O_2 particles on the LAB separators. On the other hand, in the surface mechanism pathway, $O_{2(g)}$ is adsorbed on the surface which forms $LiO_{2(cat)}$ similarly, remains at the cathode surface instead of diffusing into the solution. Then, $LiO_{2(cat)}$ is further reduced into $Li_2O_{2(cat)}$, hence it can observe the deposited Li_2O_2 particles on the cathode surface.

$$2Li_{(s)} + O_{2(g)} \leftrightarrow Li_2O_{2(s)}, \quad E^0 = 2.96\ V\ Li^+/Li \tag{1}$$

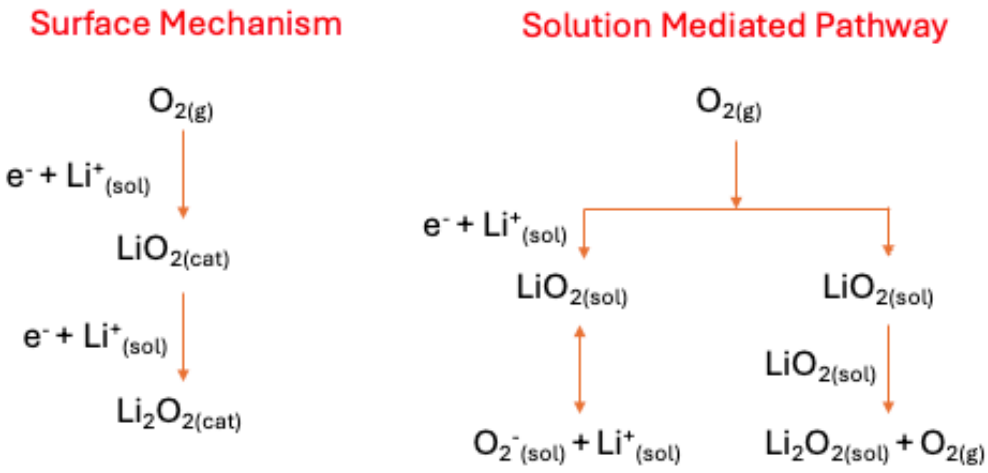

Figure 1.4 ORR mechanism pathways on cathode in non-aqueous LAB

Comparing these two mechanisms, the solution-mediated mechanism is preferred, due to the formation of Li_2O_2 on the cathode surface being limited. On the cathode surface, it is believed that when all active surfaces become covered with a thick layer of Li_2O_2[15,16], which acts as an insulator, the discharge process ends. Thus, the tunnelling current through Li_2O_2 is no longer able to sustain electrochemical current[17–20]. At this point, there is a significant drop in current which is called "sudden death" which indicates the termination of

cell discharge. This is a critical factor due to its direct effect on the achievable energy density of the LAB. Apart from the cathode, this rapid electrochemical polarization can similarly arise at the Li anode. Research groups have demonstrated that during the discharge of LAB with ether type electrolytes, additional by-products such as LiOH, Li_2CO_3, and Li_2O formed and accumulated on the Li anode due to electrolyte decomposition and formed solid electrolyte interface (SEI) which can mitigate the decomposition of the electrolyte[21–23]. However, low lithium-ion conductivity SEI layer can significantly raise charge transfer impedance at the anode and lead to a sudden death phenomenon. Electrochemical impedance spectroscopy (EIS) data further demonstrated that the impedance related to electronic transport through Li_2O_2, deposited at the cathode, experiences a significant increase during the "sudden death" phase of discharging[24]. In contrast, the impedance associated with the anode's SEI shows only a minor increase. This suggests that the sudden death is primarily governed by electronic transport through the Li_2O_2 layers covering the cathode surface.

The LAB discharge is dependent on various factors, including the donor number (DN) or acceptor number (AN) of electrolytes, choice of Li^+ salt and additives that can stabilize O_2^-, the use of redox mediators, operating temperature and pressure, or multiple factors. The main aim of modifying these factors is to promote $Li^+_{(sol)}$ and $O_{2(sol)}$ or $LiO_{2(sol)}$. In the case of DN and AN of electrolytes, it has been investigated that high DN solvent and high AN additives enhance the dissolution of LiO_2 into Li^+ and O_2^-, and lead to formation of large toroidal $Li_2O_{2(sol)}$ which increased the LAB discharge capacity. However, solvents with high DN such as dimethylformamide (DMF)[25] or N-methyl pyrrolidone (NMP) [26] suffered against nucleophilic attacks by superoxide and peroxide species[27], and resulted in low stability or rechargeability compared to ethers[27] or acetonitrile[28]. Apart from the electrolytes and additives, the choice of lithium salt anion can play an important role in stabilizing Li^+ in the solution. Another potential strategy is to use redox mediators which can shift the Li_2O_2 precipitation reaction zone away from the surface. However, increasing the solubility of LiO_2 or Li_2O_2 might cause the reaction to occur far from the cathode and lead to difficulties during the charge process which requires Li_2O_2 to be nearby the cathode surface[29]. Enhancing the performance of LABs necessitates a comprehensive approach that considers all architectures of the cell.

1.3.2 Oxygen Evolution Reaction as Charge in Li-Air Batteries

In the charging process, the mechanisms are not a simple reverse process of discharging. It involved different electrochemical profiles and higher overpotential. The

possible mechanisms are shown in Figure 1.5. The process includes either solid-solution decomposition or liquid-phase mediation. Solid-solution decomposition includes the decomposition of $Li_2O_{2(s)}$ into $LiO_{2(s)}$ and dissolves into the electrolyte as $LiO_{2(sol)}$. Then, $LiO_{2(sol)}$ is further oxidized into O_2 gas while comproportionating of $LiO_{2(sol)}$ to form $Li_2O_{2(sol)}$ and O_2 gas take place in the liquid phase mediation pathway. There is also a case where the mechanism begins from the dissolution of Li_2O_2 into the electrolyte. Then, the process is followed by a direct $2e^-$ transfer. Besides, the $Li_2O_{2(sol)}$ could undergo a single e^- transfer process to form $LiO_{2(sol)}$ and comproportionate into $Li_2O_{2(sol)}$ and O_2 gas similarly. It thus suggests that either decomposition or dissolution of $Li_2O_{2(s)}$ is the dominant step governing the charging overpotential.

The high overpotential is caused by several problems at the different charging current rates. At a lower rate, the electrocatalyst surface becomes coated with Li_2O_2 and other byproducts resulting from parasitic reactions, which possess insulating properties. Additionally, the porous structure of the electrode may become clogged due to the accumulation of these byproducts. At higher charging rates, Li_2O_2 detaches from the surfaces, leading to increased resistance between Li_2O_2 and the electrocatalyst surface. Furthermore, Li metal anode degradation can occur because of an unstable solid electrolyte interface (SEI) layer.

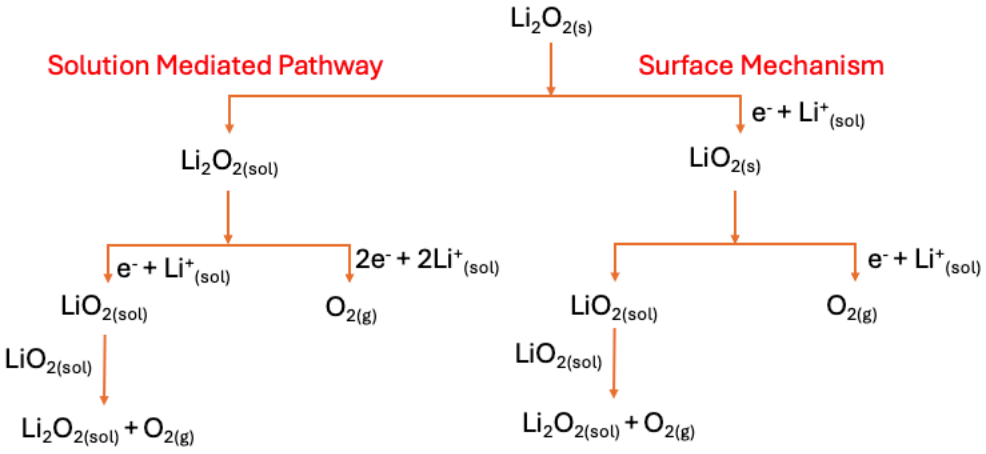

Figure 1.5 OER mechanism pathways on cathode in non-aqueous LAB

While the exact reaction mechanism remains incompletely understood, both ORR and OER occur at the surfaces of LAB's cathodes. Hence, it plays a critical role in enhancing energy density for LABs. Despite their potential, commercialization of LABs has not yet arose according to challenges associated with cathodes. Porous structures are essential for

LAB's cathode to facilitate easy electrolyte uptake and prevent pore-clogging caused by Li_2O_2 formation which led to increased ORR/OER overpotentials[30]. Similarly, in order to achieve high discharge capacity which determines the LAB energy density, the cathode should have a property of large surface area where numerous Li_2O_2 could deposited[31,32]. Also, the cathode is needed to be highly conductive, to achieve high chemical and electrochemical stability, and high electrocatalytic activity. These properties lead to superior electronic conductivity, preventing residual Li_2O_2 products after repetitive discharge and charge[33,34]. Therefore, it is necessary to uniformly decorate efficient electrocatalysts on highly conductive support materials to decompose the deposited Li_2O_2 at a cathode after discharge, resulting in enhanced round-trip efficiency of OER and ORR. Additionally, decomposition of carbon cathode, electrolyte, binder, trace water as parasitic reactions could generate undesirable by-products including Li_2CO_3 and LiOH which possess insulative properties cover the cathode surface and reduce LAB efficiency[35–37]. As these parasitic species occurred at higher charging potential, the electrocatalyst which reduces the overpotential is necessary. Considering these challenges, LAB cathode plays a major role in the commercialization of LAB. Thus, the development of electrocatalyst for the cathode to address these challenges is essential.

1.4 Catalysts for Li- air battery

The aprotic LAB consists of several components, including the cathode, anode, separator, and electrolyte. Among these, the cathode plays a critical role in the direct electrochemical reactions and significantly impacts the formation of Li_2O_2. The absorption of O_2 and the reaction between O_2 and Li^+ occur at the cathode catalyst sites. For optimal electrochemical performance, cathode catalysts should exhibit good catalytic activity, provide sufficient space for storing discharge products, and offer efficient channels for oxygen and charge transport. Therefore, thoughtful design and construction of cathode materials are essential for enhancing electrochemical performance and advancing the commercial use of aprotic Li-O_2 batteries.

1.4.1 Noble metal

In the past few decades, significant progress has been made in the development of non-precious metals for various electrochemical reactions[38–40]. To date, noble metals continue to be crucial in electrocatalysis applications because of their exceptional catalytic abilities. Numerous studies suggest that the platinum (Pt) is the most effective noble metal

electrocatalyst for ORR and hydrogen evolution reaction (HER) [41,42]. Additionally, catalysts made of ruthenium (Ru) and iridium (Ir) oxides are known to exhibit advantageous reaction kinetics for OER[43,44] Efforts to reduce the use of noble metals and improve their catalytic effectiveness have led to the creation of innovative and highly efficient noble metal electrocatalysts. It's widely recognized that nanostructured noble metals offer significant benefits in electrocatalysis over their bulk forms[45,46]. Nanomaterials feature a vast surface area and experience size-dependent quantum effects. As the particle size shrinks to the nanometer scale, the catalytic performance is notably enhanced due to a greater number of accessible surface atoms and adjustments in the proportion of undercoordinated atoms. When reduced to the atomic scale, active sites become maximally exposed on the surface, allowing for their full utilization in catalysis[47]. In an early study of LABs, researchers observed that Au/C exhibited the highest charge activity, while Pt/C demonstrated exceptionally high discharging activity. To combine the advantages of both materials, they synthesized PtAu nanoparticles with Au and Pt on their surfaces[48]. They investigated their oxygen reduction reaction (ORR) and oxygen evolution reaction (OER) activity when supported on carbon in LAB cells. Surprisingly, the PtAu/C catalyst exhibited highly active bifunctional behaviour, contributing to the efficient round-trip efficiency of rechargeable LABs. While this research focused on a PC/DME electrolyte where parasitic reactions could occur, the concept of enhancing specific atoms (like Pt and Au) with varied properties on nanoparticle exteriors shows potential for creating exceptionally effective bifunctional catalysts in LABs. Subsequently, these researchers explored the electrocatalytic activity of ORR on four polycrystalline noble metal surfaces including Pd, Pt, Ru, and Au. The electrolyte used was 0.1 M $LiClO_4$ in 1,2-dimethoxyethane with rotating disk electrode as the working electrode. They found that the ORR activity in nonaqueous Li^+ electrolyte significantly correlates with the oxygen adsorption energy, resulting in a 'volcano-type' trend[49] as shown in Figure 1.6. Moreover, Ru-decorated vertically aligned graphene nanosheets (VGNS) on Ni foam (Ru-decorated VGNS@Ni foam) serve as an effective cathode catalyst for lithium-oxygen (Li-O_2) batteries. The Ni foam acts as a framework structure and current collector, while the VGNS with a high surface area promotes O_2 molecule adsorption. The Ru catalyst and carbon defects contribute to reducing O_2 to O_2^-, leading to the formation of toroid-shaped Li_2O_2 particles (~500 nm in size). The decomposition of Li_2O_2 into Li^+ and O_2^- occurs at the electrocatalyst surface active sites such as Ru nanocrystals (Ru NCs) and vacancies in the VGNS. The multifunctional Ru-decorated VGNS/Ni foam-based cathode exhibits high discharge and charge capacities exceeding 5,000 $mAhg^{-1}$ at a current density of 200 mAg^{-1}, with a very low

charge overpotential (~450 mV). However, the significant expense of materials and the limited availability of resources in the Earth's crust pose major challenges that greatly hinder the industrial scalability of noble metals electrocatalysts. Therefore, parameters such as price, processing, cathode material properties, and electrochemical performance must be carefully considered and prioritized.

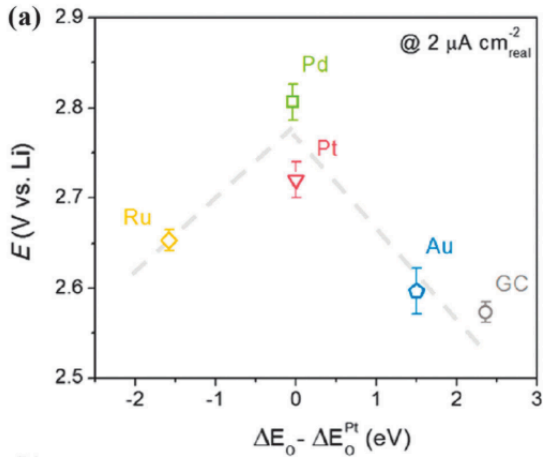

Figure 1.6 ORR volcano plot of noble metal electrocatalysts

1.4.2 Carbon-based

In LABs, the cathode are the combination of porous support materials and highly conductive materials. The term "support material" refers specifically to a porous framework designed to stored Li_2O_2 during ORR prior to the decomposition it during OER. The properties of these support materials such as morphology, electronic conductivity, chemical stability, and oxygen adsorption characteristics significantly affect LABs performance[50,51]. Notably, an insoluble discharge product (mainly Li_2O_2) forms and deposits on the surface of the supports. Therefore, the structure of these cathode materials must be carefully designed to accommodate the solid product and facilitate oxygen gas diffusion and electrolyte penetration[52]. However, creating porous support materials with sufficient conductivity and high mechanical stability remains a challenge due to their inherent fragility and reduced conductivity[53]. Porous carbon-based materials are commonly studied for LAB cathodes because of their high electronic conductivity, high porosity, lightweight, and earth abundant[54].

Commercial carbon blacks such as Super P, Vulcan XC-72, or Ketjen black have been employed as the porous structure for LAB cathode. Research has shown that the discharge capacity of LAB is significantly affected by the pore size and volume of carbon powders, more so than the surface area of the carbon powder[55]. Eight different types of carbon

electrodes with varying pore sizes and volumes have been investigated by Lui and co-workers[55]. The findings revealed that while super P carbon which exhibits a low surface area of about 62 m^2g^{-1} exhibited good performance, an activated carbon (with a higher surface area of about 1200 m^2g^{-1}) achieved a capacity of approximately 1900 $mAhg^{-1}$, which is much lower than that of super P. A simulation was used to explain how carbon pore size influences LAB capacity and the formation of Li_2O_2. The studies also indicated that carbon remains stable when the charge potential is below 3.5 V (vs Li/Li+). However, irreversible by-product, Li_2CO_3, could be formed at charge potentials higher than 3.5 V, leading to the decomposition of carbon cathode[35]. Apart from amorphous carbon, other carbon structures have also been investigated. For instance, single-wall carbon nanotubes (SWCNTs) were employed as cathode catalysts in LABs which were able to achieve the capacity of 1600 $mAhg^{-1}$ [56]. These CNTs exhibited higher capacities compared to carbon black, graphite, and activated carbon. However, compared with aligned multi-wall carbon nanotubes (MWCNTs), featuring controllable pore structures[57], were integrated into the CNT fibril as cathode for LABs. During the initial 20 cycles, these electrodes exhibited a capacity exceeding 2500 $mAhg^{-1}$. Additionally, graphene mesosponge (GMS) synthesized using the advanced template technique followed by high-temperature annealing at 1800 °C has been employed as binder-free LAB cathode[58]. As the GMS possess edge site free, the active sites for ORR and OER are the topological defects. These defects are the non-hexagonal carbon in the graphene framework. The LABs with GMS cathode exhibit an initial discharge capacity of up to 6700 $mAhg^{-1}$ at 0.2 $mAcm^{-2}$. The LAB shows extremely long stability up to 307 cycles. Heteroatom doping is another defects modification strategy to improve the electrocatalytic activity of the LAB cathode. Hu et al. proposed that ORR activity of carbon material originates from the activation of carbon π electrons, achieved by modification the integrity of π conjugation through heteroatom doping. This activation can be quantitatively correlated with the electronegativity of the dopants[59]. The electronegativity difference between carbon and dopants significantly influences the ORR. Additionally, the modified charge distribution resulting from doped carbon affects the wettability of carbon-based materials. This wettability adjustment is crucial for the typical three-phase reaction which is mainly in the ORR process on the air-cathode of metal–air batteries[60]. Ensuring good contact between catalysts and the non-aqueous electrolyte enhances charge transfer rates and improves ORR activity. The doping of carbon material could vary from single dopant to multiple dopant which have different effects on ORR and OER activity. For example, N doped graphene exhibits an initial

discharge capacity of 7300 $mAhg^{-1}$ at 50 mAg^{-1}. The stability for this material was considerably low which is 22 cycles with the cut-off capacity of 500 $mAhg^{-1}$ at 100 mAg^{-1} [61]. On the other hand, N, S doped mesoporous carbon on graphene nanosheet has been employed as the cathode in LAB[62]. The initial discharge was enhanced up to 11500 $mAhg^{-1}$ at 100 mAg^{-1}. The stability was also improved and reached 100 cycles at 50 mAg^{-1} with a cut-off capacity of 250 $mAhg^{-1}$. Decorating metal nanoparticles on carbon is another wide strategy to improve ORR and OER in LAB. This strategy provides the benefits in several ways including minimizing amount of metals content, improving stability, agglomeration mitigation, and enhance ORR/OER electro catalytic activity. Therefore, carbon materials are mostly acting as porous support material which could be modified in many ways to provide synergistic effects on LAB performance.

1.4.3 Transition-metal oxides

Transition-metal oxides form a diverse group of oxygen electrocatalysts, encompassing both mono-metal oxides and mixed-metal oxides. Compared to noble metals, transition-metal oxides offer several advantages, including abundant availability, cost-effectiveness, ease of preparation, and environmental friendliness. Moreover, these transition-metal oxides possess various crystal structures due to the multiple valence states of transition-metal elements. In the following sections, three different types of transition-metal oxide electrocatalysts based on their composition and structure will be explore.

1.4.3.1 Single metal oxide

The most prevalent transition metal elements as electrocatalysts for ORR and OER include Fe, Co, and Mn. However, additional transition elements, such as scandium (Sc), have also demonstrated remarkable catalytic potential in electrode reactions [63]. Manganese oxides have garnered significant attention according to their variable valences and abundant structural diversity, resulting in rich redox electrochemistry. These oxides can serve simultaneously as catalysts for both the ORR and OER[64], making them attractive bifunctional catalysts for oxygen electrochemistry. The most studied group of manganese oxides is manganese dioxide (MnO_2). MnO_2, first reported in the early 1970s for the ORR, has since been the focus of extensive research efforts aimed at evaluating and optimizing MnO_x-based catalysts for air cathodes[65]. Researchers have explored various factors, including chemical composition, texture, morphology, oxidation state, and crystalline structure, to enhance the electrocatalytic properties of MnO_2. The bifunctional activity of MnO_2 is significantly influenced by the specific crystal phase of the oxide[66]. For example,

A non-aqueous LAB constructed with β-MnO_2 nanowires exhibited a higher discharge capacity (approximately 2500 $mAhg^{-1}$) compared to a LAB utilizing α-MnO_2 nanowires[67] as shown in Figure 1.7.

In general, ORR performance of MnO_2 is typically better than OER performance[68]. Hence, enhancing the OER activity is crucial for overall performance improvement. Recent research has demonstrated that the vacancy defect engineering method positively influences the OER activity of δ-MnO_2. Briefly, ultrathin nanosheets of δ-MnO_2 (NS-MnO_2) were grown on the surface of nickel foam, resulting in a high concentration of oxygen vacancies and Mn^{3+} active sites. These defects enhance H_2O adsorption, leading to an electrocatalyst with a low overpotential and a smaller Tafel slope—lower even than that observed for commercial IrO_2[69].

Cobalt oxides (CoOx) are promising candidates for LABs given their outstanding bifunctional electrocatalytic activity, especially the spinel oxide Co_3O_4. In a typical spinel structure of Co_3O_4, Co^{2+} and Co^{3+} ions occupied in tetrahedral and octahedral sites, respectively[70]. Researchers have found that electrocatalysts with more Co^{2+} on the surface is more active toward ORR performance, while the OER activity is elevated from a higher number of Co^{3+} sites on the surface[71]. This elevated activity can be corresponded to the improved adsorption of O_2 at Co^{2+} sites and OH^- at Co^{3+} sites[72]. Consequently, the arrangement of Co^{2+} and Co^{3+} ions on the surface of Co_3O_4 electrocatalysts plays a significant role in optimizing bifunctional electrocatalytic activity. Some researchers have pointed out that Co_3O_4 polyhedrons enclosed by {112} facets possess higher bifunctional catalytic activities for ORR and OER compared to octahedrons enclosed by {001} and {001}+{111} facets. This result is corresponded to the optimised ratio of Co^{2+}/Co^{3+} active sites and the presence of octahedrally coordinated Co^{3+} ions[73]. Zhao and colleagues recently explored a solvent-mediated method to control the structures of Co_3O_4 nanostructures. By adjusting the mole ratio of water and dimethylformamide of the solution, they produced rod-shaped and spherical nanostructures. Interestingly, Co_3O_4 nanorods posess the best electrocatalytic activity for ORR among all the electrocatalyst samples prepared under different conditions. Their catalytic activity for the ORR was higher than that of the noble palladium catalyst. This finding suggests that the number and activity of surface-exposed Co^{3+} ions can be controlled by the structure of the cobalt oxides[74].

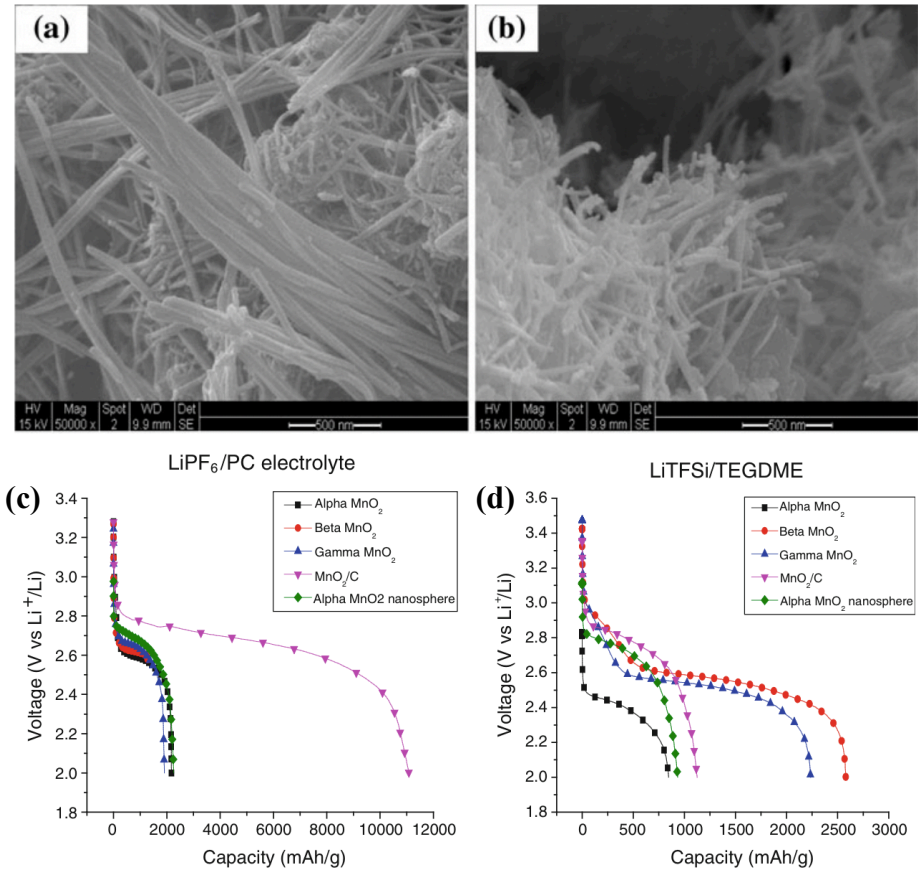

Figure 1.7 SEM images of a) α-MnO_2 and β-MnO_2 and initial discharge of LAB employing various type of MnO_2 as cathode in c) LiPF6/PC electrolyte and d) LiTFSI/TEGDME[67]

1.4.3.2 Mixed-metal oxide

The presence of additional metal ions can introduce more active sites, leading to higher intrinsic activity in mixed-metal oxides compared to single-metal oxides for ORR and OER[75]. Moreover, the activity of the electrocatalyst can be readily optimized by adjusting factors such as crystalline structure, valence, and electronic states of each metal element[76]. In this section, polymetallic spinel, and perovskite oxides as bifunctional electrocatalysts will be focused on, highlighting their excellent performance and widespread use in electrocatalysis and metal-air batteries.

Spinel

The structure of spinel oxides (denoted as AB_2O_4, where A and B represent transition metal ions) comprises B^{3+} ions occupying octahedral sites and A^{2+} ions occupying tetrahedral sites. Within this structure, there are numerous disordered sites due to cation arrangement. Even small structural changes significantly impact the performance of ORR and OER[77].

Researchers have designed and synthesized a highly efficient hierarchical porous structure three-dimensional $MnCo_2O_4$ nanowire using the hydrothermal method. This

nanowire was employed as a carbon-free and binder-free cathode for LABs, the initial discharge capacity reached 12,919 $mAhg^{-1}$ at 0.1 $mAcm^{-2}$. Furthermore, at higher rates of 0.2, 0.5, and 1.0 $mAcm^{-2}$, the initial discharge capacities were measured as 10,146, 7112, and 4771 $mAhg^{-1}$, respectively, highlighting the superior rate capability of the $MnCo_2O_4$ nanowire catalysts. As the cathode in LABs, the $MnCo_2O_4$ nanowire exhibited an overpotential of approximately 0.54 V with a cut-off capacity of 500 $mAhg^{-1}$ at 0.1 $mAcm^{-2}$. Remarkably, the cell operated for over 300 cycles under these conditions. Even with a 1000 $mAhg^{-1}$ cut-off capacity, the nanowire demonstrated 144 stable charge and discharge cycles at 0.1 $mAcm^{-2}$. The unique hierarchical interconnected mesoporous/macroporous weblike structure of the hybrid $MnCo_2O_4$/Ni foam cathode was identified as the primary reason for its excellent electrochemical performance.

Ultrathin porous $NiCo_2O_4$ nanosheets containing oxygen vacancies have been employed as cathode catalysts in LABs[78]. these nanosheets exhibit an initial discharge capacity of up to 16,400 $mAhg^{-1}$ at 200 mAg^{-1}. At the cut-off capacity of 1000 $mAhg^{-1}$, the battery maintains stability over 150 cycles. The electrochemical performance is further enhanced by a unique solution mechanism involving the electrochemical double layer at the cathode-electrolyte interface.

Additionally, microspheres containing a $NiCo_2O_4$@CeO_2 composite have been used as cathodes in LABs[79]. This microstructure catalyst provides ample electrocatalytic surface area, facilitating barrier-free transport of oxygen and Li^+. The microsphere's porous structure accelerates electrolyte penetration and enables reversible deposition and dissolution of Li_2O_2. The introduction of CeO_2 enhances oxygen vacancies and optimizes the electronic structure of $NiCo_2O_4$, resulting in improved electron transport throughout the entire electrode. As a result, this catalytic cathode material significantly reduces the overpotential to only 1.07 V and exhibits impressive cycle stability over 400 cycles at 500 mAg^{-1}. Beyond these materials, there are other spinel-structured compounds, such as $CuCo_2O_4$ nanotubes[80], $MnCo_2O_4$ nanotubes[81], and $MnCo_2O_4$/MoO_2 nanocomposites [82], which also demonstrate excellent catalyst performance for LABs.

The flexible crystal structure of spinel materials allows for easy doping to modify electrocatalytic performance. Nevertheless, the precise relationship between structure and electrocatalytic activity remains an area of ongoing research. Investigating the mechanism of

electrocatalytic activity, along with advancements in structural chemistry and controllable preparation methods, remains crucial for applied research in LABs.

Perovskite

Perovskite-type transition metal oxides, with the general formula ABO_3, have undergone extensive research due to their bifunctional electrocatalytic properties in alkaline electrolytes. These materials exhibit a wide range of properties, which can be controlled by partially substituting either A or B cations with other metals. A-site substitution affects the ability to adsorbed oxygen, while B-site substitution impacts the activity of the adsorbed oxygen[83,84]. Substituted perovskites are described by the formula $A_{1-x}A'_xB_{1-y}B'_yO_3$, where A or A' represents a rare-earth or alkaline-earth metal, and B or B' represents a transition metal. The cations' ability to adopt different valency states significantly influenced the electrocatalytic activity of transition metal oxide catalysts, specifically when they form redox couples during oxygen reduction/evolution reactions. As a result, various perovskite-type transition metal oxides with different substitution have been explored as bifunctional electrocatalysts[85,86].

$CaMnO_3$, known for its good electrocatalytic performance, exhibited a reduced overpotential of approximately 0.62 V at 50 mAg^{-1} when used as an electrocatalyst in LAB's cathode [87]. The 3D ordered macroporous $LaFeO_3$ cathode (3DOM-LFO), gaining from both porosity and higher electrocatalytic activity, demonstrated a stable charge and discharge performance of up to 124 cycles[88]. Additionally, porous $LaNiO_3$ nanocubes[89], serving as the air electrode in LABs, maintained stability over 75 cycles with a cut off capacity of 500 $mAhg^{-1}$ at 0.08 $mAcm^{-2}$. Moreover, introducing defects into the perovskite structure can improve electrocatalytic activity. Researchers have compared $CaMnO_3$, both in its pristine form and with induced defects, serves as a cathode catalyst in LABs[90]. When evaluated alongside a redox mediator LiI, the oxygen-deficient $CaMnO_3$ exhibits an improved cycle life at a high current rate of 500 mAg^{-1}, with a capacity of 500 $mAhg^{-1}$. The introduction of defects predominantly enhances catalytic activity by reducing the overpotential. The presence of oxygen vacancies leads to mixed-valence states of Mn^{3+}/Mn^{4+}, which modify the electronic structure and contribute to improved electrocatalytic performance.

1.4.3.3 Supporting Metal oxide with carbon material

In electrochemical reactions, perovskite and spinel metal oxides encounter two primary challenges similar to other metal oxides. Firstly, the particles of metal oxides tend to agglomerate together, reducing the number of active sites available. Secondly, they

demonstrate poor electrical conductivity, which hampers electron transfer and diminishes their electrocatalytic effectiveness. To overcome these issues, researchers have investigated approaches such as synthesizing nanostructured materials or developing materials with a porous structures. In both instances, supporting the metal oxides with other materials is crucial to enhance electrical conductivity and maximize exposure of active sites to the electrolyte. Carbon materials are particularly suitable for this purpose due to their inherent characteristics, such as high electrical conductivity, thermal stability, extensive surface area, and, in some cases, cost-effectiveness. Various types of carbon materials have been employed, including carbon blacks, carbon nanotubes, graphene-based materials, activated carbons, and nitrogen-doped carbon materials. For instance, researchers have investigated the electrocatalytic performance of Mn_2O_3 supported with carbon black, MWCNTs, catalytic filamentous carbon and pyrolytic carbon. The results show that both the accessibility of metal oxide surfaces for charge-transfer reactions and the oxide/carbon interface extension are improved by carbon support with moderate specific surface area, such as Vulcan carbon black and pyrolytic carbons[91]. Similarly, Kostuch and co-workers have demonstrated the effects of carbon support by the in-situ synthesis of $MnCo_2O_4$ on carbon blacks, MWCNTs, mesoporous carbon, and amorphous carbon. It is reported that MWCNTs performed best according to the higher particle dispersion, higher exposition of Co^{3+} and Mn^{2+} sites, and higher amorphous content which led to favor peroxide formation. It can be seen that carbon supports play an important role regulating electrocatalytic performance of LAB. Therefore, carbon support should be rationally designed and investigated.

1.5 Strong Metal-Substrates Interaction

Recently, researchers have focused on the interaction between the supported metal and carbon support which provide synergies effects that enhance the electrochemical properties of the electrocatalyst. This interaction is called “strong metal-substrates interaction” or “strong metal-support interaction” (SMSI)[92]. SMSI was initially discovered by Tauster et al in 1978. The researchers found that the CO and H_2 chemisorption on Pt decorated on TiO_2 disappeared after the reduction treatment at 500 °C[92]. This phenomenon is reported to be caused by the electronic perturbation of Pt-Ti bond which describes SMSI, however, it was later confirmed that the metal nanoparticles were encapsulated by the support which led to the disappearance of the chemisorption properties[93–97]. In 1986, SMSI evidence was illustrated using extended X-ray absorption fine structure spectroscopy (EXAFS)[97]. EXAFS provided that the bond length between formed Rh-TiO_2 was shorter than Rh-Ti compound.

This shorter bond length emphasizes the “strong” in SMSI. However, SMSI identification has remained to be done by physicochemical behaviors such as encapsulation or chemisorption ability.

In the case of carbon support materials, SMSI in heterogenous catalysts has been confirmed to improve the electrocatalytic performance of ORR and OER[98–100]. In case of ORR, researchers found that SMSI characterized by XPS indicating Pt strongly anchoring to carbon, facilitates efficient electron transfer to reactants. Additionally, the moderate strength of Pt-oxygen coordination (due to SMSI) enables easy desorption of intermediates and the final product or H_2O [100]. Similarly, SMSI was investigated with N doped carbon supports, besides metal oxide supports. N doped carbon supports improve the catalysts in every aspect including providing nucleation sites with better dispersion at graphitic-N, metal nanoparticles anchoring and dispersants at pyridinic-N sites[101]. Moreover, SMSI shows significant impacts in both ORR and OER. In ORR, N doped carbon nanofibers were employed as support for Pt nanoparticles[102]. The electrocatalyst indicates great improvement in ORR electrocatalytic activity. Using NEXAFS spectroscopy, Melke et al demonstrated that Pt interacts with N containing groups in the precursor which is polyaniline (PANI). This interaction shifts electrons from Pt nanoparticles into the π-conjugated system. This electron shifting increase the electron density in the π-conjugated system. Consequently, the N-defects serve as nucleation sites for Pt nanoparticles, explaining the high Pt dispersions observed via TEM measurements as shown in Figure 1.8. Additionally, the electronic interaction significantly affects PANI nanofibers (NFs) carbonization, influencing the resulting N-doped carbon nanofibers (N-CNFs) structure. Notably, in the presence of Pt, a larger number of PANI chains contribute to forming the carbon network. Further analysis using NEXAFS spectroscopy and XPS revealed changes in the Pt’s electronic structure according to its interaction with N-defects. Interestingly, the Pt dispersion observed in both N-CNFs suggested that different N-functionalities may interact with Pt. This results in a uniform particle size facilitated by interactions with pyridinic-N in Pt/PANIlong750. Conversely, N-CNFs predominantly containing graphitic-N (Pt/PANIlong1000) possess a broad particle size distribution with a larger mean particle size.

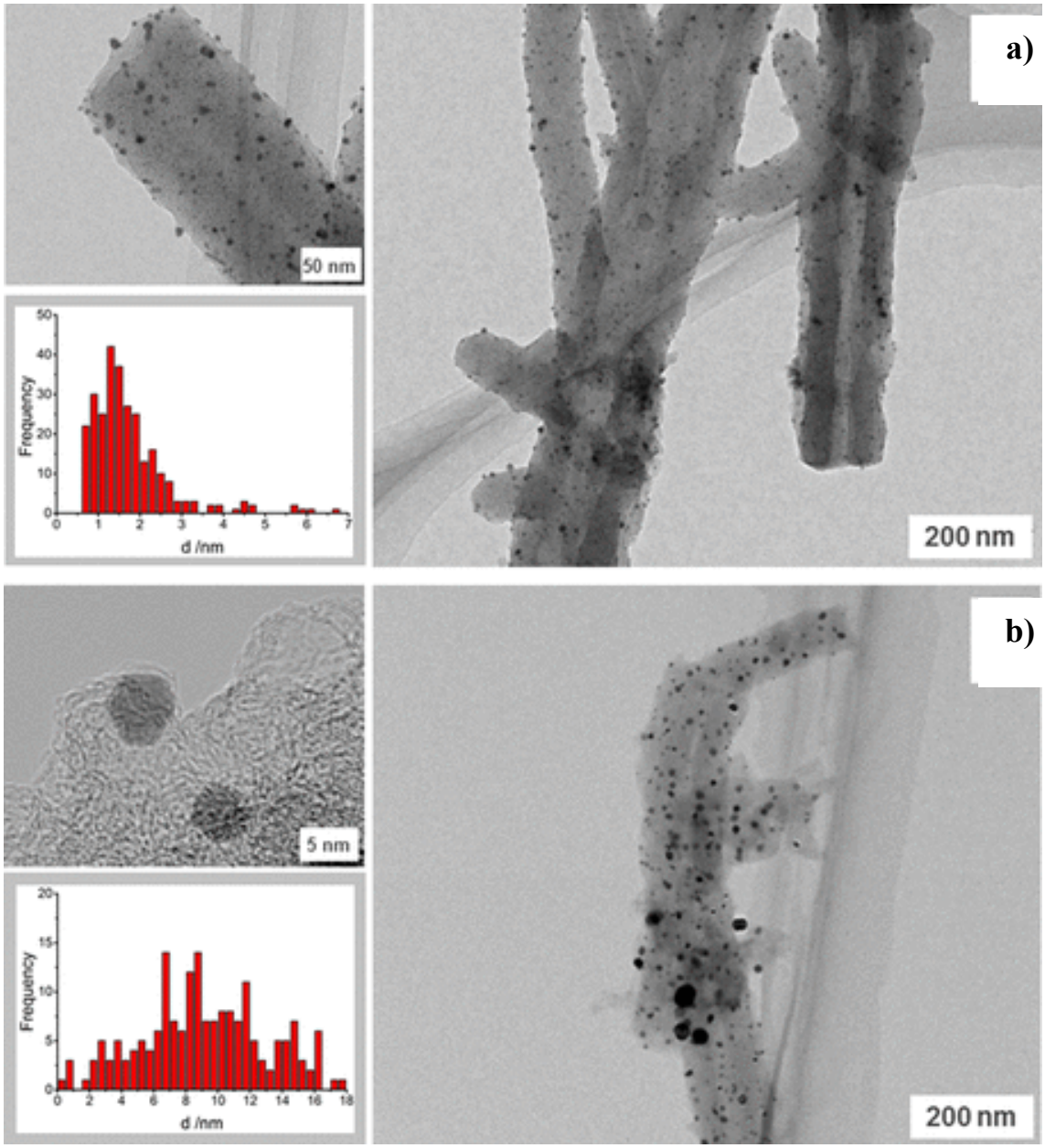

Figure 1.8 TEM images and histograms of the Pt NP size distribution of a) Pt/PANIlong750 and b) Pt/PANIlong1000

1.6 Introduction to Poly(2,5-benzimidazole)

According to the previous section, SMSI effects are different among various N functionalities such as graphitic N improve metal nanoparticle dispersion, while pyridinic provides anchoring sites for metal nanoparticles[102]. Thus, it is crucial to design and develop the desired N doped carbon support in both physical and chemical aspects. One of the strategies to develop the desired properties of carbon support is utilizing polymer-based carbon. Given the ongoing advancements in polymer nanomaterials, polymers offer great potential for producing diverse carbon materials with varying morphologies. These polymers can initially be processed into intricate structures and subsequently form selective porous

networks through intrinsic phase separation. Additionally, by incorporating heteroatoms, the electronic properties of these hybrid polymer-carbon materials (HPCMs) can be deliberately tailored for specific applications[103]. However, these polymers typically produced from fossil-based carbon, involve olefin and aromatics building blocks which are recognized that lead to global warming. Hence, to produce more sustainable polymers, researchers have extensively explored converting bio-feedstocks into compounds that closely resemble those derived from petroleum[104,105]. Poly(2,5-benzimidazole) (ABPBI) is a highly promising conductive polymer for carbon precursors. Its simple preparation process involves a single monomer[106], making it an attractive choice. The repeating unit of ABPBI contains only one benzimidazole moiety, resulting in a higher N-H group density[107]. Bio-derived ABPBI was prepared from 3,4-diaminobenzoic acid (DABA) monomers as shown in Figure 1.9 which were converted from 3-amino-4-hydroxybenzoic acid (AHBA). AHBA is synthesized from kraft pulp, an inedible cellulosic material, using genetically modified bacteria[108]. After pyrolysis of ABPBI, it leads to significant nitrogen doping in the carbon structure.

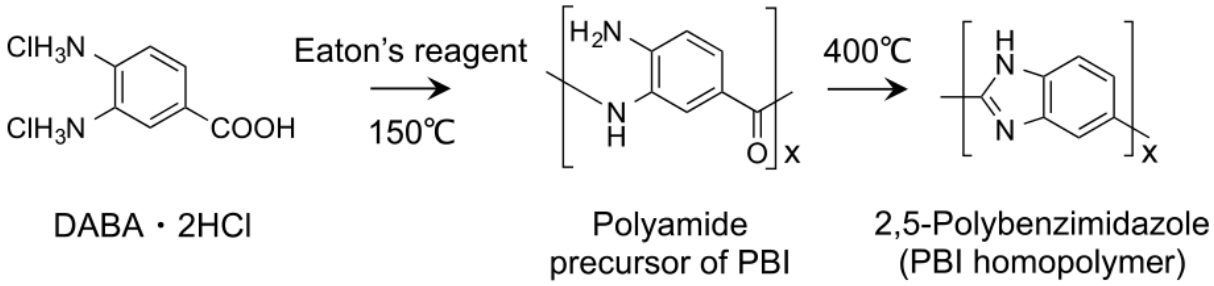

Figure 1.9 Synthesis of polymer poly(2, 5-benzimidazole) (2,5-PBI) from DABA[108]

1.7 Electrochemical Performance Testing

1.7.1 Rotating Disk Electrode

The rotating disk electrode (RDE) as shown in Figure 1.10 is an electroanalytical technique employed to mitigate the impact of mass transfer for analytes converted from precursors. The concept originates from the rotating disk electrode, which induces centrifugal movement of the electrolyte solution toward the radial ring. As the electrode's rotation rate increases, so does the convection velocity of the electrolyte solution. Consequently, the diffusion layer near the electrode becomes thinner, leading to enhanced reactions toward the electrochemical product. RDE is valuable for calculating parameters related to the diffusion-convection process[109].

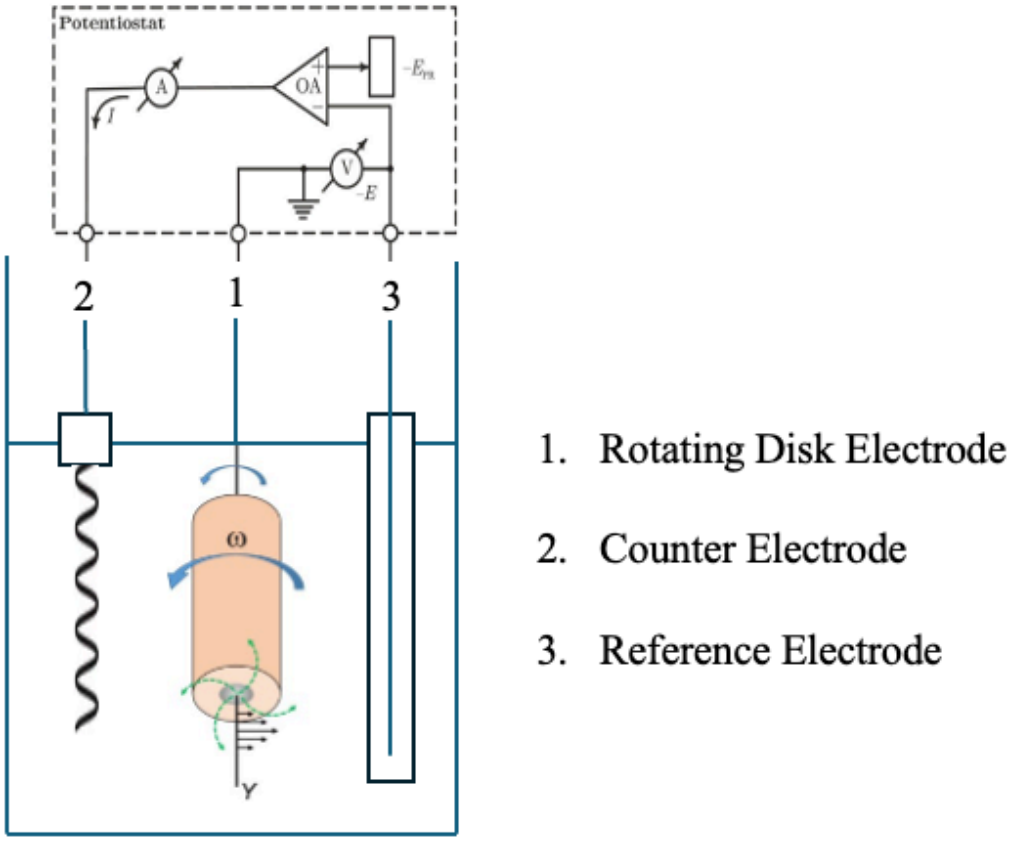

Figure 1.10 Rotating Disk Electrode with three electrodes system configuration.

This method finds widespread use in studying electrocatalytic oxygen reduction reactions (ORR) by assessing reaction efficiency. Researchers can investigate reaction kinetics, as the diffusion effect of the studied species is already accounted for. Additionally, the instrument facilitates the determination of kinetic viscosity, exchange current density, and the number of electrons transferred.

In this technique, the solution near the RDE rotates along with the RDE. When observed from the RDE as a frame of reference, the solution appears stagnant. The thickness of this stagnant layer (δ_H) can be estimated using the following formula in equation (2)

$$\delta_H = 3.6\left(\frac{\nu}{\omega}\right)^{\frac{1}{2}} \quad (2)$$

where ν is kinematic viscosity, ω is the rotational speed of RDE.

In this method, ions move from the bulk solution to the stagnant layer primarily through convection, while their transport to the electrode surface relies solely on diffusion.

Consequently, this technique completely avoids convection. The diffusion layer also possesses a specific thickness, which can be measured using equation (3)

$$\delta_f = 1.61 D^{\frac{1}{3}} \nu^{\frac{1}{6}} \omega^{-\frac{1}{2}} \quad (3)$$

From the diffusion layer specific thickness in equation (3), the diffusion limiting current can be calculate from equation (4)

$$i_l = 0.0620 nFAD^{\frac{2}{3}} \nu^{-\frac{1}{6}} \omega^{\frac{1}{2}} C \quad (4)$$

To determine the number of electron transfers, the Koutecky-Levich (K-L) equation can be used as shown in the equation (5). From the given equation (6), the number of electron transfers (n) can be calculated from the slope (BL) of the linear K-L plot as shown in Figure 1.11

$$\frac{1}{i} = \frac{1}{i_k} + \frac{1}{i_l} = \frac{1}{i_k} + \frac{1}{B_L \omega^{\frac{1}{2}}} \quad (5)$$

$$B_L = 0.0620 nFAD^{\frac{2}{3}} \nu^{-\frac{1}{6}} C \quad (6)$$

Where il is the diffusion limiting current (A)

ik is the kinetic current density (A)

C is the bulk concentration of O2 (mol cm^{-3})

F is the Faraday's constant (96485 $Cmol^{-1}$)

A is the electrode surface area (cm^2)

D is the diffusion coefficient of O_2

n is the number of electron transfer

ν is the kinematic viscosity of the electrolyte ($cm^2 s^{-1}$)

ω is the angular rotational speed (rad s^{-1})

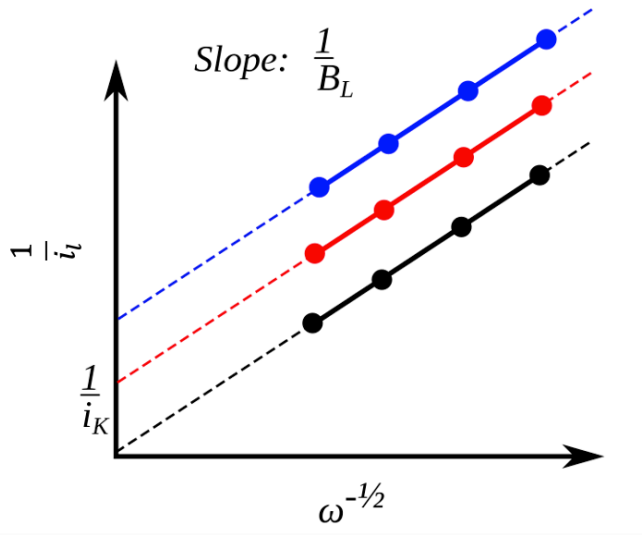

Figure 1.11 K-L plot from RDE which use to determine the number of electrons transferred

1.7.2 Cyclic Voltammetry

Cyclic Voltammetry (CV) is an electrochemical measurement used to observe redox processes' current response to a cycled potential between the set values. CV can explain the electrochemical behavior of each molecular species as a form of voltammogram. The voltammogram shows the redox peaks of the materials for the oxidation and reduction process. This data can be used to predict the element's ability for redox reaction, the electrochemical kinetics, and other characteristics which are involved in the electrochemical reaction. An example of CV voltammogram is shown in Figure 1.12.

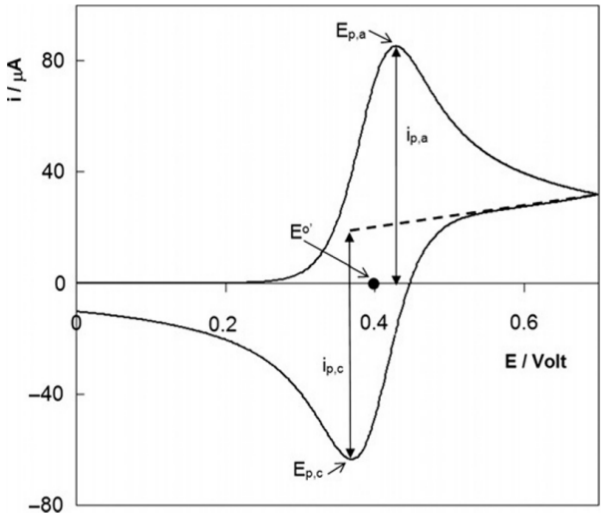

Figure 1.12 Example of cyclic voltammogram for electrochemically reversible one-electron redox process [110]

In three electrodes system, the current flows between working electrodes through the counter electrodes, the measurement of current is done by measuring the current from the working electrode to the reference electrode. The waveform of CV usually tells the potential over time as a peak, and the slope refers to the total potential in the testing. An example of a CV waveform can be seen in Figure 1.13. The composition of an electrolyte, the potential scan rate, and the working electrode status are the factors that affect the moving current that passes through the working electrode in a significant amount.

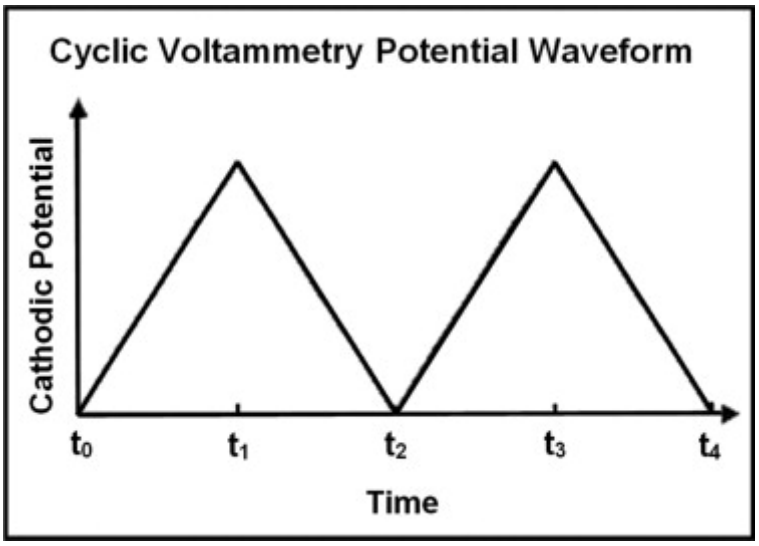

Figure 1.13 Example of CV potential waveform [111].

1.7.3 Linear Sweep Voltammetry

Linear Sweep Voltammetry (LSV) is a fundamental potentiostatic sweep technique. It is similar to a one-segment cyclic voltammetry experiment as shown in Figure 1.14. The working electrode potential is scanned linearly from a lower limit to an upper limit. During this scan, the current at the working electrode is monitored as a function of time. The primary outcome of an LSV experiment is a voltammogram, which depicts the relationship between current and potential. LSV provides both qualitative and quantitative insights into electrochemical systems and serves as a reliable and efficient characterization technique. Additionally, LSV is commonly used to study the kinetics of reactions involving electron transfer processes.

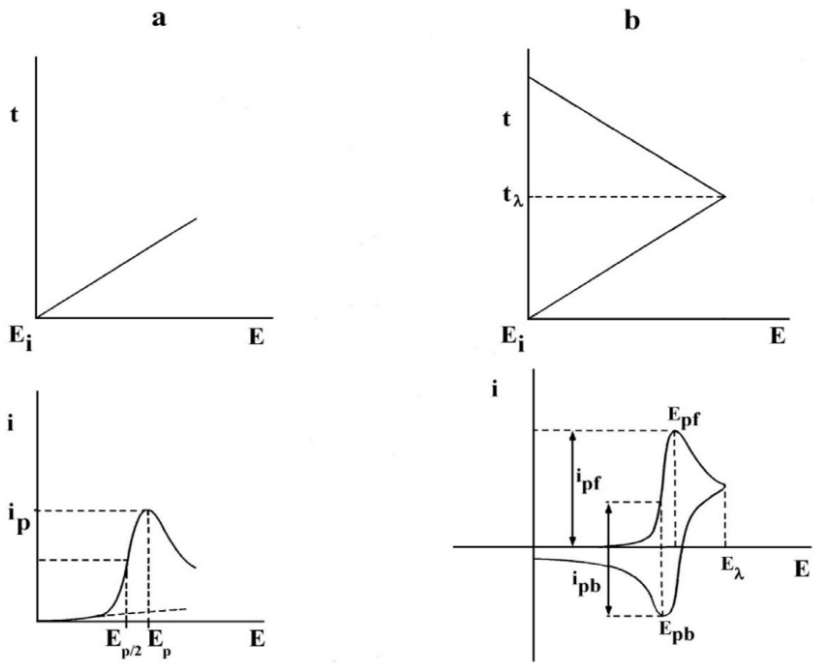

Figure 1.14 Comparison of a) Linear sweep voltammetry (LSV) and b) cyclic voltammetry waveforms[112].

1.7.4 Electrochemical impedance spectroscopy

Electrochemical Impedance Spectroscopy (EIS) is a highly sensitive technique used to characterize chemical systems nondestructively. By applying low amplitude alternating current (AC) voltages across an electrode setup (consisting of working, reference, and counter electrodes), EIS reveals the time response of chemical systems. It provides quantitative insights into small-scale chemical mechanisms at the electrode interface and within the electrolytic solution. However, interpreting EIS spectra can be challenging. Researchers often employ simple fitting models based on equivalent circuit analogues as shown in Figure 1.15 and physical models to extract parameters representing the underlying cell processes[113].

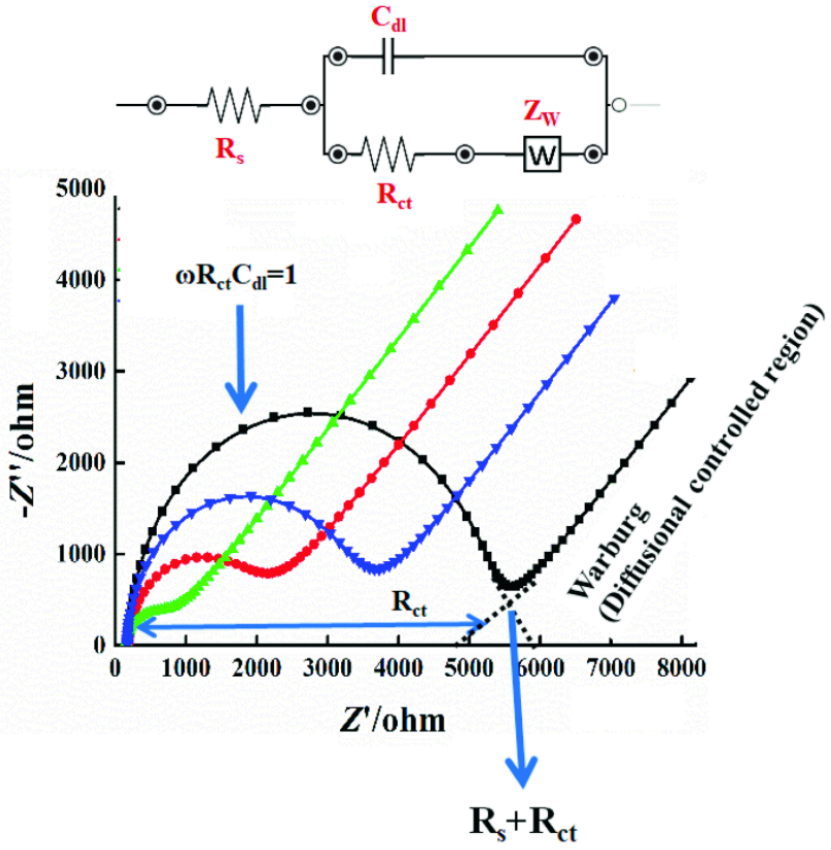

Figure 1.15 Experimental and simulated impedance spectra showing a simplified Randles equivalent circuit for an electrochemical system. [114]

1.8 Li-air Battery Evaluation

Apart from the electrochemical performance of the electrocatalyst tested by the RDE in a non-aqueous electrolyte, the electrocatalysts are employed as cathodes for LAB. The LABs are tested for their initial discharge capacity which significantly affects their energy density. The LAB will be discharged until the potential suddenly drops or the sudden death phenomenon. Furthermore, the LAB's stability is tested with charge-discharge cycles at a certain current rate and cut-off capacity. Then, from the charge-discharge cycles data, the overpotential of the LAB is determined by equation (7).

$$\text{Columbic Efficiency} = \frac{C_{discharge}}{C_{charge}} \tag{7}$$

Similarly, given that batteries serve as energy storage devices, researchers suggest calculating battery efficiency by comparing the output energy to the input energy. The goal is to assess the energy efficiency of the entire charging and discharging process. Therefore, energy efficiency is determined[115] by equation (8).

$$\text{Energy Efficiency} = \frac{\Sigma_{i=0}^{n-1} V_{discharge} \times I_{discharge} \times \Delta t_i}{\Sigma_{i=0}^{n-1} V_{charge} \times I_{charge} \times \Delta t_i} \quad (8)$$

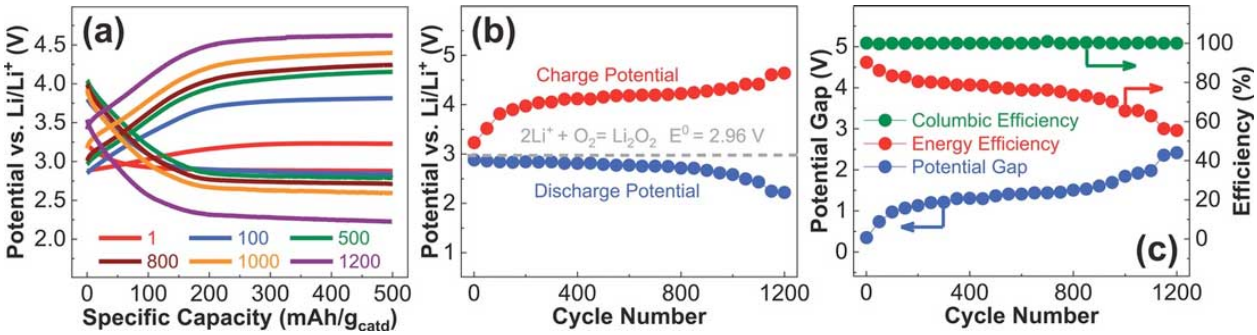

Figure 1.16 LAB evaluation including a) cycle stability test, b) initial discharge capacity, and c) LAB efficiencies and overpotential[116].

1.9 Research Outlook

According to the high theoretical energy density of LAB, it has recently become a highly active and interesting area of research. In this perspective, the mechanism behind LAB charge and discharge was introduced, followed by the discussion of the electrocatalysts that employed as cathode on LABs. According to the literature, the following areas of electrocatalyst for LAB were explored.

1. The design of the electrocatalyst utilizing N-doped carbon as support to explore the effect of strong metal substrate interaction to enhance the performance of LAB.
2. In order to obtain the desired physicochemical properties of N-doped carbon, the bio-based polymer will be used as an N-doped carbon precursor. Thus, the obtained N-doped carbon is environmentally friendly with the desired properties.
3. Spinel-type metal oxides will be supported on the N-doped carbon to enhance the drawbacks of metal oxides. On the other hand, SMSI will play a significant role in improving the LAB performance synergistically.
4. Prior to the LAB evaluation, the electrocatalysts need to be studied with RDE in a non-aqueous electrolyte under O_2 atmosphere.

References

1. J.W. Jung, S.H. Cho, J.S. Nam, I.D. Kim, *Energy Storage Mater*, 24 (2020) 512–528.
2. Y.G. Chirkov, V.I. Rostokin, V.N. Andreev, V.A. Bogdanovskaya, *Russian Journal of Physical Chemistry A*, 96 (2022) 1085–1092.
3. D. Aurbach, B.D. McCloskey, L.F. Nazar, P.G. Bruce, *Nat Energy*, 1 (2016).
4. A.U. Nilekar, M. Mavrikakis, *Surf Sci*, 602 (2008) L89–L94.
5. P. Lang, N. Yuan, Q. Jiang, Y. Zhang, J. Tang, *Energy Technology*, 8 (2020) 1900984.
6. X. Huang, M. Song, J. Zhang, T. Shen, G. Luo, D. Wang, *Nano-Micro Letters 2023 15:1*, 15 (2023) 1–34.
7. S.H. Noh, M.H. Seo, J.K. Seo, P. Fischer, B. Han, *Nanoscale*, 5 (2013) 8625–8633.
8. D.W. Wang, D. Su, *Energy Environ Sci*, 7 (2014) 576–591.
9. I.C. Man, H.Y. Su, F. Calle-Vallejo, H.A. Hansen, J.I. Martínez, N.G. Inoglu, J. Kitchin, T.F. Jaramillo, J.K. Nørskov, J. Rossmeisl, *ChemCatChem*, 3 (2011) 1159–1165.
10. W. Li, C. Han, K. Zhang, S. Chou, S. Dou, *J Mater Chem A Mater*, 9 (2021) 6671–6693.
11. N.B. Aetukuri, B.D. McCloskey, J.M. Garciá, L.E. Krupp, V. Viswanathan, A.C. Luntz, *Nature Chemistry 2014 7:1*, 7 (2014) 50–56.
12. B.D. McCloskey, R. Scheffler, A. Speidel, G. Girishkumar, A.C. Luntz, *Journal of Physical Chemistry C*, 116 (2012) 23897–23905.
13. M.D. Bhatt, J.Y. Lee, *J Mol Liq*, 271 (2018) 274–280.
14. C.O. Laoire, S. Mukerjee, K.M. Abraham, E.J. Plichta, M.A. Hendrickson, *Journal of Physical Chemistry C*, 114 (2010) 9178–9186.
15. O. Gerbig, R. Merkle, J. Maier, *Advanced Materials*, 25 (2013) 3933–3933.
16. F. Tian, M.D. Radin, D.J. Siegel, *Chemistry of Materials*, 26 (2014) 2952–2959.
17. A.C. Luntz, V. Viswanathan, J. Voss, J.B. Varley, J.K. Nørskov, R. Scheffler, A. Speidel, *Journal of Physical Chemistry Letters*, 4 (2013) 3494–3499.

18. V. Viswanathan, K.S. Thygesen, J.S. Hummelshj, J.K. Nrskov, G. Girishkumar, B.D. McCloskey, A.C. Luntz, *Journal of Chemical Physics*, 135 (2011).

19. K.B. Knudsen, A.C. Luntz, S.H. Jensen, T. Vegge, J. Hjelm, *Journal of Physical Chemistry C*, 119 (2015) 28292–28299.

20. P. Albertus, G. Girishkumar, B. McCloskey, R.S. Sánchez-Carrera, B. Kozinsky, J. Christensen, A.C. Luntz, *J Electrochem Soc*, 158 (2011) A343.

21. F. Qiu, X. Zhang, Y. Qiao, X. Zhang, H. Deng, T. Shi, P. He, H. Zhou, *Energy Storage Mater*, 12 (2018) 176–182.

22. R.S. Assary, J. Lu, P. Du, X. Luo, X. Zhang, Y. Ren, L.A. Curtiss, K. Amine, *ChemSusChem*, 6 (2013) 51–55.

23. J.L. Shui, J.S. Okasinski, P. Kenesei, H.A. Dobbs, D. Zhao, J.D. Almer, D.J. Liu, *Nature Communications 2013 4:1*, 4 (2013) 1–7.

24. J. Højberg, B.D. McCloskey, J. Hjelm, T. Vegge, K. Johansen, P. Norby, A.C. Luntz, *ACS Appl Mater Interfaces*, 7 (2015) 4039–4047.

25. Y. Chen, S.A. Freunberger, Z. Peng, F. Bardé, P.G. Bruce, *J Am Chem Soc*, 134 (2012) 7952–7957.

26. B.D. McCloskey, D.S. Bethune, R.M. Shelby, T. Mori, R. Scheffler, A. Speidel, M. Sherwood, A.C. Luntz, *Journal of Physical Chemistry Letters*, 3 (2012) 3043–3047.

27. A. Khetan, A. Luntz, V. Viswanathan, *Journal of Physical Chemistry Letters*, 6 (2015) 1254–1259.

28. R. Younesi, P. Norby, T. Vegge, *ECS Electrochemistry Letters*, 3 (2014) A15.

29. T. Liu, J.P. Vivek, E.W. Zhao, J. Lei, N. Garcia-Araez, C.P. Grey, *Chem Rev*, 120 (2020).

30. L. Grande, E. Paillard, J. Hassoun, J.-B. Park, Y.-J. Lee, Y.-K. Sun, S. Passerini, B. Scrosati, L. Grande, E. Paillard, S. Passerini, J. Hassoun, J. Park, Y. Lee, Y. Sun, B. Scrosati, *Advanced Materials*, 27 (2015) 784–800.

31. A. Rinaldi, O. Wijaya, H.E. Hoster, D.Y.W. Yu, *ChemSusChem*, 7 (2014) 1283–1288.

32. D. Zhai, H.H. Wang, J. Yang, K.C. Lau, K. Li, K. Amine, L.A. Curtiss, *J Am Chem Soc*, 135 (2013) 15364–15372.

33. B.D. Adams, R. Black, C. Radtke, Z. Williams, B.L. Mehdi, N.D. Browning, L.F. Nazar, *ACS Nano*, 8 (2014) 12483–12493.

34. J.W. Jung, D.W. Choi, C.K. Lee, K.R. Yoon, S. Yu, J.Y. Cheong, C. Kim, S.H. Cho, J.S. Park, Y.J. Park, I.D. Kim, *Nano Energy*, 46 (2018) 193–202.

35. M.M. Ottakam Thotiyl, S.A. Freunberger, Z. Peng, P.G. Bruce, *J Am Chem Soc*, 135 (2013) 494–500.

36. C. Ling, R. Zhang, K. Takechi, F. Mizuno, *Journal of Physical Chemistry C*, 118 (2014) 26591–26598.

37. D.M. Itkis, D.A. Semenenko, E.Y. Kataev, A.I. Belova, V.S. Neudachina, A.P. Sirotina, M. Hävecker, D. Teschner, A. Knop-Gericke, P. Dudin, A. Barinov, E.A. Goodilin, Y. Shao-Horn, L. V. Yashina, *Nano Lett*, 13 (2013) 4697–4701.

38. W. Tang, B. Li, K. Teng, X. Wang, R. Liu, M. Wu, L. Zhang, P. Ren, J. Zhang, M. Feng, *Journal of Materiomics*, 8 (2022) 454–474.

39. S. Park, J. Kim, K. Kwon, *Chemical Engineering Journal*, 446 (2022) 137116.

40. H. Meng, S. Pei, H. Li, Y. Zhang, *ACS Omega*, 6 (2021) 11059–11067.

41. M.K. Singla, P. Nijhawan, A.S. Oberoi, *Environmental Science and Pollution Research*, 28 (2021) 15607–15626.

42. X. Ren, Y. Wang, A. Liu, Z. Zhang, Q. Lv, B. Liu, *J Mater Chem A Mater*, 8 (2020) 24284–24306.

43. L. Zhou, K. Higashimine, R. Badam, N. Matsumi, *Mater Res Express*, 10 (2023) 125508.

44. N. Wang, J. Fu, X. Cao, L. Tang, X. Meng, Z. Han, L. Sun, S. Qi, D. Xiong, *Electrochim Acta*, 428 (2022) 140894.

45. X. Hong, C. Tan, J. Chen, Z. Xu, H. Zhang, *Nano Res*, 8 (2015) 40–55.

46. K.W. Choi, D.Y. Kim, S.J. Ye, O.O. Park, *Advances in Materials Research*, 3 (2014) 199–216.

47. F. Yang, D. Deng, X. Pan, Q. Fu, X. Bao, *Natl Sci Rev*, 2 (2015) 183–201.

48. Y.C. Lu, Z. Xu, H.A. Gasteiger, S. Chen, K. Hamad-Schifferli, Y. Shao-Horn, *J Am Chem Soc*, 132 (2010) 12170–12171.

49. Y.C. Lu, H.A. Gasteiger, Y. Shao-Horn, *J Am Chem Soc*, 133 (2011) 19048–19051.

50. Z. Wen, C. Shen, Y. Lu, *Chempluschem*, 80 (2015) 270–287.

51. S. Jin, Y. Jiang, H. Ji, Y. Yu, S. Jin, Y. Jiang, H. Ji, Y. Yu, *Advanced Materials*, 30 (2018) 1802014.

52. W. Pan, X. Yang, J. Bao, M. Wang, *J Electrochem Soc*, 164 (2017) E3499–E3511.

53. M. Kim, E. Yoo, W.S. Ahn, S.E. Shim, *J Power Sources*, 389 (2018) 20–27.

54. A.A. Franco, K.-H. Xue, *ECS Journal of Solid State Science and Technology*, 2 (2013) M3084–M3100.

55. N. Ding, S.W. Chien, T.S.A. Hor, R. Lum, Y. Zong, Z. Liu, *J Mater Chem A Mater*, 2 (2014) 12433–12441.

56. J. Dai, T. Kogut, L. Jin, D. Reisner, *ECS Trans*, 6 (2008) 381–387.

57. C. Hee-Dae Lim, K.-Y. Park, H. Song, E. Yun Jang, H. Gwon, J. Kim, Y. Hyup Kim, M.D. Lima, R. Ovalle Robles, X. Lepró, R.H. Baughman, K. Kang, H. Lim, K. Park, H. Gwon, J. Kim, K. Kang, H. Song, E.Y. Jang, Y.H. Kim, M.D. Lima, R.O. Robles, X. Lepró, R.H. Baughman Alan G MacDiarmid, *Advanced Materials*, 25 (2013) 1348–1352.

58. W. Yu, T. Yoshii, A. Aziz, R. Tang, Z.Z. Pan, K. Inoue, M. Kotani, H. Tanaka, E. Scholtzová, D. Tunega, Y. Nishina, K. Nishioka, S. Nakanishi, Y. Zhou, O. Terasaki, H. Nishihara, *Advanced Science*, 10 (2023) 2300268.

59. Y. Jiang, L. Yang, T. Sun, J. Zhao, Z. Lyu, O. Zhuo, X. Wang, Q. Wu, J. Ma, Z. Hu, *ACS Catal*, 5 (2015) 6707–6712.

60. L. Yang, J. Shui, L. Du, Y. Shao, J. Liu, L. Dai, Z. Hu, L. Yang, Z. Hu, J. Shui, L. Du, Y. Shao, J. Liu, L. Dai, *Advanced Materials*, 31 (2019) 1804799.

61. M. He, P. Zhang, L. Liu, B. Liu, S. Xu, *Electrochim Acta*, 191 (2016) 90–97.

62. J.H. Kim, A.G. Kannan, H.S. Woo, D.G. Jin, W. Kim, K. Ryu, D.W. Kim, *J Mater Chem A Mater*, 3 (2015) 18456–18465.

63. J.H. Kang, J. Lee, J.W. Jung, J. Park, T. Jang, H.S. Kim, J.S. Nam, H. Lim, K.R. Yoon, W.H. Ryu, I.D. Kim, H.R. Byon, *ACS Nano*, 14 (2020) 14549–14578.

64. Y.J. Lee, S.H. Park, S.H. Kim, Y. Ko, K. Kang, Y.J. Lee, *ACS Catal*, 8 (2018) 2923–2934.

65. P. Żółtowski, D.M. Dražić, L. Vorkapić, *J Appl Electrochem*, 3 (1973) 271–283.

66. Y. Meng, W. Song, H. Huang, Z. Ren, S.Y. Chen, S.L. Suib, *J Am Chem Soc*, 136 (2014) 11452–11464.

67. O. Oloniyo, S. Kumar, K. Scott, *J Electron Mater*, 41 (2012) 921–927.

68. T. Zhang, F. Cheng, J. Du, Y. Hu, J. Chen, T. Zhang, F. Cheng, J. Du, Y. Hu, J. Chen, *Adv Energy Mater*, 5 (2015) 1400654.

69. Y. Zhao, C. Chang, F. Teng, Y. Zhao, G. Chen, R. Shi, G.I. N Waterhouse, W. Huang, T. Zhang, Y. Zhao, C. Chang, F. Teng, G. Chen, R. Shi, T. Zhang, G.I. N Waterhouse, W. Huang, *Adv Energy Mater*, 7 (2017) 1700005.

70. D.U. Lee, P. Xu, Z.P. Cano, A.G. Kashkooli, M.G. Park, Z. Chen, *J Mater Chem A Mater*, 4 (2016) 7107–7134.

71. X. He, F. Yin, G. Li, *Int J Hydrogen Energy*, 40 (2015) 9713–9722.

72. Z. Lu, H. Wang, D. Kong, K. Yan, P.C. Hsu, G. Zheng, H. Yao, Z. Liang, X. Sun, Y. Cui, *Nature Communications 2014 5:1*, 5 (2014) 1–7.

73. X. Han, G. He, Y. He, J. Zhang, X. Zheng, L. Li, C. Zhong, W. Hu, Y. Deng, T.-Y. Ma, *Adv Energy Mater*, 8 (2018) 1870043.

74. J. Xu, P. Gao, T.S. Zhao, *Energy Environ Sci*, 5 (2012) 5333–5339.

75. Y. Yan, B.Y. Xia, B. Zhao, X. Wang, *J Mater Chem A Mater*, 4 (2016) 17587–17603.

76. F. Cheng, J. Shen, B. Peng, Y. Pan, Z. Tao, J. Chen, *Nature Chemistry 2010 3:1*, 3 (2010) 79–84.

77. J. Pan, X.L. Tian, S. Zaman, Z. Dong, H. Liu, H.S. Park, B.Y. Xia, *Batter Supercaps*, 2 (2019) 336–347.

78. X. Guo, J. Zhang, Y. Zhao, B. Sun, H. Liu, G. Wang, *ACS Appl Energy Mater*, 2 (2019) 4215–4223.

79. Y. Wu, H. Ding, T. Yang, Y. Xia, H. Zheng, Q. Wei, J. Han, D.L. Peng, G. Yue, *Advanced Science*, 9 (2022) 2200523.

80. H. Wu, W. Sun, J. Shen, Z. Mao, H. Wang, H. Cai, Z. Wang, K. Sun, *ACS Sustain Chem Eng*, 6 (2018) 15180–15190.

81. H. Wu, W. Sun, J. Shen, C. Lu, Y. Wang, Z. Wang, K. Sun, *Nanoscale*, 10 (2018) 13149–13158.

82. X. Cao, Z. Sun, X. Zheng, C. Jin, J. Tian, X. Li, R. Yang, *ChemSusChem*, 11 (2018) 574–579.

83. H.M. Zhang, Y. Shimizu, Y. Teraoka, N. Miura, N. Yamazoe, *J Catal*, 121 (1990) 432–440.

84. H. Tanaka, M. Misono, *Curr Opin Solid State Mater Sci*, 5 (2001) 381–387.

85. L. Swette, N. Kackley, S.A. McCatty, *J Power Sources*, 36 (1991) 323–339.

86. A.M. Kannan, A.K. Shukla, S. Sathyanarayana, *J Power Sources*, 25 (1989) 141–150.

87. X. Han, Y. Hu, J. Yang, F. Cheng, J. Chen, *Chemical Communications*, 50 (2014) 1497–1499.

88. J.J. Xu, Z.L. Wang, D. Xu, F.Z. Meng, X.B. Zhang, *Energy Environ Sci*, 7 (2014) 2213–2219.

89. J. Zhang, Y. Zhao, X. Zhao, Z. Liu, W. Chen, *Sci Rep*, 4 (2014).

90. G.S. Hegde, A. Ghosh, R. Badam, N. Matsumi, R. Sundara, *ACS Appl Energy Mater*, 3 (2020).

91. A.S. Ryabova, A. Bonnefont, P.A. Simonov, T. Dintzer, C. Ulhaq-Bouillet, Y.G. Bogdanova, G.A. Tsirlina, E.R. Savinova, *Electrochim Acta*, 246 (2017) 643–653.

92. S.J. Tauster, S.C. Fung, R.L. Garten, *J Am Chem Soc*, 100 (1978) 170–175.

93. S. Bernal, F.J. Botana, J.J. Calvino, C. López, J.A. Pérez-Omil, J.M. Rodríguez-Izquierdo, *Journal of the Chemical Society, Faraday Transactions*, 92 (1996) 2799–2809.

94. R.A. Demmin, C.S. Ko, R.J. Gorte, *Journal of Physical Chemistry*, 89 (1985) 1151–1154.

95. C.S. Ko, R.J. Gorte, *J Catal*, 90 (1984) 59–64.

96. D.N. Belton, Y.M. Sun, J.M. White, *Journal of Physical Chemistry*, 88 (1984) 1690–1695.

97. S. Sakellson, M. McMillan, G.L. Haller, *Journal of Physical Chemistry*, 90 (1986) 1733–1736.

98. J.M. Coronado, Y. Yang, X. Zhang, Y. Liu, X. Ma, X. Liu, R. Zhang, Y. Wang, *Nanoenergy Advances 2023, Vol. 3, Pages 48-72*, 3 (2023) 48–72.

99. Z. Luo, G. Zhao, H. Pan, W. Sun, Z. Luo, G. Zhao, H. Pan, W. Sun, *Adv Energy Mater*, 12 (2022) 2201395.

100. R. Badam, R. Vedarajan, K. Okaya, K. Matsutani, N. Matsumi, *Scientific Reports 2016 6:1*, 6 (2016) 1–7.

101. S. Mao, C. Wang, Y. Wang, *J Catal*, 375 (2019) 456–465.

102. J. Melke, B. Peter, A. Habereder, J. Ziegler, C. Fasel, A. Nefedov, H. Sezen, C. Wöll, H. Ehrenberg, C. Roth, *ACS Appl Mater Interfaces*, 8 (2016) 82–90.

103. H. Wang, Y. Shao, S. Mei, Y. Lu, M. Zhang, J.K. Sun, K. Matyjaszewski, M. Antonietti, J. Yuan, *Chem Rev*, 120 (2020) 9363–9419.

104. R.M. Cywar, N.A. Rorrer, C.B. Hoyt, G.T. Beckham, E.Y.X. Chen, *Nature Reviews Materials 2021 7:2*, 7 (2021) 83–103.

105. C.; Yang, H.; Wu, M.; Cai, Y.; Zhou, C.; Guo, Y.; Han, L. Zhang, C. Yang, H. Wu, M. Cai, Y. Zhou, C. Guo, Y. Han, L. Zhang, *Polymers 2023, Vol. 15, Page 2741*, 15 (2023) 2741.

106. J.A. Asensio, P. Gómez-Romero, *Fuel Cells*, 5 (2005) 336–343.

107. S.C. Kumbharkar, U.K. Kharul, *J Memb Sci*, 360 (2010) 418–425.

108. A. Nag, M.A. Ali, H. Kawaguchi, S. Saito, Y. Kawasaki, S. Miyazaki, H. Kawamoto, D.T.N. Adi, K. Yoshihara, S. Masuo, Y. Katsuyama, A. Kondo, C. Ogino, N. Takaya, T. Kaneko, Y. Ohnishi, *Adv Sustain Syst*, 5 (2021) 2000193.

109. C. Du, Q. Tan, G. Yin, J. Zhang, *Rotating Electrode Methods and Oxygen Reduction Electrocatalysts* (2014) 171–198.

110. R.J. Forster, D. Walsh, K. Adamson, E. Spain, *Encyclopedia of Analytical Science* (2019) 209–217.

111. J. Zhang, J. Wu, H. Zhang, J. Zhang, *PEM Fuel Cell Testing and Diagnosis* (2013) 1–375.

112. G. Bontempelli, N. Dossi, R. Toniolo, *Reference Module in Chemistry, Molecular Sciences and Chemical Engineering* (2016).

113. R.K. Singh, R. Devivaraprasad, T. Kar, A. Chakraborty, M. Neergat, *J Electrochem Soc*, 162 (2015) F489–F498.

114. H.S. Magar, R.Y.A. Hassan, A. Mulchandani, *Sensors 2021, Vol. 21, Page 6578*, 21 (2021) 6578.

115. Z. Lin, D. Li, Y. Zou, *J Energy Storage*, 74 (2023) 109386.

116. T. Placke, R. Kloepsch, S. Dühnen, M. Winter, *Journal of Solid State Electrochemistry*, 21 (2017) 1939–1964.

Chapter 2 $CoFe_2O_4$ Nanoparticles on Bio-based Polymer Derived Nitrogen Doped Carbon as Bifunctional ORR/OER Electrocatalyst in Nonaqueous Electrolyte.

Abstract

The oxygen reduction reaction (ORR) and oxygen evolution reaction (OER) play a crucial role in various energy storage devices. Metal oxides nanoparticles on carbon support have been investigated for ORR and OER applications. ORR and OER electrochemical activity depend on physicochemical properties of both metal oxides nanoparticles and carbon support. Nitrogen functional groups naturally present on the carbon surface act as adsorption sites for ORR intermediates and nucleation sites for nanoparticles. Some of these nitrogen functionalities lead to an increase in the dispersion and stabilization of metal oxides nanoparticles, which positively impacts the ORR and OER performance in aqueous electrolyte. Researchers are particularly interested in studying the effect of nitrogen groups on aprotic ORR due to the growing development of aprotic metal-air batteries. Similarly, in Li+ containing electrolytes, these nitrogen groups enhance both the ORR and OER performance. Herein, we synthesized spinel $CoFe_2O_4$-decorated on bio-based nitrogen doped carbon derived from poly(2,5-benzimidazole) (ABPBI) electrocatalysts. The carbon support (PY-PBI800) possesses highly doped nitrogen up to 17% wt. Notably, strong metal-substrate interaction (SMSI) influence by the nitrogen functionalities was observed through X-ray photoelectron spectroscopy.

2.1 Introduction

In the relentless pursuit of sustainable energy solutions, the global scientific community has long recognized the pressing need for advanced energy storage systems. Among the array of potential energy storages, lithium-air batteries (LABs) have emerged as a promising prospect due to their unparalleled theoretical energy density of 3,505 $Whkg^{-1}$ [1], which surpasses that of the prevalent typical lithium-ion batteries (500 – 800 $Whkg^{-1}$)[2]. This remarkable potential stems from LABs utilizing atmospheric oxygen as a reactant. However, despite the promising theoretical advantages, the practical realization of LABs remains fraught with multifaceted challenges. Issues such as poor cycling stability, limited lifespan, and unresolved side reactions have hindered their commercial viability and widespread adoption [3]. Consequently, the

imperative for rigorous research and development efforts aimed at overcoming these obstacles cannot be overstated. The major challenges of LABs are mostly dependent on air cathode which consists of porous material to store Li_2O_2 and electrocatalysts to facilitate oxygen reduction reaction (ORR) and oxygen evolution reaction (OER). The sluggish kinetics from these reactions are a major issue that hindered their performance compared to their theoretical performance. Hence, developing electrocatalysts to promote ORR/OER is essential to reach the theoretical performance of LABs.

In recent times, researchers have investigated noble metal-free oxides as potential electrocatalysts. There are several types of metal oxides catalysts including single metal oxide, spinel metal oxides, and perovskite[4]. Single metal oxides are efficient electrocatalyst in either ORR or OER, however they do not possess efficient bifunctional electrocatalytic activity[5,6]. Hence, combining metal oxides to promote bifunctional electrocatalytic activity has been investigated. In the case of perovskite, efficient bifunctional electrocatalysts mostly contain rare earth metal such as La or Sr [7–9]. Therefore, among these oxides, spinel oxides have garnered attention. The structure of spinel oxides (denoted as AB_2O_4, where A and B represent transition metal ions) comprises B^{3+} ions at the octahedral sites and A^{2+} ions at the tetrahedral sites. These metal ions serve as active sites, enhancing the reactivity of ORR and OER [10,11]. Despite their potential, spinel-oxide electrocatalysts suffer from inadequate cyclability and limited electrocatalytic performance. To tackle these challenges, employing carbon-based electrocatalyst as the support materials which possess high surface area and good conductivity is crucial. These conductive support materials, characterized by their large surface area, enhance the availability of active sites for oxygen adsorption. Additionally, they facilitate rapid ion and charge transportation by providing elevated electrode – electrolyte interface. As a result, this enhancement in electrocatalytic activity contributes to improved ORR and OER[12,13]. Notwithstanding their inherent potential, carbonaceous electrocatalysts still exhibit lower electrocatalytic performance compared to commercial Pt/C electrocatalysts. Researchers have widely employed the doping of heteroatoms into carbonaceous materials as an effective strategy to enhance electrocatalytic performance[14–16]. These heteroatoms, including nitrogen, boron, phosphorus, and sulfur, induce changes in spin and charge density between atoms [17]. Consequently, these density alterations facilitate oxygen absorption and desorption within the carbonaceous materials, leading to improved oxygen electrocatalytic reactions.

Among heteroatom-doped carbon, nitrogen-doped carbon is widely studied for electrocatalytic application [18–20]. Nitrogen-doped carbon materials exhibit fascinating

properties due to the introduction of nitrogen atoms. Despite having a similar size to carbon atoms, nitrogen possesses higher electronegativity [21]. Consequently, when nitrogen is incorporated into the carbon structure, it induces defects that disrupt the electroneutrality of carbon atoms[22]. This modification enhances both electronic and ionic conductivity without distorting the local geometry[23]. In the case of applying nitrogen-doped carbon as a support for metal electrocatalyst, these defects also serve as anchoring sites for uniformly active metals, leading to enhanced stability according to the strong interaction between metal nanoparticles and the nitrogen-doped carbon support [24]. The strong metal–substrate interaction (SMSI) between the nitrogen-doped carbon support and the active metallic species can be modulated by electronic interactions originating from incorporating heteroatoms into the carbon materials[25]. Research has demonstrated that metal nanoparticles supported on nitrogen-doped carbon materials possess higher stability according to the stronger binding to the support in regions with high nitrogen doping[26]. Even when metal is directly deposited on nitrogen-doped carbon followed by carbonization at high temperatures, it leads to highly dispersed metal nanoparticles [27]. A study involving Pt nanoparticles on nitrogen-doped highly ordered pyrolytic graphite (HOPG) revealed that Pt preferentially nucleates on pyrrole and pyridinic defect sites, according to the partial charges on adjacent carbon atoms induced by nitrogen[28]. Thus, For ORR and OER, the nitrogen functionalities on carbon support and the corresponding SMSI with the metal nanoparticles are crucial to achieving highly efficient and stable electrocatalysts.

To obtain preferable nitrogen functionalities in the carbon support structure both carbon and nitrogen precursors should be intensively selected. Polymers, as precursors, hold significant potential due to their adaptable molecular and nanoscale structures, tuneable chemical composition, and diverse processing methods. These attributes, combined with solid-state chemistry, allow the resulting carbon materials to maintain their desired textures during carbonization[29]. However, these polymers typically produced from fossil-based carbon, involve olefin and aromatics building blocks which lead to climate change. Hence, to produce more sustainable polymers, researchers have extensively explored converting bio-feedstocks into compounds that closely resemble those derived from petroleum [30,31]. Poly(2,5-benzimidazole) (ABPBI) is a highly promising polymer for carbon precursors. Its simple preparation process involves a single monomer [32], making it an attractive choice. The repeating unit of ABPBI contains only one benzimidazole moiety, resulting in a higher N-H group density[33]. Bio-derived ABPBI was prepared from 3,4-diaminobenzoic acid (DABA) monomers which were converted from 3-amino-4-hydroxybenzoic acid (AHBA). AHBA is

synthesized from kraft pulp, an inedible cellulosic material, using genetically modified bacteria[34]. After pyrolysis of ABPBI, it leads to significant nitrogen doping in the carbon structure. According to these properties, ABPBI serves as a single precursor for both carbon and nitrogen, enabling the preparation of heavily N-doped carbon material (PYPBI800). This material boasts an impressive char yield of up to 95% and heavily nitrogen doping on carbon (~17 wt%)[35].

Herein, we introduced spinel cobalt iron oxide ($CoFe_2O_4$) nanoparticles decorated on pyrolyzed poly(2,5-benzimidazole) (PYPBI800) as the bifunctional electrocatalyst in Li^+ non aqueous electrolyte. The electrocatalyst was synthesized through pyrolysis of PBI followed by incipient wetness impregnation calcination on the metal precursors. The SMSI between $CoFe_2O_4$ and PYPBI800 has been confirmed with X-ray photoelectron spectroscopy. Due to both the intrinsic properties of $CoFe_2O_4$ and the nitrogen doping effect, these electrocatalysts also modulate the electronic state of metals, facilitating oxygen adsorption and desorption at the electrode. When employed as an electrocatalyst in three electrode system, the electrocatalyst exhibited promising onset potential of -0.85 V vs Ag/Ag^+ for ORR, and 1.0 V vs Ag/Ag^+ for OER which are comparable to noble metal electrocatalyst[36]. To the best of our knowledge, this will be the first study to employ bio-derived PYPBI800 as a support for $CoFe_2O_4$ as ORR/OER bifunctional electrocatalysts in nonaqueous electrolyte.

2.2 Experimental

2.2.1 Synthesis of Pyrolyzed Poly(2,5-benzimidazole)

Pyrolyzed poly(2,5-benzimidazole) (PYPBI) was prepared according to the literature [35]. First, ABPBI precursor was synthesised by polycondensation of bio-derived 3,4-diaminobenzoic acid (DABA). In brief, 30 g of polyphosphoric acid (PPA) as a condensation agent was heated to 120 ºC under N_2 atmosphere for 30 minutes to remove water. Then, HCl•DABA as monomers were added into the PPA and stirred until a homogenous mixture was obtained. The temperature was then elevated to 160 ºC, and then the mixture was continuously stirred for 2 hours. After that, the temperature was further elevated to 200 ºC and the mixture was stirred overnight. The obtained ABPBI was rinsed with deionized water and oven-dried overnight and ground into powder. The powdered PBI was dispersed in 10% KOH to remove the remaining PPA. Finally, the ABPBI powder is filtered and dried in a vacuum oven overnight. The ABPBI was carbonized under N_2 atmosphere in a tube furnace. The temperature was raised from room temperature to 200 ºC at the rate of 5 ºC min^{-1} and held for 30 minutes to remove moisture. Then it was elevated to 800 ºC at 5 ºC min^{-1} and kept for 145

minutes. The obtained product was activated in 1M HCl. Then, it was washed and dried in a vacuum oven overnight. The final product yield was 25% compared to the initial monomer. It is labelled as PYPBI800.

2.2.2 Decoration of $CoFe_2O_4$ on PYPBI800

In this work, PYPBI800-supported $CoFe_2O_4$, Co, and Fe samples were prepared. Co-incipient wetness impregnation method with the mixture of ethylene glycol and DI water (3:1) was used. Cobalt(II) nitrate hexahydrate and iron(III) nitrate nonahydrate was used as precursors. Firstly, the metal precursors were dissolved in a mixture of ethylene glycol and DI water separately. Then, both nitrate solutions were incorporated into PYPBI800 to obtain total metals loading of 20%. Next, the impregnated samples were dried in the vacuum oven overnight. After drying, the samples were calcinated under N_2 atmosphere in a tube furnace. The temperature was raised from room temperature to 200 ºC at the rate of 5 ºC min^{-1} and held for 30 minutes to remove moisture. Then it was elevated to 550 ºC at 5 ºC min^{-1} and kept for 4 hours. The samples were denoted as 20% $CoFe_2O_4$ PBI, Co PBI, and Fe PBI. Besides, 10% $CoFe_2O_4$ and 30% $CoFe_2O_4$ were also prepared to study the effects of metal loading.

2.2.3 Characterization of Electrocatalyst

The morphologies and elemental composition of each sample were studied by scanning electron microscopy equipped with energy dispersive X-ray spectrometers (SEM-EDS) using Tabletop Microscope TM3030 plus (Hitachi High-Technologies Co. Ltd) and the TM Series Energy Dispersive X-ray Spectrometers: AZtec Series from Oxford Instruments (UK) Co. Ltd. High-resolution transmission electron microscope (HR-TEM) along with JEM-ARM200F instrument (JEOL Ltd) was used to determine nanoparticles size, crystal plane, and composite formation of the samples. The chemical composition and oxidation state of each sample were determined by X-ray photoelectron spectroscopy (XPS) with S-ProbeTM2803 (Fisions Instrument Ltd.) The X-ray diffraction (XRD) patterns of each sample were analysed using Smart Lab X-Ray Diffractometer (Rigaku Corporation) with Cu Kα radiation (λ = 0.15418 nm, over the 2θ range of 10° – 80° with a step size of 0.02°)

2.2.4 Electrochemical Characterization

Electrochemical performance of the electrocatalysts was performed in rotating disk electrode RRDE-3A (ALS Japan) with three electrodes configuration in 0.1 M LiTFSI in tetra-ethylene glycol dimethyl ether (TEGDME) nonaqueous electrolyte with VSP potentiostat (Bio-logic Science Instruments). The working electrode was a 3 mm glassy carbon electrode

which was polished with alumina paste to get a smooth surface. Then, the electrocatalyst ink was prepared by dissolving 3 mg of active material and 3 mg of acetylene black in 1200 µL solution of 6:4 isopropyl alcohol and deionized water. Then, Nafion™ perfluorinated resin solution 5 wt% was added as a binder for 12 µL. 2.5 µL of electrocatalyst ink was dropped on the glassy carbon electrode which make the active material loading of 88.5 µg cm^{-2}. A platinum coil was used as the counter electrode. $Ag/Ag(NO_3)$ which consisted of a silver wire and 0.01 M $AgNO_3$, 0.1 M tetrabutylammonium perchlorate in acetonitrile electrolyte was used as the reference electrode for nonaqueous electrolyte. Electrochemical impedance spectroscopy (EIS) was performed to gather the impedance information of the electrocatalyst. Cyclic voltammetry (CV) plots were recorded by sweeping the potential between 1.8 to -2.5 V vs Ag/Ag^{+} at a scan rate of 50 mVs^{-1} under 1600 rpm.

2.3 Results and Discussion

2.3.1 Characterisation of Electrocatalysts

In the study of carbon-supported catalysts, various metal loadings were examined, revealing a similar carbon support structure across all loadings. As shown in Figure 2.1, Co PBI exhibited finely dispersed nanoparticles, while Fe PBI showcased larger nanoparticles but with superior distribution. Interestingly, the combination of Co and Fe yielded nanoparticles that demonstrated a fusion of these characteristics. Furthermore, it was observed that higher concentrations of $CoFe_2O_4$ resulted in an expanded coverage area. In Figure 2.2, the elemental mapping for PYPBI800 indicates that nitrogen is well distributed in the carbon structure. On the other hand, 20%$CoFe_2O_4$ PBI elemental mapping is illustrated in Figure 2.3 which confirmed the well dispersion of the $CoFe_2O_4$ nanoparticles on PYPBI800. Similarly, the other sample also shown well distributed of the metal oxides nanoparticles as shown in Figure 2.4 for Co PBI, Figure 2.5 for Fe PBI, Figure 2.6 for 10%$CoFe_2O_4$ PBI, and Figure 2.7 for 30%$CoFe_2O_4$ PBI. The elemental content determined from SEM-EDS is illustrated in Table 2.1. It can be observed that nitrogen content was significantly dropped compared to the metal-free PBI. Additionally, oxygen content was increased after the introduction of metal nanoparticles. These indicate the formation of metal oxides in the electrocatalysts. However, in the case of Co PBI, the oxygen content was much lower which could be referred to as metallic Co nanoparticles were formed.

To confirm the formation of spinel $CoFe_2O_4$ on PBI, powder XRD were recorded as shown in Figure 2.8. The broad peak observed in the range of 10° to 30° corresponds to the presence of carbon in the PYPBI800 support[37]. Comparing the XRD patterns of

20%$CoFe_2O_4$ PBI and PYPBI800, it is evident that 20%$CoFe_2O_4$ PBI retains the basic characteristic peaks of PYPBI800, indicating that PYPBI800 remains relatively unaffected during the calcination of 20%$CoFe_2O_4$ PBI. In the XRD spectrum of 20%$CoFe_2O_4$ PBI, typical diffraction peaks are located at specific angles: 30.17°, 35.55°, 38.14°, 43.21°, 54.42°, 57.08°, and 62.67°. These peaks can be indexed to the diffraction of $CoFe_2O_4$, corresponding to crystal planes (220), (311), (222), (400), (422), (511), and (440) (according to the PDF#22-1086 database) [38]. In the case of Fe PBI, similar peaks were observed corresponding to the spinel structure of Fe_3O_4 according to PDF# 96–900-7645 database. Besides, apart from PBI, Co PBI exhibits a single peak at 44.4° peaks corresponding to crystal planes (111) of metallic, according to PDF#15-0806 database. The Scherrer formula, expressed as Equation 1, was employed to determine the average crystallite size of $CoFe_2O_4$ based on the intensity of the corresponding Bragg peaks.

$$Crystallite \quad size(\text{Å}) = \frac{k\lambda}{\beta cos\theta} \qquad (1)$$

where k is a dimensionless shape factor having a value of 0.9, λ is the wavelength of X-rays used (1.5418 Å), β is full width at half maximum (FWHM) of the Bragg peak in radians, and θ is the diffraction angle. The crystallite size of $CoFe_2O_4$ in 20%$CoFe_2O_4$ PBI was found to be in the range of 15 - 20 nm.

Figure 2.9a displays a high-resolution transmission electron microscope (HR-TEM) image of 20%$CoFe_2O_4$ PBI. The image reveals well-decorated, random-shaped $CoFe_2O_4$ grains on the PBI support with a size of 10 – 20 nm which is in accord with XRD results. Additionally, the image also shows a high coverage area of $CoFe_2O_4$ nanoparticles compared to decorating on Vulcan XC-72[39] and carbon black[40]. This emphasized the SMSI effect by the nitrogen defects in the carbon structure. Nitrogen defects act as an anchoring site for $CoFe_2O_4$[27,28].

Figure 2.9b shows lattice fringes of 20%$CoFe_2O_4$ PBI, where the d-spacing value of 0.253 nm, 0.210 nm, 0.170 nm, and 0.150 nm corresponds to the (311), (400), (422), and (420) plane of $CoFe_2O_4$, respectively. The observed clear lattice fringes align with the results obtained from the XRD pattern, confirming the presence of cubic spinel $CoFe_2O_4$. Moreover, the SAED pattern for the 20%$CoFe_2O_4$ PBI is depicted in Figure 2.9c. The clear diffraction rings and spots observed at 0.29, 0.25, 0.20, 0.16, and 0.14 nm are associated with the (220), (311), (400), (511), and (440) planes of $CoFe_2O_4$, respectively. Thus, these values from HR-TEM showed good agreement with the values determined from Bragg's Law as shown in Equation 2 where n is diffraction order (n=1) and d is the d-spacing.

$$n\lambda = 2d \sin\theta \qquad (2)$$

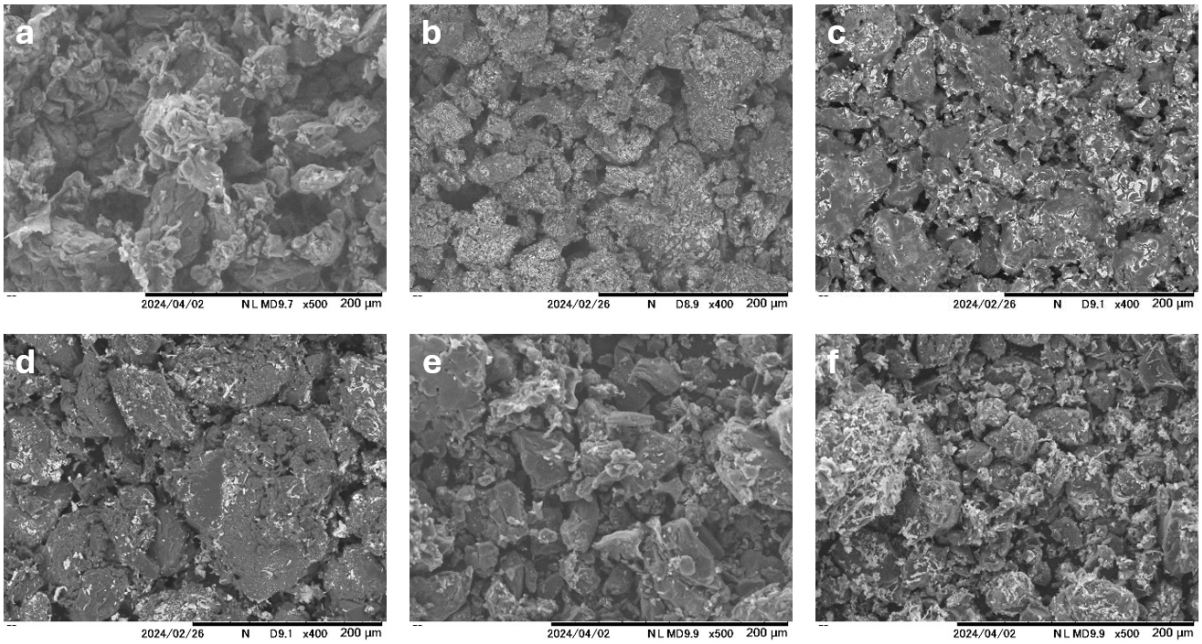

Figure 2.1 SEM images of a) PBI800, b) Fe PBI, c) Co PBI, d)20%$CoFe_2O_4$ PBI, e) 10%$CoFe_2O_4$ PBI, and f) 30%$CoFe_2O_4$ PBI

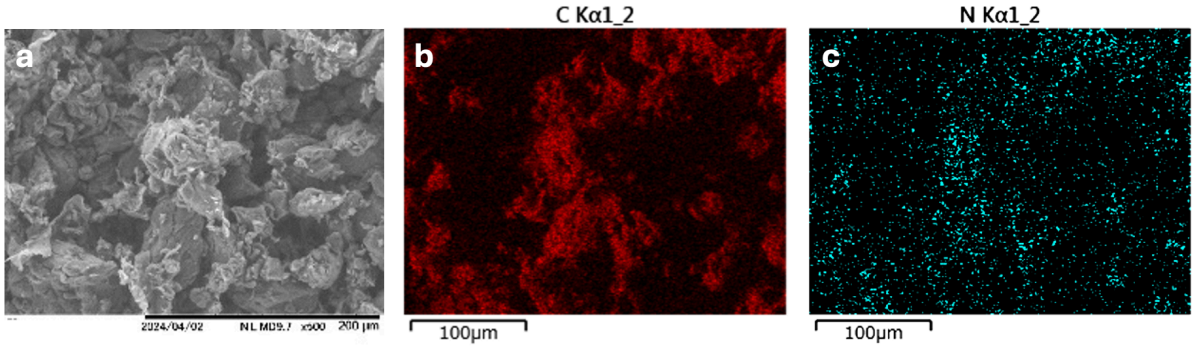

Figure 2.2 SEM-EDS Mapping images of PYPBI800 a) Depicted area for EDS elemental mapping. b) Carbon c) Nitrogen

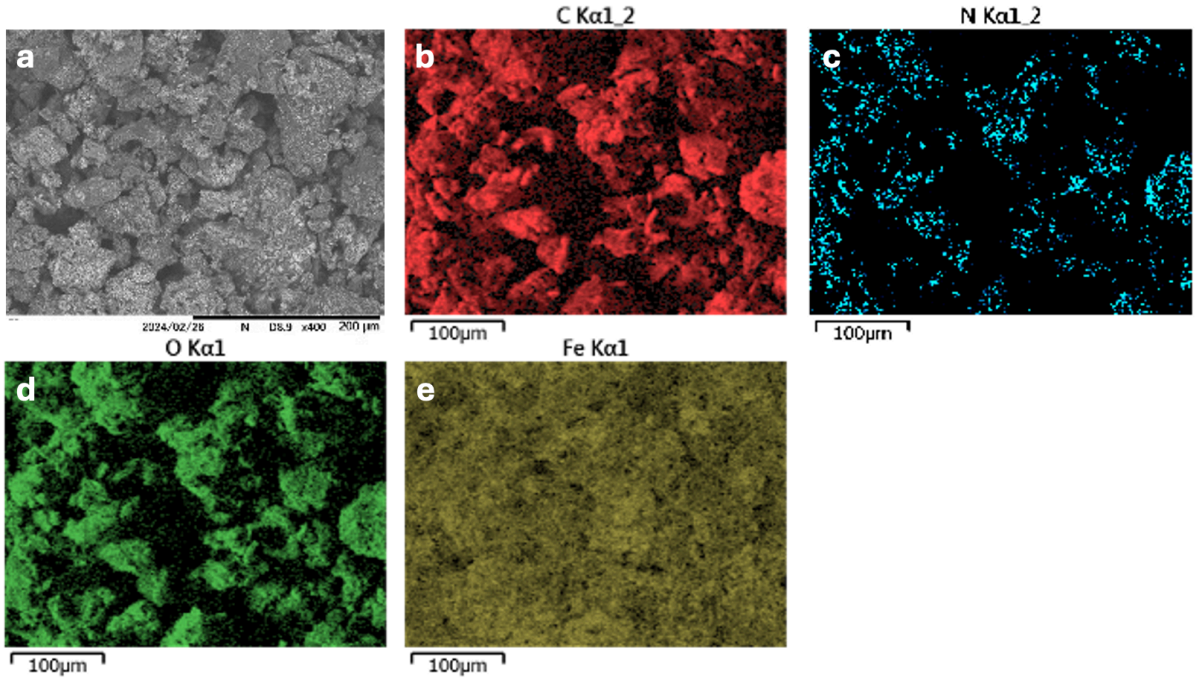

Figure 2.3 SEM-EDS Mapping images of Fe PBI a) Depicted area for EDS elemental mapping. b) Carbon c) Nitrogen d) Oxygen e) Iron

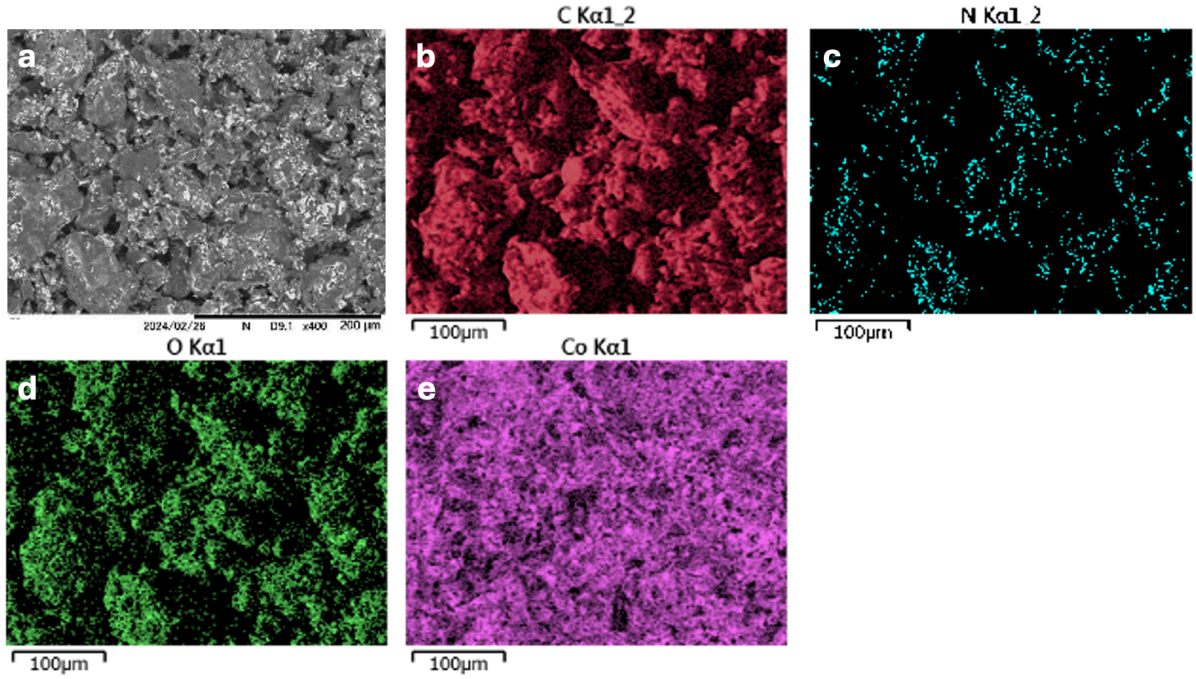

Figure 2.4 SEM-EDS Mapping images of Co PBI a) Depicted area for EDS elemental mapping. b) Carbon c) Nitrogen d) Oxygen e) Cobalt

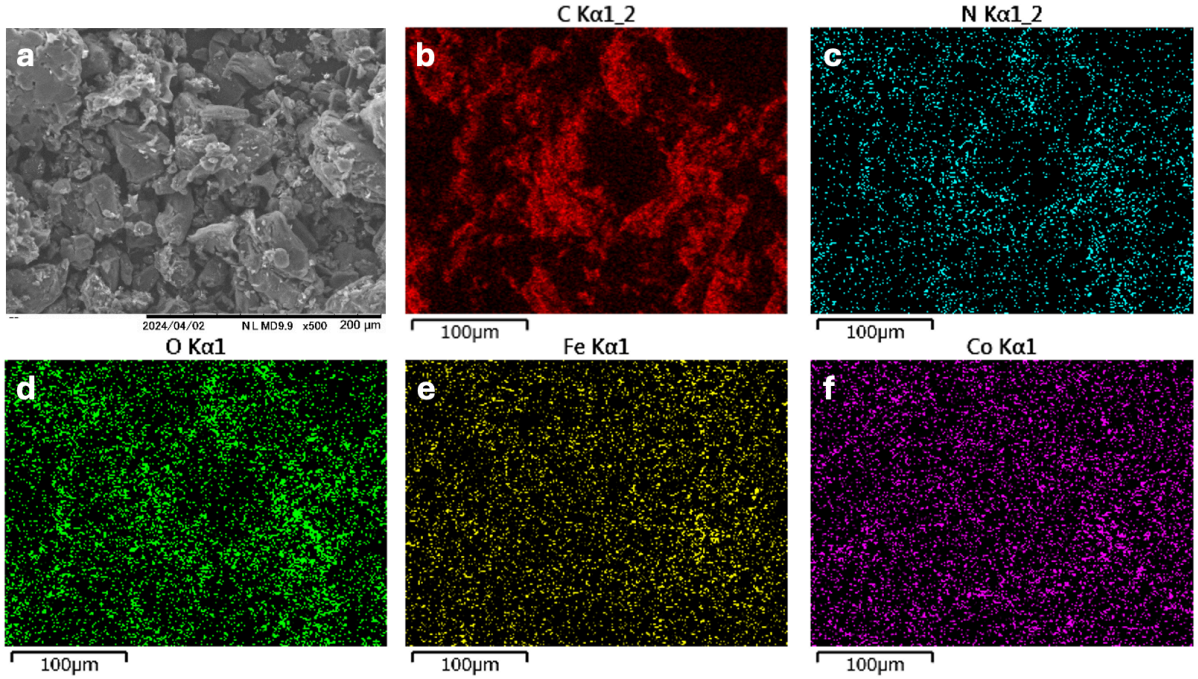

Figure 2.5 SEM-EDS Mapping images of 10%$CoFe_2O_4$ PBI a) Depicted area for EDS elemental mapping. b) Carbon c) Nitrogen d) Oxygen e) Iron f) Cobalt

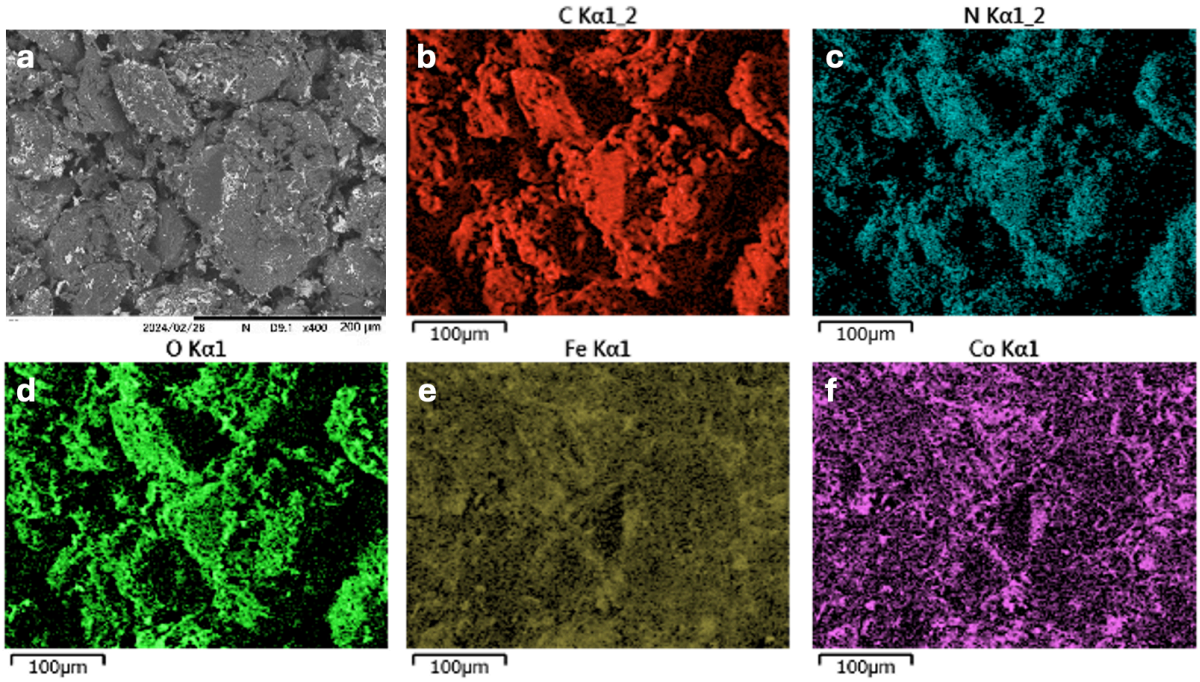

Figure 2.6 SEM-EDS Mapping images of 20%$CoFe_2O_4$ PBI a) Depicted area for EDS elemental mapping. b) Carbon c) Nitrogen d) Oxygen e) Iron f) Cobalt

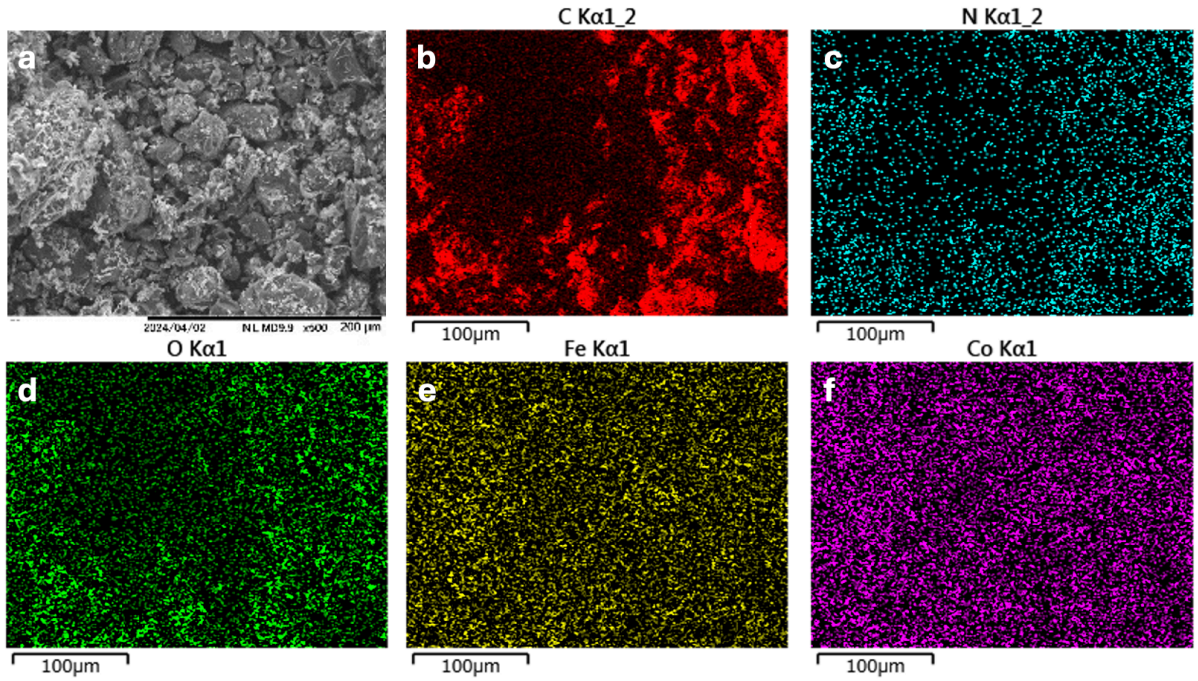

Figure 2.7 SEM-EDS Mapping images of 30%$CoFe_2O_4$ PBI a) Depicted area for EDS elemental mapping. b) Carbon c) Nitrogen d) Oxygen e) Iron f) Cobalt

Table 2.1 Composition of synthesized electrocatalysts acquired from SEM-EDS.

Elemental Content (%wt.)						
Sample	C	N	O	Co	Fe	Metal Loading
PYPBI800	70.47	23.54	5.99	-	-	-
Fe PBI	62.21	4.74	13.00	-	20.05	20.05%
Co PBI	69.37	7.41	3.34	19.88	-	19.88%
20%$CoFe_2O_4$ PBI	58.25	7.94	12.80	10.36	10.65	21.01%
10%$CoFe_2O_4$ PBI	64.27	13.32	11.24	5.70	5.47	11.17%
30%$CoFe_2O_4$ PBI	54.38	7.47	12.46	13.27	12.42	25.69%

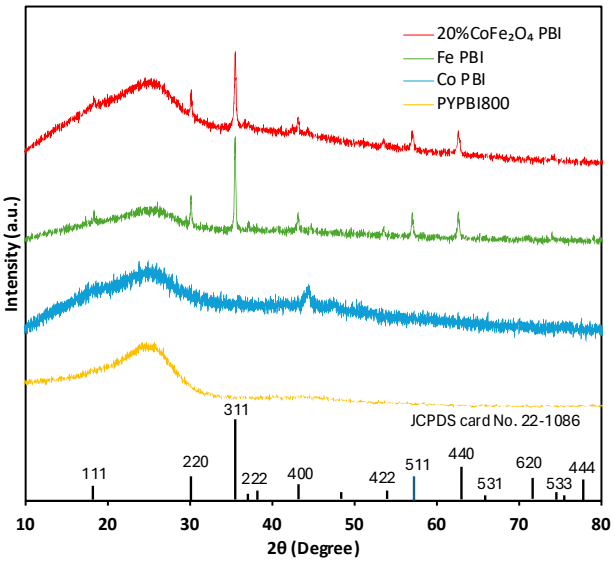

Figure 2.8 XRD patterns corresponded to Fe PBI, Co PBI, 20%$CoFe_2O_4$ PBI, and PBI800

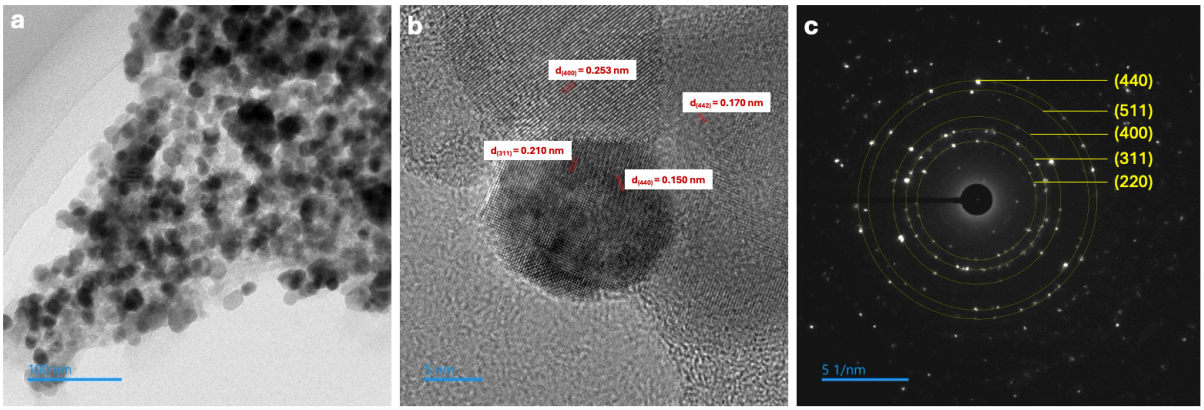

Figure 2.9 a) HR-TEM image, b) lattices fringes, and c) SAED pattern of 20%$CoFe_2O_4$ PBI

XPS measurements were conducted to determine the cation state and surface chemical composition of PYPBI800, 20% $CoFe_2O_4$ Graphite, Co PBI, and Fe PBI 10% $CoFe_2O_4$ PBI, and 20% $CoFe_2O_4$ PBI. The survey spectrum for PYPBI800 reveal peaks corresponding to C1s, N1s and O1s as shown in Figure 2.10a. In the case of 20% $CoFe_2O_4$ Graphite, the C1s, O1s, Fe2p, and Co2p peaks are observed (Figure 2.10b). For Co PBI, the survey spectra reveal C1s, O1s, N1s, and Co2p peaks (Figure 2.10c), while Fe PBI reveals C1s, O1s, N1s, and Fe2p peaks as illustrated in Figure 2.10d. Besides, 10% $CoFe_2O_4$ PBI and 20% $CoFe_2O_4$ PBI reveal similar peaks corresponding to C1s, N1s, O1s, Fe2p, and Co2p as shown in Figure 2.10e and Figure 2.10f, respectively.

The C1s deconvolution of all samples are illustrated on Figure 2.11a and Table 2.2. In can be seen that the peaks were shifted according to the developed C-N peak in PYPBI800 supports. These could be owing to the charge transfer from the nanoparticles to the carbon

structure[41]. Moreover, the peak at 290.7 eV in 20% $CoFe_2O_4$ Graphite indicate the π-π* bond[42,43] which was not observable in PYPBI800 supports. This is the evidence that the π-π* bond is perturbated by the nitrogen defects.

The N1s deconvolution of 20%$CoFe_2O_4$ PBI exhibits peaks at 397.6, 399.0, 400.5, and 404.0 eV, assignable to pyridinic-N, metal-N, graphitic-N, and oxidized-N, respectively[44] as shown in Figure 2.11b and Table 2.3, while PYPBI800 N1s peak is deconvoluted into pyridinic-N, graphitic-N, and oxidized-N at the binding energy of 397.9, 400.5, and 404.0 eV. According to the results can be seen that the peak at 399.0 eV in 20%$CoFe_2O_4$ PBI which corresponds to metal-N has appeared compared to PYPBI800. This metal-N illustrate that the metal oxide nanoparticles are anchored on the carbon support at N-defect sites, indicating SMSI between PYPBI800 support and $CoFe_2O_4$ nanoparticles[45].

The O1s spectra reveal peaks at 529.0 and 530.3 eV (associated with absorbed water and metal-O[12] in the carbon structure[46]) as shown in Figure 2.12 and Table 2.4. The metal-O is corresponded to the O in the metal oxide structure. Regularly, PYPBI800 does not contain oxygen in the carbon structure, hence O1s spectra for PYPBI800 show only absorbed water at 532.3 eV. Moreover, decoration of metal oxide nanoparticles led to a significant shift that correspond to oxygen in the spinel oxide structure Besides, the metal-O peak is not observed in Co PBI. This indicates that the nanoparticles in this sample are in metallic form instead of metal oxide in accord with XRD and SEM-EDS results.

Regarding the Co2p deconvolution of 20%$CoFe_2O_4$ PBI, five peaks are observed. The fitting results indicate that the peaks at 772.7 eV indicate Co-N[47] in $CoFe_2O_4$ decorated samples as shown in Figure 2.13a and Table 2.5. The metallic Co^0 is also observed at 776.3 eV. Also, the peaks at 779.7 and 795.3 eV correspond to Co^{2+} at the octahedral sites, while the peaks at 782.2 and 796.98 eV indicated Co^{3+} at the tetrahedral sites [48]. Compared to pure $CoFe_2O_4$ nanoparticles[45] and 20% $CoFe_2O_4$ Graphite, the peak for Co-N at 773.4 eV was not observed, also the peaks for Co^{2+} are located at 780.7 and 796.3 eV which are shifted by 1.0 eV. These are the evidence that SMSI is also observable in 20%$CoFe_2O_4$ PBI at Co 2p region. When compared to Co PBI, the satellites peak of 20%$CoFe_2O_4$ PBI was much stronger due to the Fe LMM line[48,49].

Fe2p spectrum of 20%$CoFe_2O_4$ PBI revealed 7 peaks. The peaks at 709.6 and 722.7 eV correspond to the binding energy of Fe^{3+} $2p_{3/2}$ and Fe^{3+} $2p_{1/2}$ at the octahedral sites, respectively. Besides, the binding energy at 712.1 and 724.8 eV correspond to Fe^{3+} $2p_{3/2}$ and Fe^{3+} $2p_{1/2}$ at the tetrahedral sites as illustrated in Figure 2.13b and Table 2.6. Moreover, the

strong satellite peak at 717.8 eV could potentially indicate the existence of a minor quantity of Fe^{2+} in the sample[48,49]. In comparison to Fe PBI, they exhibit similar Fe^{3+} species. The pure $CoFe_2O_4$ nanoparticles [12] and 20% $CoFe_2O_4$ Graphite show peaks at 710.9 and 724.2 eV in Fe 2p region. The broader satellite peaks at 717.8 and 728.9 eV are overlaid by the Auger line originating from the Co. Thus, decorating $CoFe_2O_4$ nanoparticles on PYPBI800 was shown to cause a peak shift by 1.0 – 1.5 eV confirming the SMSI[50,51]. From XPS results, the structure of $CoFe_2O_4$ is partially inversed spinel type which could be represented by $(Co_{0.2}Fe_{0.80})_{Tet}(Co_{0.86}Fe_{1.14})_{Oct}O_4$.

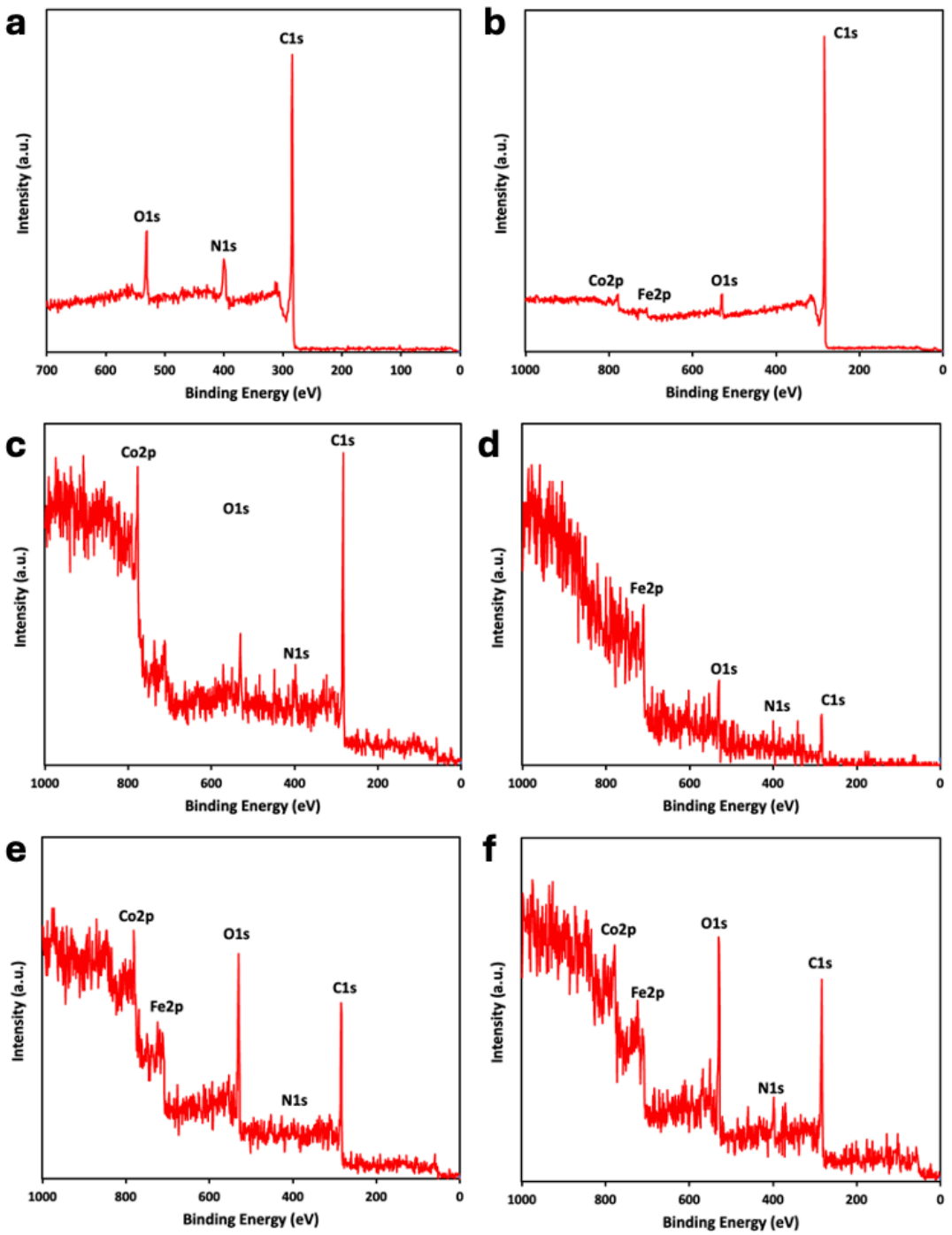

Figure 2.10 XPS survey spectra for a) PYPBI800, b) 20%$CoFe_2O_4$ Graphite, c) Co PBI, d) Fe PBI, e) 10%$CoFe_2O_4$ PBI, and f) 20%$CoFe_2O_4$ PBI

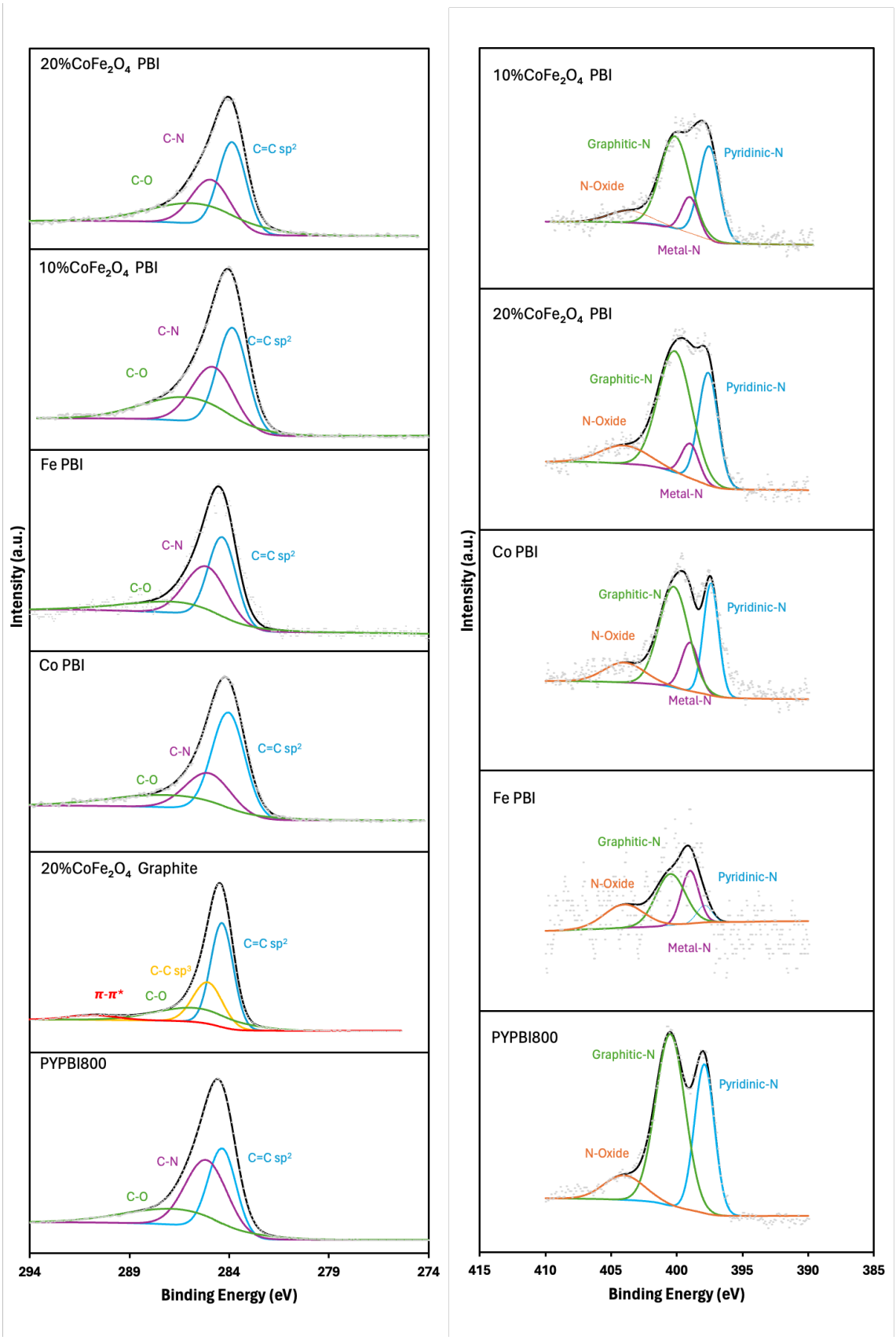

Figure 2.11 XPS spectra of PYPBI800, 20%$CoFe_2O_4$ Graphite, Co PBI, Fe PBI, 10%$CoFe_2O_4$ PBI, and 20%$CoFe_2O_4$ PBI at a) C 1s region and b) N 1s region.

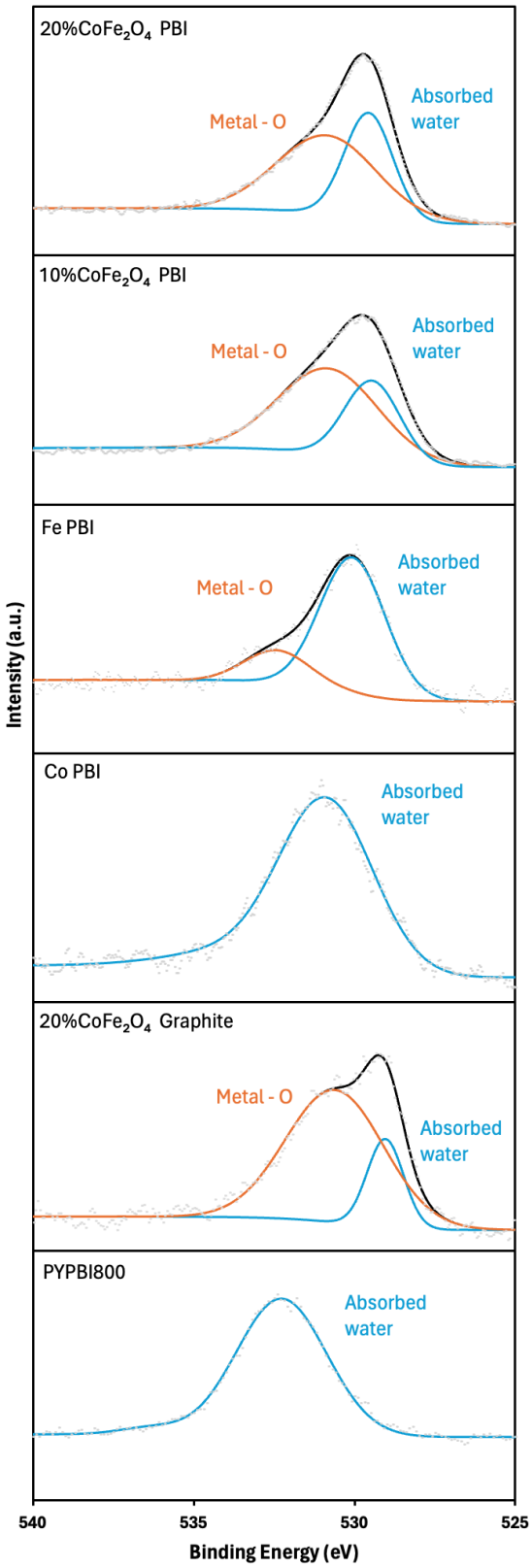

Figure 2.12 XPS spectra at O 1s region of PYPBI800, 20%$CoFe_2O_4$ Graphite, Co PBI, Fe PBI, 10%$CoFe_2O_4$ PBI, and 20%$CoFe_2O_4$ PBI

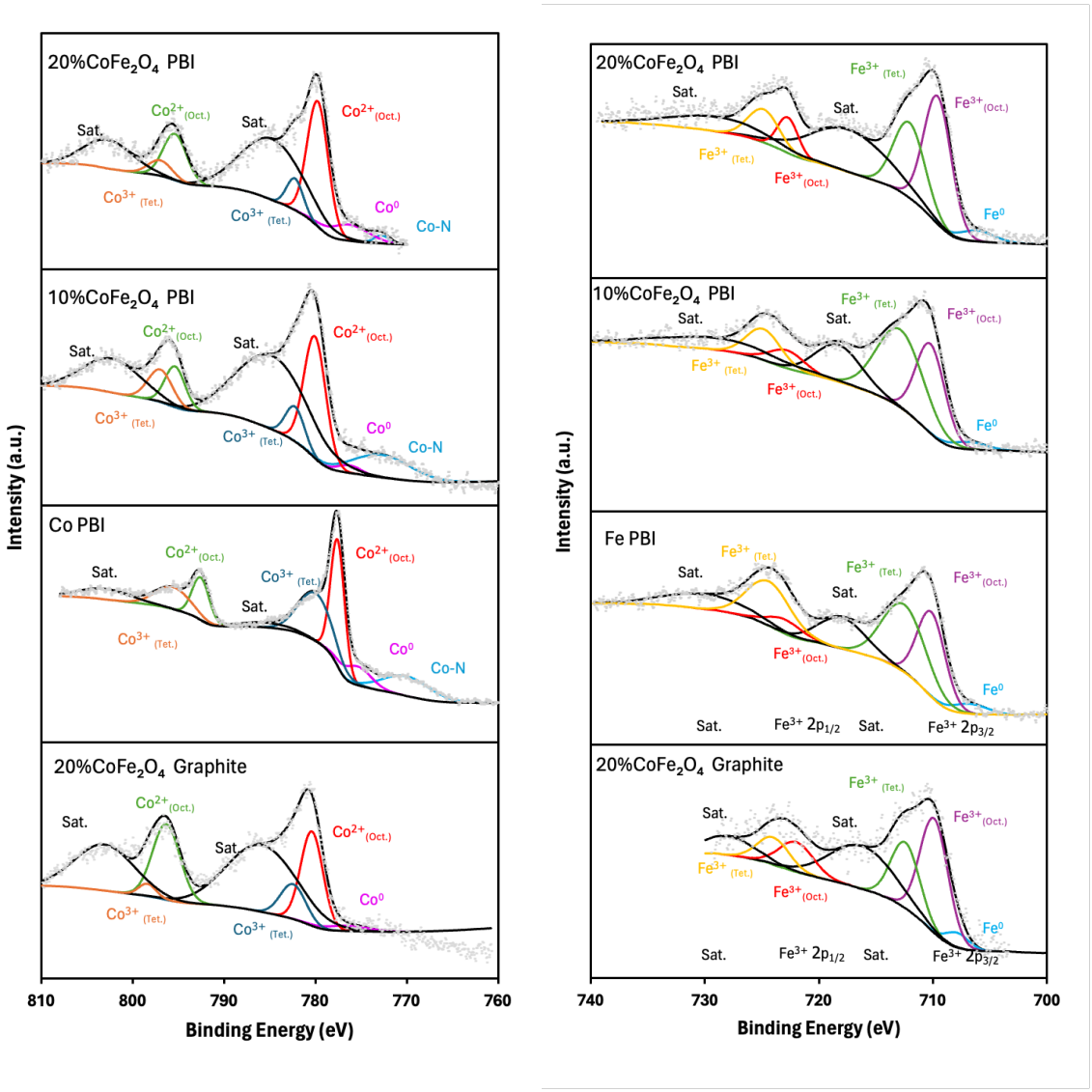

Figure 2.13 XPS spectra of PYPBI800, 20%CoFe2O4 Graphite, Co PBI, Fe PBI, 10%CoFe2O4 PBI, and 20%CoFe2O4 PBI at a) Co 2p region and b) Fe 2p region.

Table 2.2 Peaks corresponded to C 1s region of XPS spectra

Electrocatalysts	C 1s (eV)				
	C – C	C – N	C – O	C – C(sp^3)	π – π*
PYPBI800	284.4	285.1	286.6	-	-
Co PBI	284.1	285.0	286.9	-	-
Fe PBI	284.4	285.1	286.6	-	-
10%$CoFe_2O_4$ PBI	283.8	284.8	286.1	-	-
20%$CoFe_2O_4$ PBI	283.9	284.9	285.7	-	-
20%$CoFe_2O_4$ Graphite	284.4	-	285.6	285.0	290.8

Table 2.3 Peaks corresponded to N 1s region of XPS spectra

Electrocatalysts	N 1s (eV)			
	Pyridiinc-N	Metal-N	Graphitic-N	N-oxide
PYPBI800	397.9	-	400.5	404.0
Co PBI	397.4	399.0	400.2	404.0
Fe PBI	397.9	399.0	400.5	404.0
10%$CoFe_2O_4$ PBI	397.9	399.0	400.5	404.0
20%$CoFe_2O_4$ PBI	397.6	399.0	400.1	404.0
20%$CoFe_2O_4$ Graphite	-	-	-	-

Table 2.4 Peaks corresponded to O 1s region of XPS spectra

Electrocatalysts	O 1s (eV)		
	Absorbed water	Metal-O	O_2 Defects
PYPBI800	532.3	-	-
Co PBI	530.9	-	-
Fe PBI	530.0	532.4	-
10%$CoFe_2O_4$ PBI	530.8	529.5	-
20%$CoFe_2O_4$ PBI	530.8	529.5	-
20%$CoFe_2O_4$ Graphite	531.5	-	529.8

Table 2.5 Peaks corresponded to Co 2p region of XPS spectra

Electrocatalysts	Co 2p (eV)					
	Co-N	Metallic Co	Co^{3+} $2p_{3/2\ (Tet)}$	Co^{3+} $2p_{1/2\ (Tet)}$	Co^{2+} $2p_{3/2\ (Oct)}$	Co^{2+} $2p_{1/2\ (Oct)}$
PYPBI800	-	-	-	-		
Co PBI	770.0	775.4	777.6	792.6	780.7	796.1
Fe PBI	-	-	-	-		
10%$CoFe_2O_4$ PBI	772.7	776.3	782.2	796.9	780.0	795.4
20%$CoFe_2O_4$ PBI	772.7	776.3	782.2	796.9	779.7	795.4
20%$CoFe_2O_4$ Graphite	-	776.6	782.4	798.4	780.4	796.3

Table 2.6 Peaks corresponded to Fe 2p region of XPS spectra

Electrocatalysts	Fe 2p (eV)					
	Fe^{2+} (Sat.)	Metallic Fe	Fe^{3+} $2p_{3/2\ (Tet)}$	Fe^{3+} $2p_{1/2\ (Tet)}$	Fe^{3+} $2p_{3/2\ (Oct)}$	Fe^{3+} $2p_{1/2\ (Oct)}$
PYPBI800	-	-	-	-		
Co PBI	-	-	-	-		
Fe PBI	718.0	706.8	712.5	724.4	710.1	723.0
10%$CoFe_2O_4$ PBI	718.3	706.8	712.9	724.9	710.2	722.8
20%$CoFe_2O_4$ PBI	717.4	706.2	712.1	724.9	709.1	722.7
20%$CoFe_2O_4$ Graphite	716.23	707.9	712.4	724.0	709.9	722.0

2.4 Electrocatalytic Performance of Electrocatalysts

To get insight into the catalytic activity of 20%$CoFe_2O_4$ PBI toward ORR and OER, the electrocatalytic activity of the 20%$CoFe_2O_4$ PBI in 0.1 M LiTFSI in TEGDME was investigated using a standard three-electrode configuration. PBI800, Co PBI, Fe PBI, 10%$CoFe_2O_4$ PBI, and 30%$CoFe_2O_4$ PBI were also tested for comparison. Figure 2.14a displays the CV curves for PBI800, Co PBI, Fe PBI, and 20%$CoFe_2O_4$ PBI electrocatalysts, recorded at a scan rate of 50 mV/s. All the electrocatalysts exhibit a distinct ORR peak in the CV curves recorded under an O_2 atmosphere. Notably, there are discernible differences in the limiting current density for each case. Interestingly, 20%$CoFe_2O_4$ PBI electrocatalyst demonstrates a significantly higher limiting current density of -4.07 $mAcm^{-2}$ compared to the others. Upon comparison across 10% and 30% loadings of $CoFe_2O_4$, the CV shows that the 20%$CoFe_2O_4$ PBI loading remains to have the highest limiting current density as shown in Figure 2.14b. Similarly, the OER part of CV shows that 20%$CoFe_2O_4$ PBI has the highest current density. The results suggest that the 20%$CoFe_2O_4$ PBI electrocatalyst exhibits superior electrocatalytic activity toward ORR and OER when compared to the other electrocatalysts. Due to the synergized of Co and Fe in the spinel $CoFe_2O_4$ structure, six possible pathways towards OER have been proposed[52]. The coulombic efficiency of each electrocatalyst was separately calculated from CV cathodic and anodic region. As shown in Figure 2.15, 20%$CoFe_2O_4$ PBI has the coulombic efficiency of 83% which is significantly improved compared to PYPBI800 with 59%. The coulombic efficiency of Co PBI, Fe PBI, 10%$CoFe_2O_4$ PBI, and 30%$CoFe_2O_4$ PBI are 70%, 70%, 80%, and 66%, respectively. Thus, 20%$CoFe_2O_4$ PBI has the highest reversibility compared to other electrocatalysts. The 20%$CoFe_2O_4$ PBI exhibits a highest limiting current density due to the conductivity of the $CoFe_2O_4$ nanoparticles, concluding that the results aligns with the electrochemical impedance

spectroscopy data. As depicted in Figure 2.16a, R_s represents the ohmic resistance of the electrode – electrolyte interface, according to the high-frequency intercept of the semicircle on the real axis. The combination of charge-transfer resistance (R_{ct}) and the double layer capacitance (C_{dl}) are indicated by the semicircle in the high- and medium-frequency regions. The tail in the low-frequency Warburg-like emerges from electric double layer formation (steep slope region) and diffusion-controlled process (low slope region) [53]. The transmission line model (TLM) has been employed to analyze the impedance characteristics of porous electrodes in Li-ion batteries, metal-O_2, and LABs [54–56]. Specifically, the Warburg-like linear region in TLM corresponds to the resistance of ionic resistance in the pores (R_{ion}) [57]. The Warburg-like projection can be used to estimated R_{ion} impedance. According to the fitted results in Figure 2.16b, the ohmic resistance (R_s) the electrocatalysts at open circuit voltage (OCV) are approximately 700 – 900 Ω, except Co PBI which has the R_s at 1,043 Ω. However, Co PBI exhibits lowest R_{ct} according to conductivity of metallic cobalt. The R_{ct} of the electrocatalysts are approximately 2200 – 2500 Ω. However, a notable difference is observed in the R_{ion}. The R_{ion} of the 20%$CoFe_2O_4$ PBI electrode is measured to be 1688.1 Ω, compared to 1,009.5 Ω for the PYPBI800 electrode, suggesting a lower ionic transfer process in the pore for the 20%$CoFe_2O_4$ PBI electrode. Based on R_{ion}, by decorating $CoFe_2O_4$ nanoparticles on PYPBI800, the conductivity of the $CoFe_2O_4$ nanoparticles has increased. As depicted in Table 2.7, PYPBI800 has the least R_{ion}, and the R_{ion} increased with higher loading of metal oxides. However, in the case of Co PBI, the particles size was much finer according to the SEM result. Thus, these finer particles were able to block the pores resulted as higher R_{ion} at the same metal loading.

The Fe^{3+} sites in $CoFe_2O_4$ PBI serve as reaction centers for OER, while the Co^{2+} sites provide conductivity and favorable synergetic effects for Fe^{3+} sites [52,58]. Also, the extensive surface area with N heteroatom defects of the PBI provides abundant nucleation sites for $CoFe_2O_4$ nanoparticles which serve as active sites for ORR and OER. The $CoFe_2O_4$ nanoparticles formed on the support exhibit SMSI which leads to high electrocatalytic activity and stability. The SMSI enhance the resistance to poisonous species which might occur during ORR and OER [59].

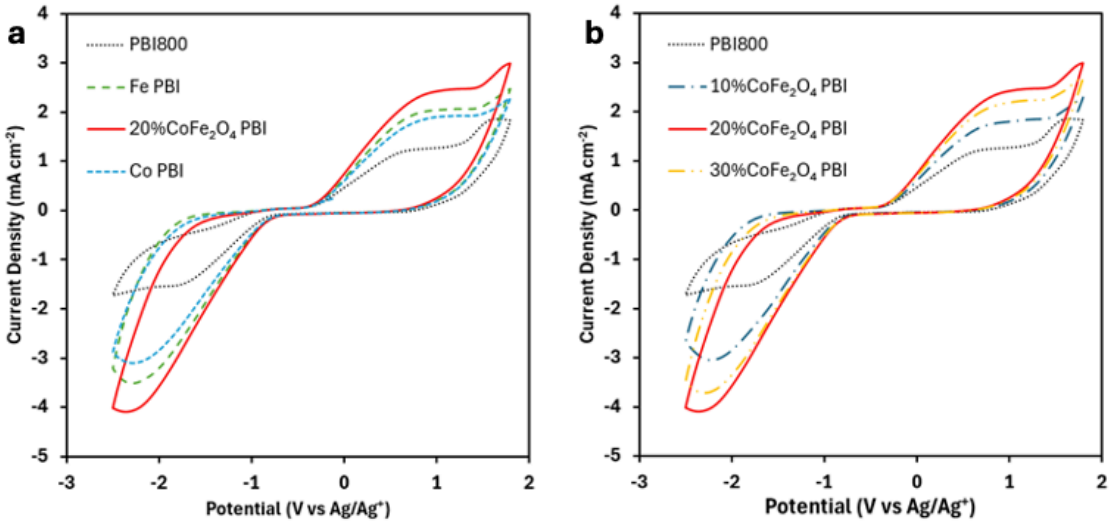

Figure 2.14 CV plot comparing a) different metal content and b) different metal loading at 1600 rpm at a scan rate of 50 mVs^{-1} in 0.1 M LiTFSI in TEGDME under O_2 atmosphere.

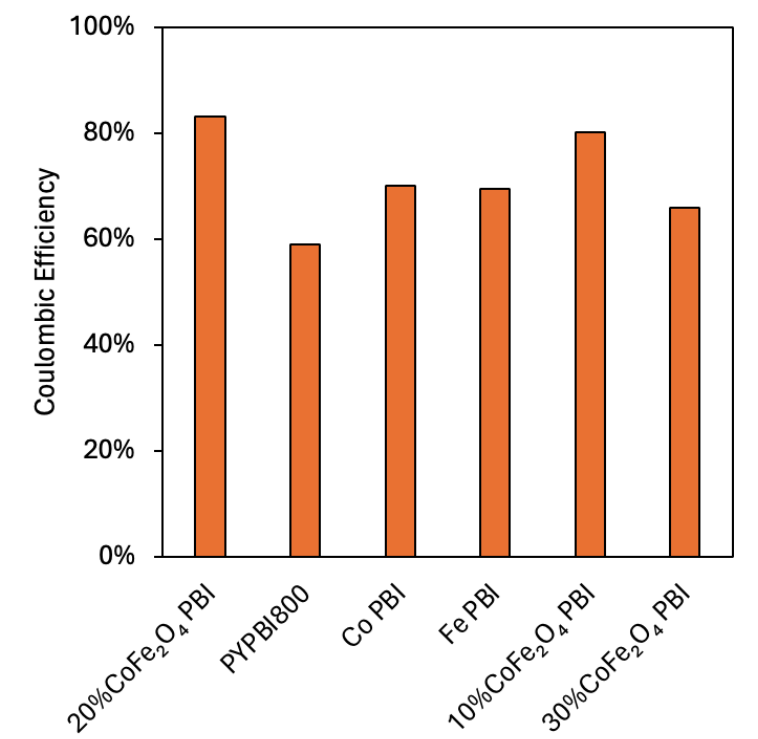

Figure 2.15 Coulombic efficiency of electrocatalyst calculated from CV at 1600 rpm at a scan rate of 50 mVs^{-1} in 0.1 M LiTFSI in TEGDME under O_2 atmosphere.

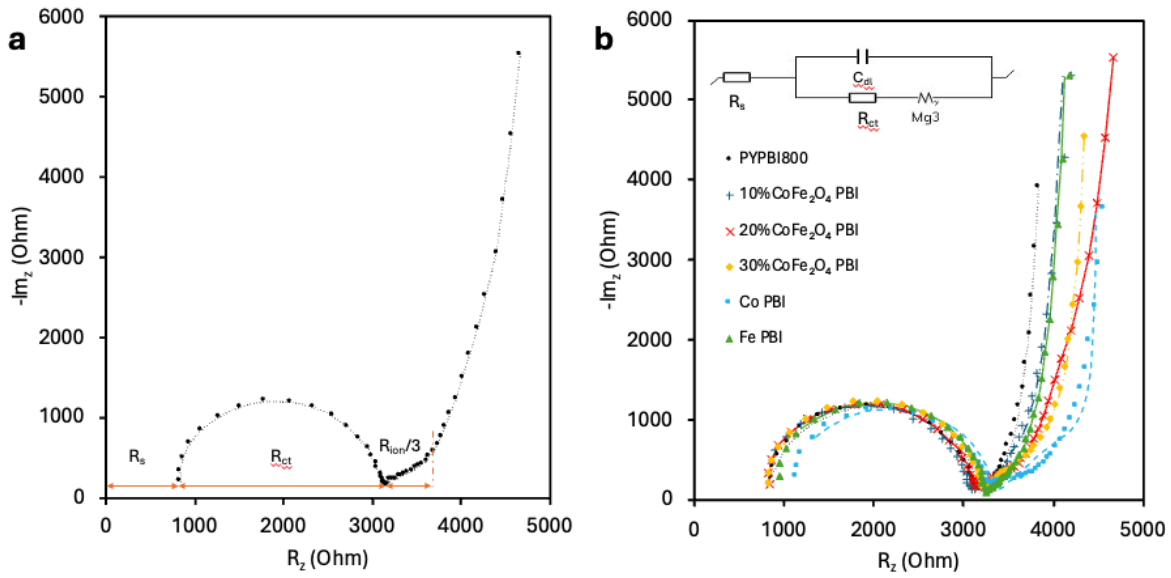

Figure 2.16 Potentiostatic electrochemical impedance spectroscopy of electrocatalyst calculated at 1600 rpm in 0.1 M LiTFSI in TEGDME under O_2 atmosphere.

Table 2.7 Potentiostatic electrochemical impedance spectroscopy parameter from Nyquist plot fitting

Electrocatalyst	R_s (Ω)	R_{ct} (Ω)	R_{ion} (Ω)
PYPBI800	828.5	2325	1009.5
10%$CoFe_2O_4$ PBI	723.5	2356	1561.5
20%$CoFe_2O_4$ PBI	733.3	2404	1688.1
30%$CoFe_2O_4$ PBI	769.1	2417	2204.7
Co PBI	1043.0	2256	2709.0
Fe PBI	806.6	2425	1651.2

2.5 Conclusions

In this study, spinel $CoFe_2O_4$ decorated on PYPBI800 were synthesized as electrocatalyst. $CoFe_2O_4$ with the size of 15 – 20 nm were well distributed according to SEM images. On the other hand, XRD and HR-TEM confirmed the formation of the spinel structure of $CoFe_2O_4$. More importantly, the strong metal-substrate interaction (SMSI) is confirmed by the developed metal-N peak in N1s region of XPS spectra. Furthermore, the shifted peaks in both Co2p and Fe2p regions of XPS spectra also indicate the SMSI from the $CoFe_2O_4$ decorated on PYPBI800 electrocatalysts. The bifunctional electrocatalytic activity toward ORR and OER was enhanced by the SMSI due to the bonding state of Co^{2+} and Fe^{3+} in the spinel structure as the active sites. Remarkably, the 20%$CoFe_2O_4$ PBI electrocatalysts exhibited an improved catalytic limiting current density compared to other synthesized electrocatalysts. The catalytic activity of 20%$CoFe_2O_4$ PBI can be attributed to the synergistic contribution of $CoFe_2O_4$ nanoparticles, and the N doped carbon support network.

References

1. N. Imanishi, O. Yamamoto, *Mater Today Adv*, 4 (2019).
2. T. Liu, J.P. Vivek, E.W. Zhao, J. Lei, N. Garcia-Araez, C.P. Grey, *Chem Rev*, 120 (2020).
3. K.N. Jung, J. Kim, Y. Yamauchi, M.S. Park, J.W. Lee, J.H. Kim, *J Mater Chem A Mater*, 4 (2016) 14050–14068.
4. K. Surya, M.S. Michael, S.R.S. Prabaharan, *Solid State Ion*, 317 (2018) 89–96.
5. D.U. Lee, P. Xu, Z.P. Cano, A.G. Kashkooli, M.G. Park, Z. Chen, *J Mater Chem A Mater*, 4 (2016) 7107–7134.
6. A.M. Kannan, A.K. Shukla, S. Sathyanarayana, *J Power Sources*, 25 (1989) 141–150.
7. H.M. Zhang, Y. Shimizu, Y. Teraoka, N. Miura, N. Yamazoe, *J Catal*, 121 (1990) 432–440.
8. H. Tanaka, M. Misono, *Curr Opin Solid State Mater Sci*, 5 (2001) 381–387.
9. J. Zhang, Y. Zhao, X. Zhao, Z. Liu, W. Chen, *Sci Rep*, 4 (2014).
10. Y. Yan, Y. Xu, B. Zhao, Y. Xu, Y. Gao, G. Chen, W. Wang, B.Y. Xia, *J Mater Chem A Mater*, 8 (2020) 5070–5077.
11. Y. Li, Z. Zhou, G. Cheng, S. Han, J. Zhou, J. Yuan, M. Sun, L. Yu, *Electrochim Acta*, 341 (2020) 135997.
12. W. Bian, Z. Yang, P. Strasser, R. Yang, *J Power Sources*, 250 (2014) 196–203.
13. W. Yan, W. Bian, C. Jin, J.H. Tian, R. Yang, *Electrochim Acta*, 177 (2015) 65–72.
14. C.V. Rao, C.R. Cabrera, Y. Ishikawa, *Journal of Physical Chemistry Letters*, 1 (2010) 2622–2627.
15. T. Li, Y. Lv, J. Su, Y. Wang, Q. Yang, Y. Zhang, J. Zhou, L. Xu, D. Sun, Y. Tang, T. Li, Y. Lv, J. Su, Y. Wang, Q. Yang, L. Xu, D. Sun, Y. Tang, Y. Zhang, J. Zhou, *Advanced Science*, 4 (2017) 1700226.
16. J. Lai, C. Zeng, S. Peng, Q. Zhou, J. Zeng, C. Liu, X. Qi, *J Power Sources*, 599 (2024) 234218.
17. H. Safardoust-Hojaghan, M. Salavati-Niasari, *J Clean Prod*, 148 (2017) 31–36.
18. L. Li, C. Tang, Y. Zheng, B. Xia, X. Zhou, H. Xu, S.Z. Qiao, *Adv Energy Mater*, 10 (2020) 2000789.
19. S. Park, J. Kim, K. Kwon, *Chemical Engineering Journal*, 446 (2022) 137116.
20. Z. Li, C. Gao, H. Zhao, A. Meng, S. Ding, X. Wang, S. Li, *J Alloys Compd*, 897 (2022) 163175.

21. X. Duan, J. Xu, Z. Wei, J. Ma, S. Guo, S. Wang, H. Liu, S. Dou, *Advanced Materials*, 29 (2017) 1701784.

22. K. Gao, B. Wang, L. Tao, B. V. Cunning, Z. Zhang, S. Wang, R.S. Ruoff, L. Qu, *Advanced Materials*, 31 (2019) 1805121.

23. W. Liu, J. Qi, P. Bai, W. Zhang, L. Xu, *Appl Catal B*, 272 (2020) 118974.

24. S. Kramer, J. Mielby, K. Buss, T. Kasama, S. Kegnæs, *ChemCatChem*, 9 (2017) 2930–2934.

25. H. Wang, T. Maiyalagan, X. Wang, *ACS Catal*, 2 (2012) 781–794.

26. S. Pylypenko, A. Borisevich, K.L. More, A.R. Corpuz, T. Holme, A.A. Dameron, T.S. Olson, H.N. Dinh, T. Gennett, R. O'Hayre, *Energy Environ Sci*, 6 (2013) 2957–2964.

27. B. Peter, J. Melke, F. Muench, W. Ensinger, C. Roth, *J Appl Electrochem*, 44 (2014) 573–580.

28. T. Holme, Y. Zhou, R. Pasquarelli, R. O'Hayre, *Physical Chemistry Chemical Physics*, 12 (2010) 9461–9468.

29. H. Wang, Y. Shao, S. Mei, Y. Lu, M. Zhang, J.K. Sun, K. Matyjaszewski, M. Antonietti, J. Yuan, *Chem Rev*, 120 (2020) 9363–9419.

30. R.M. Cywar, N.A. Rorrer, C.B. Hoyt, G.T. Beckham, E.Y.X. Chen, *Nature Reviews Materials 2021 7:2*, 7 (2021) 83–103.

31. C.; Yang, H.; Wu, M.; Cai, Y.; Zhou, C.; Guo, Y.; Han, L. Zhang, C. Yang, H. Wu, M. Cai, Y. Zhou, C. Guo, Y. Han, L. Zhang, *Polymers 2023, Vol. 15, Page 2741*, 15 (2023) 2741.

32. J.A. Asensio, P. Gómez-Romero, *Fuel Cells*, 5 (2005) 336–343.

33. S.C. Kumbharkar, U.K. Kharul, *J Memb Sci*, 360 (2010) 418–425.

34. A. Nag, M.A. Ali, H. Kawaguchi, S. Saito, Y. Kawasaki, S. Miyazaki, H. Kawamoto, D.T.N. Adi, K. Yoshihara, S. Masuo, Y. Katsuyama, A. Kondo, C. Ogino, N. Takaya, T. Kaneko, Y. Ohnishi, *Adv Sustain Syst*, 5 (2021) 2000193.

35. K.S. Patnaik, R. Badam, Y. Peng, K. Higashimine, T. Kaneko, N. Matsumi, *Chemical Communications*, 57 (2021).

36. L. Zhou, K. Higashimine, R. Badam, N. Matsumi, *Mater Res Express*, 10 (2023) 125508.

37. Y. Yang, Q. Sun, Y.S. Li, H. Li, Z.W. Fu, *J Power Sources*, 223 (2013) 312–318.

38. W. Bian, Z. Yang, P. Strasser, R. Yang, *J Power Sources*, 250 (2014) 196–203.

39. T. Şener, E. Kayhan, M. Sevim, Ö. Metin, *J Power Sources*, 288 (2015) 36–41.

40. M. Athika, P. Elumalai, *ChemElectroChem*, 7 (2020) 4188–4200.

41. M. V. Kharlamova, *Nanomaterials 2021, Vol. 11, Page 2500*, 11 (2021) 2500.

42. Y. So, H.S. Bae, Y.Y. Kang, J.Y. Chung, N.K. Park, J. Kim, H.T. Jung, J.C. Won, M.H. Ryou, Y.H. Kim, *Nanomaterials*, 11 (2021) 3164.

43. J. V. Rojas, M. Toro-Gonzalez, M.C. Molina-Higgins, C.E. Castano, *Materials Science and Engineering: B*, 205 (2016) 28–35.

44. Q. Wang, Y. Ji, Y. Lei, Y. Wang, Y. Wang, Y. Li, S. Wang, *ACS Energy Lett*, 3 (2018) 1183–1191.

45. J. Melke, B. Peter, A. Habereder, J. Ziegler, C. Fasel, A. Nefedov, H. Sezen, C. Wöll, H. Ehrenberg, C. Roth, *ACS Appl Mater Interfaces*, 8 (2016) 82–90.

46. S. Li, J. Wang, J. Wang, C. Chen, Z. Guo, N. Cai, Y. Xue, F. Yu, *Colloids Surf A Physicochem Eng Asp*, 626 (2021) 126898.

47. J. Ma, Q. Wu, W. Zhang, Y. Li, Y. Lu, B. Liu, F. Yang, Y. Song, *Electrochim Acta*, 432 (2022) 141224.

48. Q. Huang, P. Zhou, H. Yang, L. Zhu, H. Wu, *Chemical Engineering Journal*, 325 (2017) 466–473.

49. A. Kostuch, J. Gryboś, S. Wierzbicki, Z. Sojka, K. Kruczała, *Materials 2021, Vol. 14, Page 820*, 14 (2021) 820.

50. R. Badam, R. Vedarajan, K. Okaya, K. Matsutani, N. Matsumi, *Scientific Reports 2016 6:1*, 6 (2016) 1–7.

51. R. Badam, M. Hara, H.H. Huang, M. Yoshimura, *Int J Hydrogen Energy*, 43 (2018) 18095–18104.

52. Ö.N. Avcl, L. Sementa, A. Fortunelli, *ACS Catal*, 12 (2022) 9058–9073.

53. B.A. Mei, O. Munteshari, J. Lau, B. Dunn, L. Pilon, *Journal of Physical Chemistry C*, 122 (2018) 194–206.

54. A. Chamaani, M. Safa, N. Chawla, B. El-Zahab, *ACS Appl Mater Interfaces*, 9 (2017) 33819–33826.

55. K.B. Knudsen, T. Vegge, B.D. McCloskey, J. Hjelm, *J Electrochem Soc*, 163 (2016) A2065–A2071.

56. K.B. Knudsen, J.E. Nichols, T. Vegge, A.C. Luntz, B.D. McCloskey, J. Hjelm, *Journal of Physical Chemistry C*, 120 (2016) 10799–10805.

57. N. Ogihara, S. Kawauchi, C. Okuda, Y. Itou, Y. Takeuchi, Y. Ukyo, *J Electrochem Soc*, 159 (2012) A1034–A1039.

58. G.A. Gebreslase, M.V. Martínez-Huerta, D. Sebastián, M.J. Lázaro, *J Colloid Interface Sci*, 625 (2022) 70–82.

59. Z. Shi, W. Yang, Y. Gu, T. Liao, Z. Sun, Z. Shi, W. Yang, Y. Gu, T. Liao, Z. Sun, *Advanced Science*, 7 (2020) 2001069.

Chapter 3 $CoFe_2O_4$ Nanoparticles on Bio-based Polymer Derived Nitrogen Doped Carbon as Bifunctional Electrocatalyst for Li-air Battery

Abstract

Lithium-air batteries (LABs) are gaining attention as a promising energy storage solution. Their theoretical energy density of 3,505 $Whkg^{-1}$ exceeds that of conventional lithium-ion batteries (500 – 800 $Whkg^{-1}$). The commercial viability and widespread adoption of lithium-air batteries face challenges such as poor cycling stability, limited lifespan, and unresolved side reactions. In this study, we synthesized spinel $CoFe_2O_4$-decorated on bio-based poly(2,5-benzimidazole) derived N-doped carbon for electrocatalysts. Notably, strong metal-substrate interaction (SMSI) was observed through various characterizations. The bifunctional electrocatalytic activity and stability toward oxygen reduction reaction (ORR) and oxygen evolution reaction (OER) were significantly enhanced by the SMSI, The LAB (lithium-air battery) demonstrated a high discharge capacity of 18,356 $mAhg^{-1}$ at a current density of 200 mAg^{-1}, maintaining a remarkable discharge capacity of 1,000 $mAhg^{-1}$ even at a high current density of 400 mAg^{-1} for 200 cycles. $CoFe_2O_4$-decorated on bio-derived ABPBI holds promise as a practical air-breathing electrode for high-capacity rechargeable LABs.

3.1 Introduction

Lithium-ion batteries (LIBs) have been widely used as rechargeable energy sources for portable electronic devices over the past few decades. While cutting-edge LIBs have demonstrated a 10-year operational lifespan and have been successful in consumer electronics, they do not meet the energy-density demands required for grid-scale energy storage. Given the growing energy requirements of modern devices such as smartphones, laptops, and tablets, there is a concerted effort to enhance the capacity of existing Li-ion batteries. Researchers are actively exploring alternative active materials to create more cost-effective LIBs with significantly higher energy density, all while ensuring acceptable cycle life and safety

On the other hand, the global scientific community has long recognized the pressing need for advanced energy storage systems. Among the various options, lithium-air batteries (LABs) stand out due to their exceptional theoretical energy density of 3,505 $Whkg^{-1}$ [1], surpassing that of typical lithium-ion batteries (500–800 $Whkg^{-1}$)[2]. LABs leverage atmospheric oxygen

as a reactant, but practical challenges such as poor cycling stability, limited lifespan, and unresolved side reactions hinder their commercial viability [3]. Addressing these obstacles through rigorous research and development efforts is crucial. The primary challenges lie in the air cathode, which comprises porous material for Li_2O_2 storage and electrocatalysts to facilitate oxygen reduction and evolution reactions. Developing efficient electrocatalysts is essential to realize LABs' full theoretical potential.

Consequently, the imperative for rigorous research and development efforts aimed at overcoming these obstacles cannot be overstated. The air cathode which consists of porous material to store Li_2O_2 and electrocatalysts to facilitate oxygen reduction reaction (ORR) and oxygen evolution reaction (OER) are the major components that affect LABs performance. The sluggish oxygen kinetics from these reactions are a major issue that hindered their performance compared to their theoretical performance. Hence, researchers have been developing electrocatalysts to enhance ORR/OER electrocatalytic activity to achieve the theoretical performance of LABs.

In recent times, researchers have investigated the modification of LAB cathode in several aspects including morphology/nanostructure engineering, heteroatom doping, defect engineering, and functionalization engineering[4]. According to the chemical and physical properties, nanostructured materials have recently garnered significant interest as electrodes for LABs. Moreover, the shape, particle size of these nanostructured electrodes, and the influence of the support material play a crucial role in their electrocatalytic performance. Various metal or metal oxide nanoparticles have been employed in electrochemical energy storage devices to deliver both high power and high energy density, thanks to their large surface-to-volume ratio. For instance, cobalt ferrite ($CoFe_2O_4$) nanoparticles have been investigated as cathode electrocatalysts in LABs. While bulk $CoFe_2O_4$ was shown to offer a high initial discharge capacity, it experienced a swift initial capacity fade. This capacity drop issue could be resolved by either altering the size and shape of the $CoFe_2O_4$ electrode or supporting it on carbonaceous materials. Cao and co-workers demonstrated an increase in capacity by using graphene as a support material for $CoFe_2O_4$ in LAB, increasing from 1200 $mAhg^{-1}$ of $CoFe_2O_4$ to 2116 $mAhg^{-1}$ of the combined graphene and $CoFe_2O_4$[5]. However, the commercialization of carbon nanotubes and graphene is currently challenging, time-intensive, and expensive. As a result, Vulcan XC-72, a commercial and inexpensive carbon support material with excellent electrical and thermal conductivity, has been used for creating uniformly dispersed and more cost-effective $CoFe_2O_4$-based designs by Sener et al[6]. The different loading of $CoFe_2O_4$ on Vulcan XC-72 was employed as LAB cathodes. At 16.4 %wt

loading, the higest capacity for LAB was 7510 $mAhg^{-1}$.

Moreover, decoration of $CoFe_2O_4$ on heteroatom doped carbon support is able to promote LAB performance. Gong et al presented a composite of inverse spinel $Co[Co,Fe]O_4$ and nitrogen-doped graphene (NG), which shows promise as a electrocatalyst for rechargeable Li–O_2 batteries[7]. The batteries using this $Co[Co,Fe]O_4$/NG electrocatalyst demonstrate a high initial capacity of 13292 $mAhg^{-1}$, impressive cyclability for more than 110 cycles with 1000 mAh g^{-1} cut-off capacity, and solid rate capability. Furthermore, the overpotential of the LABs is significantly lowered. The enhanced ORR and OER performances can be credited to the favorable properties of inverse spinel structure $Co[Co,Fe]O_4$ for ORR and the increased electronic conductivity of the N-doped graphene. N defects in the carbon structure play important roles. Hence, incorporating more defects to the carbon support is one the strategy to enhance LAB performance[1,4,8]

In this study, we introduced spinel cobalt iron oxide ($CoFe_2O_4$) nanoparticles decorated on pyrolyzed poly(2,5-benzimidazole) (PYPBI800) as the bifunctional electrocatalyst for LABs. The electrocatalyst was synthesized through pyrolysis of PBI followed by incipient wetness impregnation calcination on the metal precursors. The SMSI between $CoFe_2O_4$ and PYPBI800 has been confirmed with X-ray photoelectron spectroscopy. Due to synergistic properties of $CoFe_2O_4$ and the nitrogen doping, these electrocatalysts also modulate the electronic state of metals, facilitating oxygen adsorption and desorption at the electrode. When employed as an electrocatalyst in LAB, the electrocatalyst exhibited promising discharge capacity and stability over 200 cycles at 400 $mAhg^{-1}$ with low overpotential at 140 mV. To the best of our knowledge, this will be the first study to employ bio-derived PYPBI800 as a support for $CoFe_2O_4$ in LAB application.

3.2 Experimental

3.2.1 Electrocatalyst Preparation

The electrocatalysts was prepared according to the previous chapter. Briefly, The ABPBI precursor was synthesized by polycondensation of 3,4-diaminobenzoic acid (DABA) using 30 g polyphosphoric acid (PPA) as a condensation agent. The mixture was heated and stirred at 160 ºC to 200 ºC under N_2 atmosphere. The obtained ABPBI was rinsed, dried, and ground into powder. The powder was then treated with 10% KOH to remove remaining PPA, filtered, and dried. The ABPBI was then carbonized under N_2 atmosphere in a tube furnace, at 800 ºC with 5 ºC min^{-1}. The product was activated in 1 M HCl, washed, and dried. The final product, labelled as PYPBI800. PYPBI800 yield was around 25% compared to the initial monomer.

Then, PYPBI800-supported $CoFe_2O_4$ were prepared using the co-incipient wetness impregnation method. Cobalt(II) nitrate hexahydrate and iron(III) nitrate nonahydrate were dissolved in a mixture of ethylene glycol and DI water at the ratio of 3:1, respectively to obtain. Then, incorporated into PYPBI800 for a total metal loading of 20%. The samples were dried, then calcinated under N_2 atmosphere in a tube furnace, with the temperature gradually raised to 550 ºC. The samples were denoted as 20% $CoFe_2O_4$ PBI, Co PBI, and Fe PBI. Additionally, 10% and 30% $CoFe_2O_4$ were prepared to study the effects of metal loading.

3.2.2 Characterisation of Electrocatalyst

The electrocatalyst characterization has been done according to the previous chapter. Briefly, the morphology and elemental composition were examined using scanning electron microscopy with energy dispersive X-ray spectrometers (SEM-EDS), specifically the Tabletop Microscope TM3030 plus and the AZtec Series from Oxford Instruments. The size of nanoparticles, crystal plane, and composite formation were determined using a high-resolution transmission electron microscope (HR-TEM) and the JEM-ARM200F instrument. The chemical composition and oxidation state were identified using X-ray photoelectron spectroscopy (XPS) with the S-ProbeTM2803. Lastly, the X-ray diffraction (XRD) patterns were analyzed using the Smart Lab X-Ray Diffractometer with Cu Kα radiation, scanning over a 2θ range of 10° – 80° with a step size of 0.02°.

3.2.3 Electrochemical Characterisation

Electrochemical performance of the electrocatalysts was performed in rotating disk electrode RRDE-3A (ALS Japan) with three electrodes configuration in 0.1 M LiTFSI in tetra-ethylene glycol dimethyl ether (TEGDME) nonaqueous electrolyte with VSP potentiostat (Bio-logic Science Instruments). The working electrode was a 3 mm glassy carbon electrode which was polished with alumina paste to get a smooth surface. Then, the electrocatalyst ink was prepared by dissolving 3 mg of active material and 3 mg of acetylene black in 1200 µL solution of 6:4 isopropyl alcohol and deionized water. Then, Nafion™ perfluorinated resin solution 5 wt% was added as a binder for 12 µL. 2.5 µL of electrocatalyst ink was dropped on the glassy carbon electrode. The counter electrode employed the Pt coil. The reference electrode for nonaqueous electrolyte was $Ag/Ag(NO_3)$ which consisted of a silver wire and 0.01 M $AgNO_3$, 0.1 M tetrabutylammonium perchlorate in acetonitrile electrolyte. Electrochemical impedance spectroscopy (EIS) was performed to gather the impedance information of the electrocatalyst. The linear sweep voltammetry (LSV) was obtained by sweeping the potential from 0 to -2.5 V vs Ag/Ag^+ for ORR and from 0 to 0.18 V vs Ag/Ag^+

for OER at a scan rate of 5 mVs^{-1} under 1600 rpm. All experiments were carried out at 25ºC controlled temperature.

3.2.4 Li−Air Battery Fabrication and Testing

To create the battery cathode, a slurry containing active materials, acetylene black, and poly(vinylidene fluoride) (PVDF) binder in a 4:5:1 ratio was dissolved in N-methyl pyrrolidone as a solvent to obtain a uniform dispersion. The slurry was coated onto 12 mm diameter disks GDL-coated carbon cloth (MTI Corporation, BCGDL1400s). The electrode was then prepared with brush coating and followed by drying in a vacuum oven at 80°C overnight. After drying, the electrode underwent hot pressing at 80°C overnight to achieve a uniform coating thickness, each serving as a cathode in the fabricated battery. The LABs were assembled in punched 2025-coin cells. The cell base punched portion was covered by nickel mesh acting as an oxygen window. The 1.0 M LiTFSI in TEGDME, with 0.1 M LiI as a redox mediator was used as the electrolyte for the cell. Prior to the electrolyte preparation, the TEGDME trace water was remove by drying with activated molecular sieves. Glass fiber (GF/D), polypropylene (PP), and polytetrafluoroethylene (PTFE) were employed as separators. These separators were soaked with 100 µL of the electrolyte. The anode of the cell was employing a lithium disk with12 mm in diameter. The cells were assembled in an argon glovebox with oxygen and water content below 1 ppm. LABs testing took place in a custom-built, leak-proof chamber filled with oxygen. The LABs testing conditions are at 25ºC under 1 bar O_2 atmosphere. LABs evaluations were conducted using a Versastat electrochemical test station. Firstly, the initial discharge was studied with a current density of 200 mAg^{-1}, and cut-off voltage at 4.5 V and 2.0 V for charge and discharge, respectively. Then, stability tests were performed with charge and discharge capacity limited to 1,000 $mAhg^{-1}$ and a current density of 400 mAg^{-1}. The limited capacity and current density were based on the weight of the active material.

3.3 Results and Discussion

3.3.1 Characterisation of Electrocatalysts

According to the previous chapter, PYPBI800 was decorated with spinel $CoFe_2O_4$ nanoparticles through a synthesis process. The SEM images revealed that the $CoFe_2O_4$, which ranged in size from 15 to 20 nm, were evenly distributed. The formation of the spinel structure of $CoFe_2O_4$ was validated by XRD and HR-TEM. The strong metal-substrate interaction (SMSI) was evidenced by the appearance of a metal-N peak in the N1s region of the XPS

spectra. The SMSI from the $CoFe_2O_4$ decorated on PYPBI800 electrocatalysts was further indicated by the shifted peaks in the Co2p and Fe2p regions of the XPS spectra. The bifunctional electrocatalytic activity towards ORR and OER was amplified by the SMSI, along with the changes in bonding state of Co^{2+} and Fe^{3+} in the spinel structure serving as the active sites. Notably, the 20%$CoFe_2O_4$ PBI electrocatalysts displayed a significantly enhanced catalytic limiting current density compared to other synthesized electrocatalysts. The superior catalytic activity of the 20%$CoFe_2O_4$ PBI can be ascribed to the combined effect of the $CoFe_2O_4$ nanoparticles, and the N doped carbon support network.

3.3.2 Electrocatalytic Performance of Electrocatalysts

Apart from CV in the previous chapter, the ORR activity of all the synthesized electrocatalysts was further compared with IR-corrected LSV curves, acquired at a scan rate of 5 mVs^{-1} and a rotation rate of 1600 rpm. The obtained voltammograms are presented in Figure 3.1a and b. Notably, the onset potential of noble metal-based electrocatalysts in nonaqueous electrolyte is around -1.0 V vs Ag/Ag^+[9]. In contrast, the LSV curve for the $CoFe_2O_4$ PBI electrocatalysts as shown in Table 3.1, exhibits a lower onset potential of -0.85 V vs Ag/Ag^+. Remarkably, the present catalyst demonstrates significantly superior onset potential compared to that of the noble metal electrocatalyst. However, the limiting current density was lower compared to the noble metal electrocatalysts. Figure 3.1c and d present IR-corrected LSV curves for the electrocatalysts, acquired at a scan rate of 5 mVs^{-1} and a rotation rate of 1600 rpm. The OER peak that appeared at around 0.9 V vs Ag/Ag^+ in CV did not appear in LSV. It could be explained that OER in TEGDME is scan rate sensitive, so at a lower scan rate OER peak is not observable[10]. In this case, the onset for OER shifted to approximately 1.04 V vs Ag/Ag^+ as shown in Table 3.1. Combining results from CV and LSV, it could be seen that $CoFe_2O_4$ PBI electrocatalysts were able to catalyze both ORR and OER in nonaqueous electrolyte. This enhanced ORR and OER activity is a critical prerequisite for utilizing as an air-breathing electrode in LAB.

The catalytic kinetics of these electrocatalysts were additionally assessed using Tafel slopes (as shown in Figure 3.2). In ORR there are two stages of kinetics due to the TEGDME base electrolyte. The reaction moves from step 1 to step 2 rapidly as it can be seen in a single ORR peak rather than 2. Therefore, in Figure 3.2a and b, there are two values of Tafel slope from each electrocatalyst. 20%$CoFe_2O_4$ PBI exhibits the lowest Tafel slope among its counterparts which are 364.2 $mVdec^{-1}$ and 592.1 $mVdec^{-1}$ for the first and second step, respectively. However, comparing different metal loading, 10% $CoFe_2O_4$ PBI has Tafel slope

of 366.3 $mVdec^{-1}$ and 577.6 $mVdec^{-1}$ which is even lower than 20% $CoFe_2O_4$ PBI. In the case of OER as shown in Figure 3.2c and d, $CoFe_2O_4$ PBI electrocatalysts also show better performance compared to their counterparts. This observation suggests more favourable ORR and OER kinetics for the $CoFe_2O_4$ PBI electrocatalysts, specifically 10%$CoFe_2O_4$ PBI.

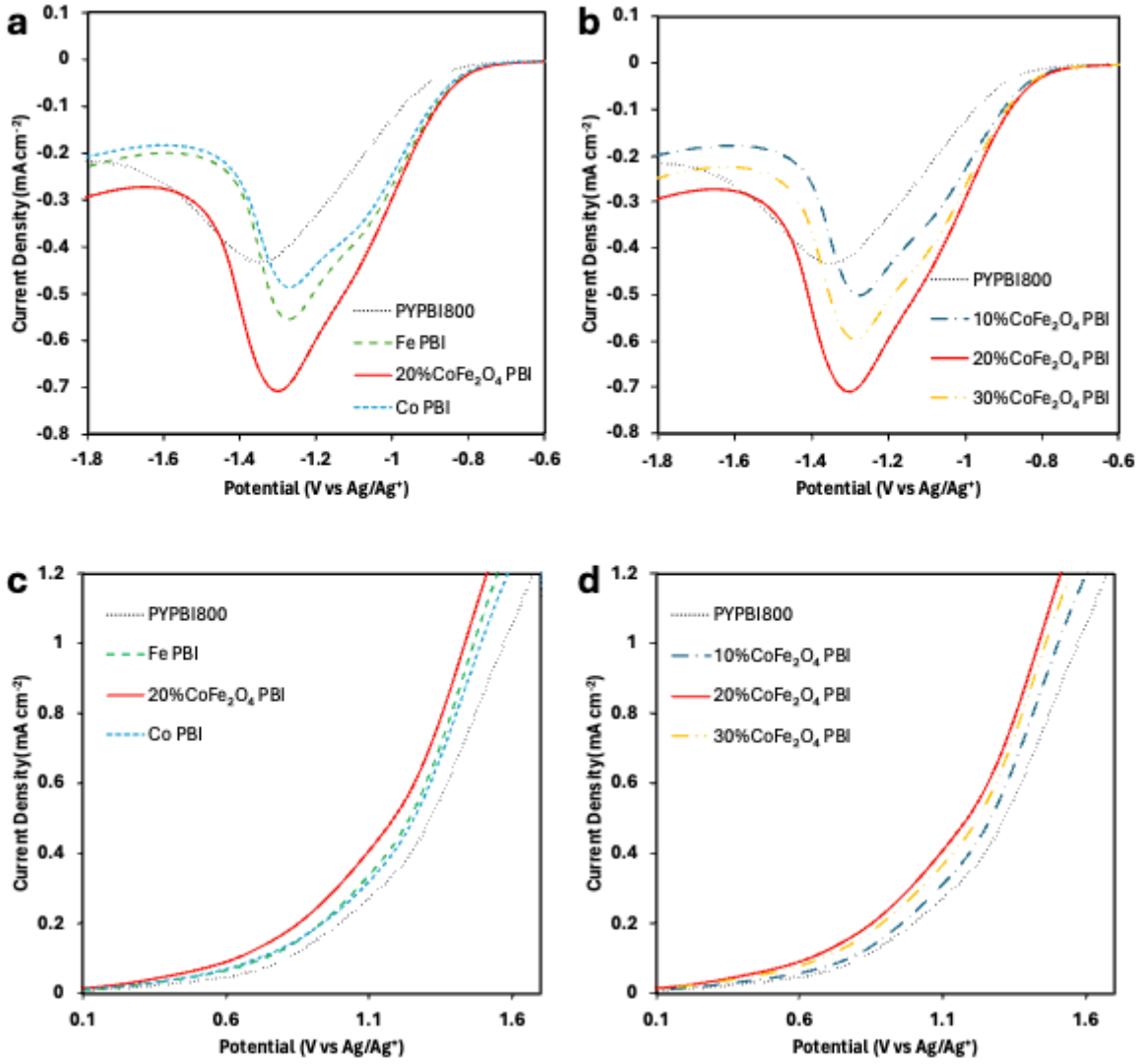

Figure 3.1 LSV plot comparing a) ORR on different metals, b), ORR on different $CoFe_2O_4$ content c) OER on different metals d) OER on different $CoFe_2O_4$ content at 1600 rpm at a scan rate of 5 mVs^{-1} in 0.1 M LiTFSI in TEGDME under O_2 atmosphere.

Table 3.1 Onset potential for ORR and OER determined from LSV at scan rate of 5 mVs^{-1} in 0.1 M LiTFSI in TEGDME under O_2 atmosphere of synthesized electrocatalysts.

Sample	ORR onset Potential (V vs Ag/Ag^+)	OER onset Potential (V vs Ag/Ag^+)
PYPBI800	-0.902	1.107
10%$CoFe_2O_4$ PBI	-0.846	1.035
20%$CoFe_2O_4$ PBI	-0.848	1.052
30%$CoFe_2O_4$ PBI	-0.847	1.02
Fe PBI	-0.845	1.044
Co PBI	-0.851	1.043

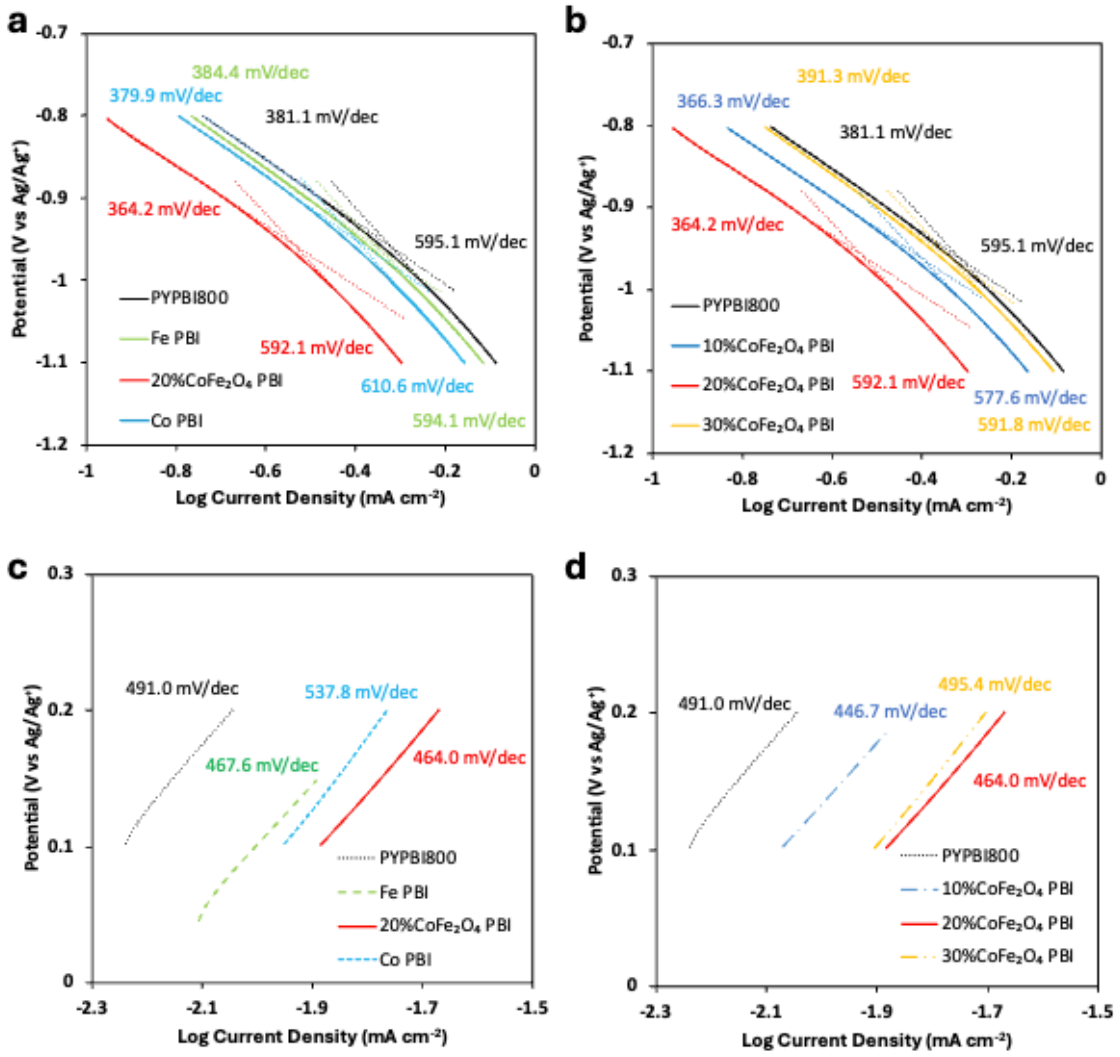

Figure 3.2 Tafel plots comparing different metal content in a) ORR and b) OER, and different metal loading in c) ORR and d) OER at 1600 rpm at a scan rate of 5 mVs^{-1} in 0.1 M LiTFSI in TEGDME under O_2 atmosphere

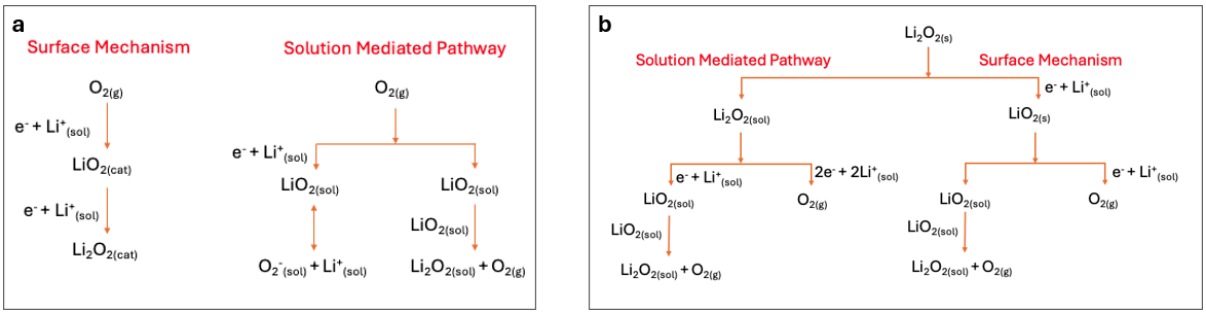

Figure 3.3 a)ORR and b)OER mechanism pathways on cathode in non-aqueous LAB

3.3.3 Li-Air Battery Evaluation

Given the remarkable ORR and OER activity demonstrated by the $CoFe_2O_4$ PBI electrocatalysts, a practical application in LABs was conducted. The electrocatalysts were evaluated as air-breathing electrodes in a CR-2032 coin-type cell LABs with their counterparts. The initial discharge curves for LAB coin cells with different electrocatalysts on the air-cathode within the 2.0 V cut-off voltage at 200 mAg^{-1} were presented in Figure 3.4a. The discharge voltage plateau for 20%$CoFe_2O_4$ PBI was observed at 2.65 V, at 2.70 V for Co PBI, 10%$CoFe_2O_4$ PBI, and 30%$CoFe_2O_4$ at 2.75 V for Fe PBI and 2.50 V for PYPBI800. The capacity of 18,356 $mAhg^{-1}$ was observed from 20%$CoFe_2O_4$ PBI, 16,595 $mAhg^{-1}$ for 10%$CoFe_2O_4$ PBI, 14,935 $mAhg^{-1}$ for 30%$CoFe_2O_4$ PBI, 2,576 $mAhg^{-1}$ for Co PBI, 4,176 $mAhg^{-1}$ for Fe PBI and 1,596 $mAhg^{-1}$ for PYPBI800. The discharge capacity of 20%$CoFe_2O_4$ PBI are comparable to the noble metal LAB[11]. The introduction of metal NPs into N-doped carbon structure significantly improved its discharge capacity. Moreover, decorating bimetallic Co-Fe NPs which later formed spinel $CoFe_2O_4$ provided a synergising effect and drastically improved the discharge capacity by 3 - 4.5 folds compared to its Fe and Co counterpart, respectively. However, too much metal loading led to the blockage of PYPBI800 pores which prevented the formation of Li_2O_2 and resulted in a lower discharge capacity in 30%$CoFe_2O_4$ PBI [12].

To compare the LAB performance, the initial discharge capacity of LABs reported in the literature with the present work is shown in Table 3.2. The initial discharge capacity of $CoFe_2O_4$ PBI electrocatalyst on air-cathode is comparable or higher with similar electrocatalysts which are normally decorated on pristine carbon. Furthermore, the charge – discharge capacity before and after 200 charge-discharge cycles at 400 mAg^{-1} were tested as depicted in Figure 3.4b and Figure 3.4c. The charging voltage has been reduced while the discharge voltage was increased. Both charge and discharge show sign of further stability. To

obtain further charge – discharge data, the results of 200 cycle-life data are depicted in Figure 3.5. In every sample, the 1st cycle depicted high overpotential which might cause by the impurity on the cathode surface. This revealed that the battery maintains a discharge capacity as high as 100% even after the 200th cycle, demonstrating exceptional stability. The overpotential and energy efficiency for each sample are illustrated in Figure 3.6. In the case of LAB with 20%$CoFe_2O_4$ PBI cathode, overpotential remains consistently low at 140 mV throughout the examined cycle range. Besides, Fe PBI possess similar overpotential with slightly higher energy efficiency, however the overpotential start to increase after 50 cycles.

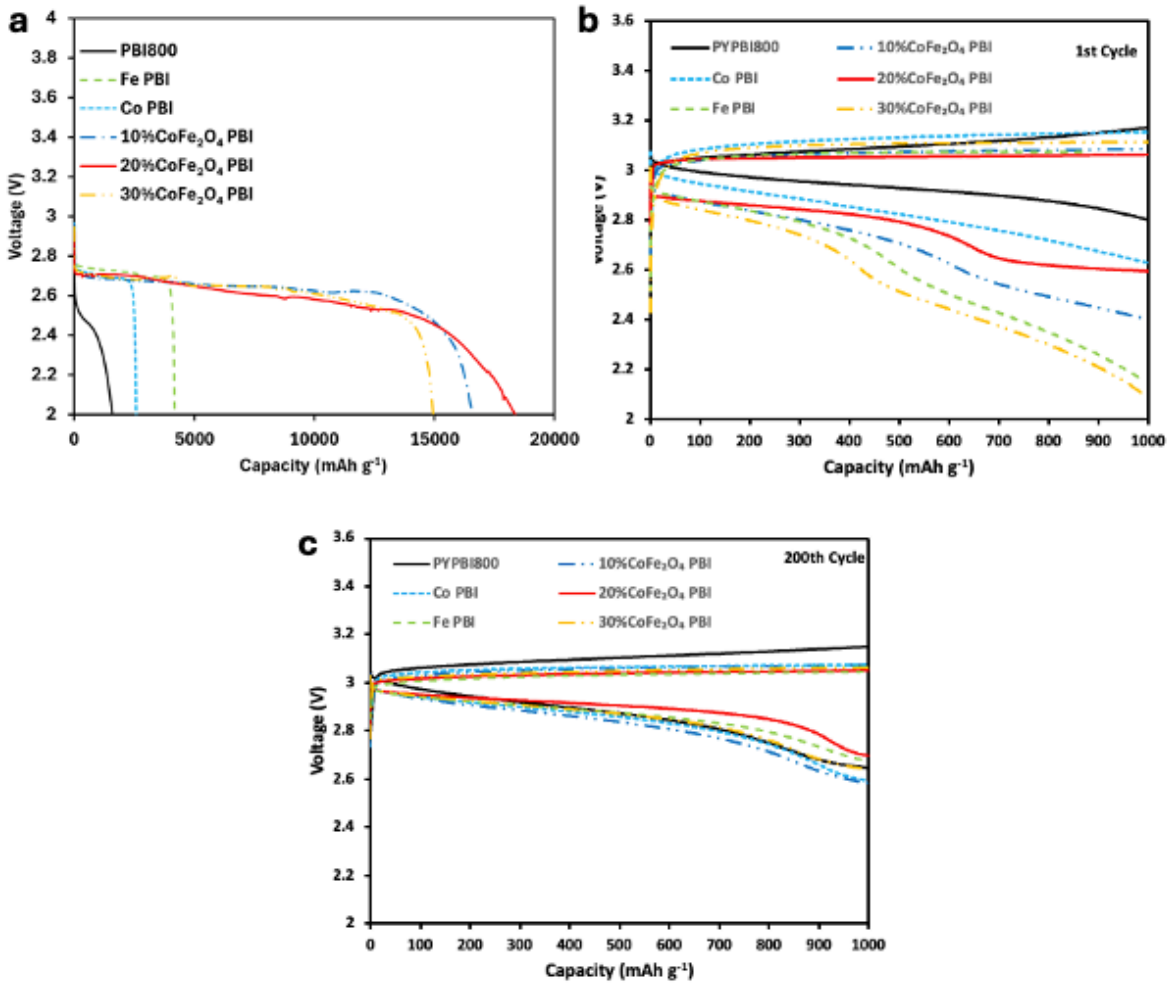

Figure 3.4 a) Initial discharge of LABs at the discharge current density of 200 mA g^{-1}, cyclic stability of LABs at current density of 400 mA g^{-1} for b) 1st cycle, and c) 200th cycle.

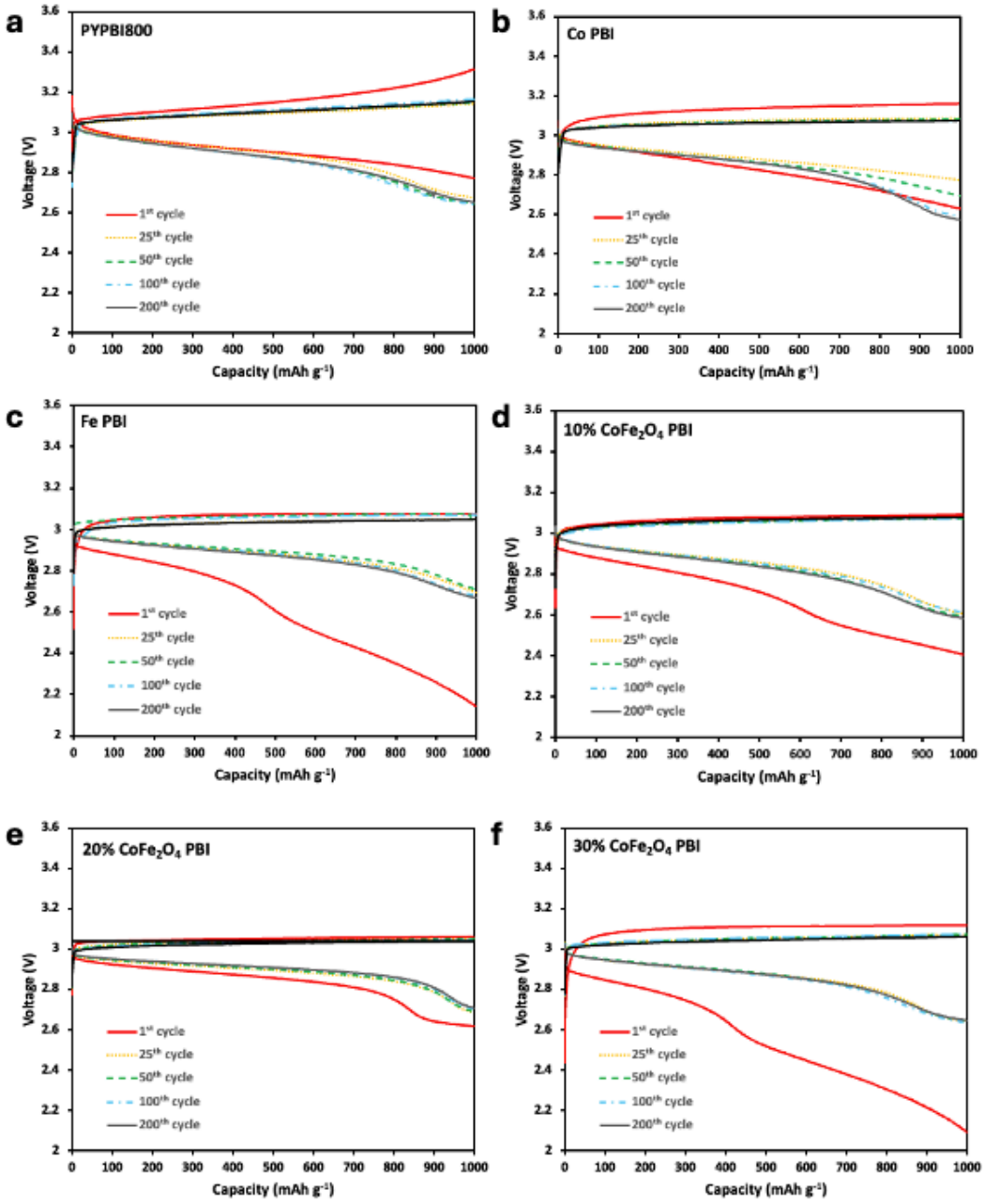

Figure 3.5 Cyclic stability of LABs at current density of 400 mA g^{-1} from 1st cycle to 200th cycle employing a) PYPBI800, b) Co PBI, c) Fe PBI, d) 10%$CoFe_2O_4$ PBI, e) 20%$CoFe_2O_4$ PBI, and f) 30%$CoFe_2O_4$ PBI as cathodes.

Table 3.2 Comparison of discharge capacity of the LAB reported in literatures.

Electrocatalyst	Discharge Capacity ($mAhg^{-1}$)	Reference
MnO_2/Carbon submicron tube	4675	[13]
MnO_2/Co_3O_4	5738	[14]
MnO_2/C	4150	[15]
Ni/$NiFe_2O_4$@C	3820	[16]
r-Co_3O_4@Ni	4448	[17]
Co/$CoFe_2O_4$/Carbon	4320	[18]
$CoFe_2O_4$/Vulcan XC-72	7510	[6]
$CoFe_2O_4$/PBI (N-doped Carbon)	18356	This work

This exceptional performance of 20% $CoFe_2O_4$ PBI are from the Fe^{3+} sites that act as the reaction sites for OER, while the Co^{2+} sites contribute to conductivity and create beneficial synergistic effects for the Fe^{3+} sites [19,20]. Additionally, the PBI's large surface area, which is marked by N heteroatom defects, offers a multitude of nucleation sites for $CoFe_2O_4$ nanoparticles. These nanoparticles serve as active sites for both ORR and OER. The $CoFe_2O_4$ nanoparticles that form on the support display a strong metal-substrate interaction (SMSI), which results in high electrocatalytic activity and stability[21]. Besides, Athika et al. have developed LAB applying $CoFe_2O_4$ on carbon black support as the air-breathing cathode. With the lack of nitrogen defects, the metal-substrate interaction was weaker[22–24] and led to lower electrocatalytic activity and stability as the capacity slightly dropped by 37% after 100 cycles of charge and discharge [18]. In our case, the porous nature of the carbon support accommodates the solid discharge product [2,25,26], ensuring oxygen diffusion and electrolyte penetration during battery cycling. Furthermore, the bifunctional electrocatalyst effectively promotes the decomposition of discharge product Li_2O_2 at a lower overpotential, contributing to the battery's high capacity. Moreover, as the charge potential was not over 3.5 V, the byproducts were not formed during this process [2]. Hence, the low overpotential with high stability originated from the SMSI between the $CoFe_2O_4$ nanoparticles and nitrogen-doped carbon support. In summary, the synthesized 10%$CoFe_2O_4$ PBI electrocatalyst holds promise as a practical air-breathing electrode for high-capacity rechargeable LAB.

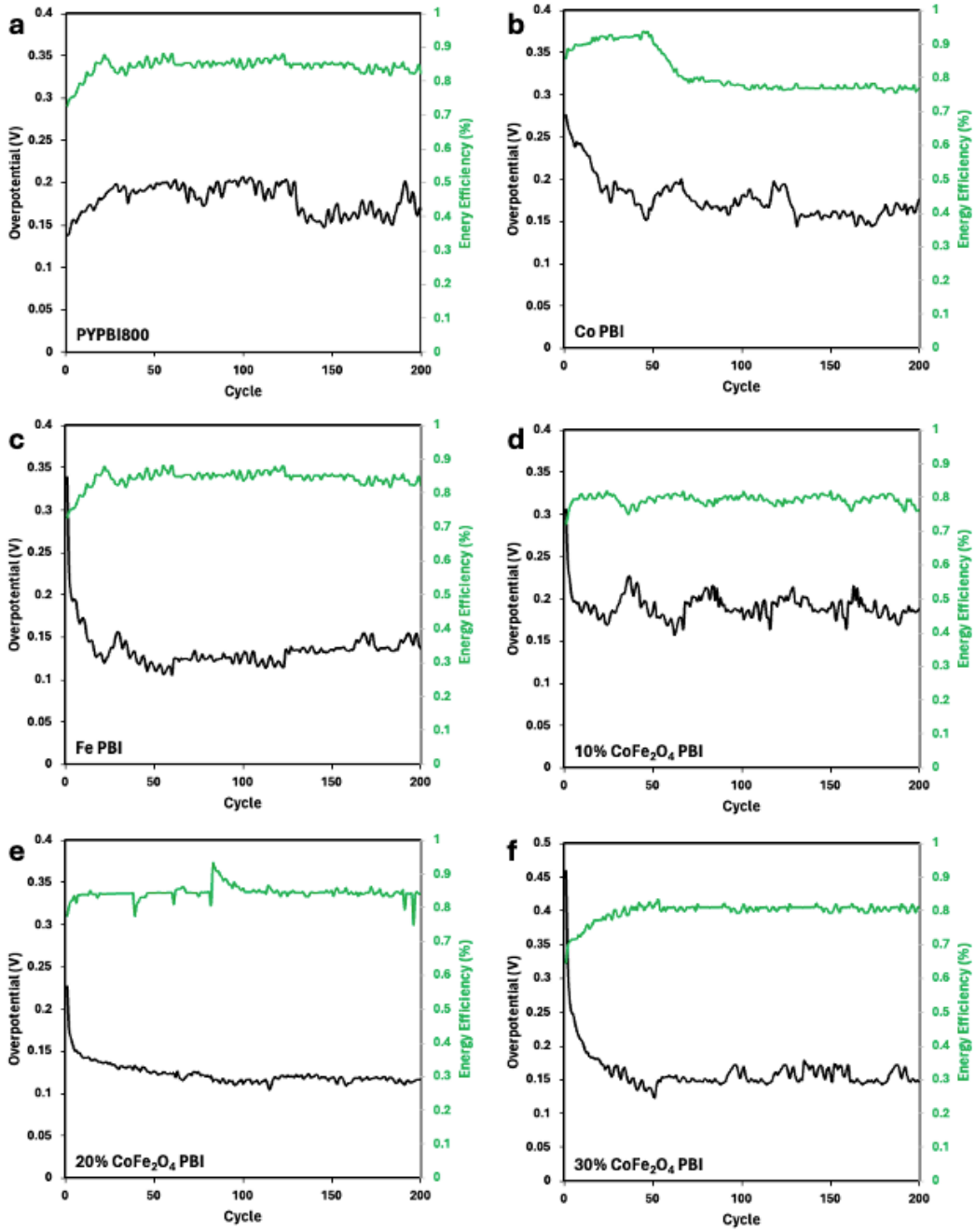

Figure 3.6 Overpotential and energy efficiency of LABs at current density of 400 mA g^{-1} from 1st cycle to 200th cycle employing a) PYPBI800, b) Co PBI, c) Fe PBI, d) 10%$CoFe_2O_4$ PBI, e) 20%$CoFe_2O_4$ PBI, and f) 30%$CoFe_2O_4$ PBI as cathodes.

3.4 Post-mortem Analysis

According to the Coulombic efficiencies results in the previous chapter, the lost efficiency might be due to the parasitic reaction during the discharge. Also, the electrode – electrolyte interface (EEI) passivation layer might be formed on the cathode [27,28]. In order to confirm the formation of EEI layer, XPS was used to identify the products from these parasitic reactions. The cathode was removed from the coin cell and washed with diethyl

carbonate (DEC). The electrode was dried under vacuum overnight, before characterized with XPS. The pristine electrode was also characterized as a control.

From the XPS results of pristine electrode, C1s spectrum shows 5 peaks at 283.3, 284.7, 287.7, 289.3, and 291.2 eV corresponded to C-C, C-O, C=O, O-C=O, and CO_3, respectively. According to Figure 3.7a, C-O and CO_3 intensities had increased after 200 cycles. These indicate that the parasitic reaction as shown in equation (3-1) and (3-2) has occurred forming $LiCO_3$. However, the intensified C-O was developed from the electrolyte which is TEGDME [29]. In O1s region, there are 2 peaks, including 531.1 and 532.2 eV corresponded to C-O and Metal-O. The higher intensity of C-O was originated from TEGDME.

The formation of EEI layer was also observed in F1s region as shown in Figure 3.7c, the peak at 684.4 eV has appeared corresponding to LiF. This suggested that the EEI layer was also formed due to the parasitic reaction between the electrolyte and binder. Hence, these observations indicated that there were parasitic reactions occurred. These reactions were led to the formation of the EEI layer which increased the cell resistance. The EEI layer formation might occurred during the first cycle according to the charge – discharge studies in which the overpotentials were significantly high in the first cycle as shown in Figure 3.5.

$$Li_2O_2 + C + \frac{1}{2}O_2 \rightarrow Li_2CO_3 \quad (3\text{-}1)$$

$$2Li_2O_2 + C \rightarrow Li_2O + Li_2CO_3 \quad (3\text{-}2)$$

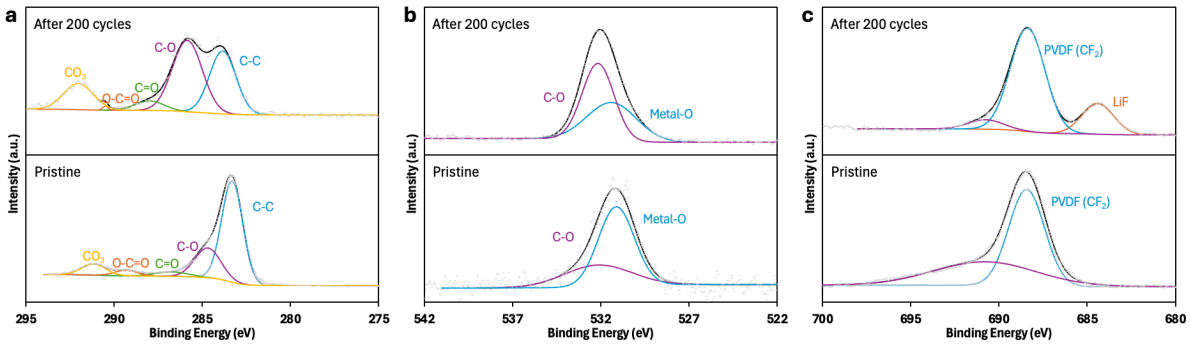

Figure 3.7 XPS results for pristine electrode and electrode after 200 charge-discharge cycles of 20%CoFe2O4 PBI at a) C1s, b) O1s, and c) F1s region

3.5 Conclusions

In this study, spinel $CoFe_2O_4$ decorated on PYPBI800 as electrocatalyst was synthesized. Material characterization confirmed the formation of the spinel structure of $CoFe_2O_4$. More importantly, the strong metal-substrate interaction (SMSI) is confirmed by the characterizations. The bifunctional electrocatalytic activity toward ORR and OER was enhanced by the SMSI together with the bonding state of Co^{2+} and Fe^{3+} in the spinel structure as the active sites. Remarkably, the 20%$CoFe_2O_4$ PBI electrocatalysts exhibited a remarkably improved catalytic limiting current density compared to other synthesized electrocatalysts. The excellent catalytic activity of 20%$CoFe_2O_4$ PBI can be attributed to the synergistic contribution of $CoFe_2O_4$ nanoparticles, and the N-doped carbon support network. As a practical demonstration, CR-2032 coin-cells utilizing 10%$CoFe_2O_4$ PBI, 20%$CoFe_2O_4$ PBI, and 30%$CoFe_2O_4$ PBI as an air-breathing electrode were fabricated. The LAB with 20%$CoFe_2O_4$ PBI achieved a high discharge capacity of 18,356 $mAhg^{-1}$ at a current density of 200 mAg^{-1}, with a remarkable charge - discharge capacity of 1,000 $mAhg^{-1}$ even at a high current density of 400 mAg^{-1}. The fabricated LAB exhibited stable charge - discharge capacity at 1,000 $mAhg^{-1}$ even after 200 charge-discharge cycles, along with acceptable overpotential. Hence, $CoFe_2O_4$ PBI holds promise as a practical air-breathing electrode for high-capacity rechargeable LABs.

References

1. N. Imanishi, O. Yamamoto, *Mater Today Adv*, 4 (2019).
2. T. Liu, J.P. Vivek, E.W. Zhao, J. Lei, N. Garcia-Araez, C.P. Grey, *Chem Rev*, 120 (2020).
3. K.N. Jung, J. Kim, Y. Yamauchi, M.S. Park, J.W. Lee, J.H. Kim, *J Mater Chem A Mater*, 4 (2016) 14050–14068.
4. W. Li, C. Han, K. Zhang, S. Chou, S. Dou, *J Mater Chem A Mater*, 9 (2021) 6671–6693.
5. Y. Cao, S.R. Cai, S.C. Fan, W.Q. Hu, M. Sen Zheng, Q.F. Dong, *Faraday Discuss*, 172 (2014) 215–221.
6. T. Şener, E. Kayhan, M. Sevim, Ö. Metin, *J Power Sources*, 288 (2015) 36–41.
7. Y. Gong, W. Ding, Z. Li, R. Su, X. Zhang, J. Wang, J. Zhou, Z. Wang, Y. Gao, S. Li, P. Guan, Z. Wei, C. Sun, *ACS Catal*, 8 (2018) 4082–4090.
8. Z. Ma, X. Yuan, L. Li, Z.F. Ma, D.P. Wilkinson, L. Zhang, J. Zhang, *Energy Environ Sci*, 8 (2015) 2144–2198.

9. L. Zhou, K. Higashimine, R. Badam, N. Matsumi, *Mater Res Express*, 10 (2023) 125508.

10. C.O. Laoire, S. Mukerjee, K.M. Abraham, E.J. Plichta, M.A. Hendrickson, *Journal of Physical Chemistry C*, 114 (2010) 9178–9186.

11. N. Wang, J. Fu, X. Cao, L. Tang, X. Meng, Z. Han, L. Sun, S. Qi, D. Xiong, *Electrochim Acta*, 428 (2022) 140894.

12. T. Zhang, M. Yu, J. Li, Q. Li, X. Zhang, H. Sun, *J Energy Storage*, 46 (2022).

13. F. Tu, Q. Wang, J. Xie, G. Cao, S. Zhang, J. Wang, S.X. Mao, X. Zhao, H.Y. Yang, *Energy Storage Mater*, 6 (2017) 164–170.

14. Y.J. Lee, D.H. Kim, T.G. Kang, Y. Ko, K. Kang, Y.J. Lee, *Chemistry of Materials*, 29 (2017) 10542–10550.

15. H. Cheng, K. Scott, *J Power Sources*, 195 (2010) 1370–1374.

16. M. Athika, V.S. Devi, P. Elumalai, *ChemistrySelect*, 5 (2020) 3529–3538.

17. L. Liu, H. Guo, Y. Hou, J. Wang, L. Fu, J. Chen, H. Liu, J. Wang, Y. Wu, *J Mater Chem A Mater*, 5 (2017) 14673–14681.

18. M. Athika, P. Elumalai, *ChemElectroChem*, 7 (2020) 4188–4200.

19. Ö.N. Avcl, L. Sementa, A. Fortunelli, *ACS Catal*, 12 (2022) 9058–9073.

20. G.A. Gebreslase, M.V. Martínez-Huerta, D. Sebastián, M.J. Lázaro, *J Colloid Interface Sci*, 625 (2022) 70–82.

21. Z. Shi, W. Yang, Y. Gu, T. Liao, Z. Sun, Z. Shi, W. Yang, Y. Gu, T. Liao, Z. Sun, *Advanced Science*, 7 (2020) 2001069.

22. Y. Lou, J. Xu, Y. Zhang, C. Pan, Y. Dong, Y. Zhu, *Mater Today Nano*, 12 (2020) 100093.

23. J.M. Coronado, Y. Yang, X. Zhang, Y. Liu, X. Ma, X. Liu, R. Zhang, Y. Wang, *Nanoenergy Advances 2023, Vol. 3, Pages 48-72*, 3 (2023) 48–72.

24. Y. Li, Y. Zhang, K. Qian, W. Huang, *ACS Catal*, 12 (2022) 1268–1287.

25. Z. Peng, S.A. Freunberger, L.J. Hardwick, Y. Chen, V. Giordani, F. Bardé, P. Novák, D. Graham, J.M. Tarascon, P.G. Bruce, *Angewandte Chemie - International Edition*, 50 (2011) 6351–6355.

26. J.W. Jung, S.H. Cho, J.S. Nam, I.D. Kim, *Energy Storage Mater*, 24 (2020) 512–528.

27. R.A. Quinlan, Y.-C. Lu, D. Kwabi, Y. Shao-Horn, A.N. Mansour, *J Electrochem Soc*, 163 (2016) A300–A308.

28. R. Tatara, P. Karayaylali, Y. Yu, Y. Zhang, L. Giordano, F. Maglia, R. Jung, J.P. Schmidt, I. Lund, Y. Shao-Horn, *J Electrochem Soc*, 166 (2019) A5090–A5098.

29. M. Carboni, A.G. Marrani, R. Spezia, S. Brutti, *J Electrochem Soc*, 165 (2018) A118–A125.

Chapter 4 Conclusion

4.1 General Conclusion

In an increasingly electrified world, energy storage technologies have become pivotal for ensuring the reliability and efficiency of various applications, ranging from portable electronic devices to electric vehicles and renewable energy systems.

Energy storage is crucial for bridging the gap between energy production and consumption, enabling the effective utilization of intermittent renewable resources, and maintaining a stable power supply during peak demand periods. Particularly batteries, have gained widespread prominence due to their high energy density, rapid response times, and versatility for diverse applications. Different types of batteries cater to specific needs, each with their unique chemistry, advantages, and limitations. Lithium-ion batteries, for instance, are renowned for their reliability and high energy density but face challenges concerning limited capacity and eventual degradation. Innovations such as lithium-sulfur and solid-state batteries have sought to address these issues, but none hold as much transformative potential as lithium-air batteries.

Energy storage is essential for balancing energy production and consumption, optimizing the utilization of intermittent renewable sources, and maintaining a steady power supply during peak demand. Among storage technologies, batteries have garnered significant interest due to their efficiency, rapid response capabilities, and versatility across different uses. Various types of batteries cater to specific requirements, each distinguished by its chemistry, benefits, and drawbacks. While lithium-ion batteries are known for their reliability and high energy density, they encounter challenges such as limited capacity and gradual deterioration over time. Innovations like lithium-sulfur and solid-state batteries are being developed to tackle these issues, yet lithium-air batteries are seen as particularly promising for their potential to bring about transformative changes.

Lithium-air batteries (LABs), also known as lithium-oxygen batteries, represent an innovative frontier in energy storage due to their unmatched potential for high energy density. The fundamental concept of a Li-air battery involves the reaction between lithium and oxygen from the air to generate electrical energy, facilitated by a porous cathode and a solid electrolyte separator. The pursuit of more effective energy storage solutions has spurred the development of lithium-air batteries, poised to transform the energy storage landscape. With their exceptional energy density potential, utilization of abundant and non-toxic oxygen sources, and

capacity to reshape various sectors, lithium-air batteries offer promise in addressing many of the challenges associated with current battery technologies. Nonetheless, it is important to acknowledge that while lithium-air batteries show great potential, there remain obstacles to overcome, including concerns regarding efficiency, longevity, and safety.

For LABs to be widely adopted, several significant challenges must be addressed. One of these is the need for an electrocatalyst to facilitate key reactions on the cathode side. Oxygen reduction reaction and Oxygen evolution reaction takes place during discharge and charge, respectively. These reactions are notably slow and have sluggish kinetics. The most used electrocatalyst for this reaction is Pt/C and RuO_2/C, but it has its drawbacks, including cost, corrosion, and durability issues. The focus of this thesis is to develop an alternative electrocatalyst using innovative methods.

Chapter 1 provides a comprehensive introduction to the principles of Lithium-air batteries. It discusses the overview of the oxygen Reduction Reaction (ORR) and oxygen evolution reaction (OER) together with their mechanism in different mediums. The chapter includes brief discussions about the reaction mechanism and the constraints of this reaction. It places special emphasis on LABs' cathode with various electrocatalysts and discusses the enhancement in ORR/OER activity by modifying with different strategies. Among the various electrocatalysts, metal nanoparticles on carbon support are widely used. This type of electrocatalysts give plenty of room for improvement including metal nanoparticles and carbon supports.

Chapter 2 delves into the significance of the synthesized and characterization of the $CoFe_2O_4$ nanoparticles on bio-based polymer derived nitrogen doped carbon. The bio-derived single precursor for both carbon and nitrogen, poly(2,5-benzimidazole) (ABPBI) has been employed as the support for spinel $CoFe_2O_4$ nanoparticles. After the pyrolysis of ABPBI, the $CoFe_2O_4$ nanoparticles are introduced via co-incipient wetness impregnation method. The characterization of the electrocatalysts has confirmed the spinel type structure of $CoFe_2O_4$ nanoparticles on pyrolyzed ABPBI (PYPBI800). Moreover, in X-ray photoelectron spectroscopy, the strong metal – substrates interaction (SMSI) is observed. This SMSI enhances the durability of the electrocatalysts. Furthermore, SMSI also plays an important role in ORR and OER in non-aqueous electrolyte. ORR and OER activity are pre-determined via rotating disk electrode with three electrodes configuration. The results indicated that at 20% $CoFe_2O_4$ nanoparticles on PYPBI800 possess the best current density and onset potential among all samples.

Chapter 3 detailed the lithium air batteries evaluation employing different electrocatalysts as the cathode. The electrocatalytic activity for ORR and OER is amplified by the SMSI, in conjunction with the bonding state of Co^{2+} and Fe^{3+} in the spinel structure serving as the active sites. Notably, the 20%$CoFe_2O_4$ PBI electrocatalysts demonstrated a significantly enhanced catalytic limiting current density compared to other synthesized electrocatalysts. The superior catalytic activity of 20%$CoFe_2O_4$ PBI can be credited to the combined effect of $CoFe_2O_4$ nanoparticles and the N-doped carbon support network. As a practical application, a CR-2032 coin-cell using synthesized electrocatalysts as an air-breathing electrode was constructed. The LAB with 20%$CoFe_2O_4$ PBI achieved an impressive discharge capacity of 18,356 $mAhg^{-1}$ at a current density of 200 mAg^{-1}, maintaining a notable charge-discharge capacity of 1,000 $mAhg^{-1}$ even at a high current density of 400 mAg^{-1}. The constructed LAB maintained a stable charge-discharge capacity at 1,000 $mAhg^{-1}$ even after 200 charge-discharge cycles, with an acceptable overpotential and energy efficiency. Therefore, this chapter shows potential of 20%$CoFe_2O_4$ PBI as a practical air-breathing electrode for high-capacity rechargeable LABs.

4.2 Future Prospects

In this doctoral research, the author has investigated the use of bio-based polymer derived N-doped carbon (poly(2,5-benzimidazole)) as the support for spinel $CoFe_2O_4$ nanoparticles. This exploration is based on their abundant redox chemistry, electrochemical importance, and the relationship between structure and property to catalyzed ORR and OER at LAB cathodes. According to the present work the possible outgrowths of this work can be as follows:

1. Employing electrocatalysts in aqueous electrolytes. This will provide a pathway to fuel cell application which is another promising energy storage.
2. Decorate noble metal nanoparticles instead of metal oxides on pyrolyzed poly(2,5-benzimidazole). From the present work, spinel $CoFe_2O_4$ nanoparticles on PYPBI800 greatly promote the LAB performance. Replace metal oxide with noble metal would eventually further enhance the LAB performance.
3. As the carbon support has the variety of tuning. It is possible to modify the PYPBI800 both physically and chemically. With this modification, the electrocatalyst might not need to be decorated with metal and work as the metal free bifunctional electrocatalyst.